博 士 論 文

Study on electric-field control of magnetism in transition metal/oxide stacked structures

(遷移金属/酸化物積層構造における
磁性の電界制御に関する研究)

平 井 孝 昌

Contents

Chapter 1

Introduction

Our present advanced civilization is supported by the development of electronics. Conventional semiconductor electronics are based on the charge property of electrons only. In contrast, electrons have another fundamental property, called "spin" degree of freedom. Spintronics is a study about the intrinsic spin together with the electronic charge degree of freedom. In the magnetic materials, an imbalance between up-spin and down-spin electrons generates the spontaneous magnetization. In addition, it bestows significant benefits onto spin-dependent electron transport phenomena. The development of the spintronics research started from the discovery of the giant magneto resistance (GMR) effect in the magnetic multilayers [1, 2]. The use of the GMR effect and the tunneling magneto resistance (TMR) effect helps us to store information in the nano-sized magnetic memory devices with a zero stand-by power. In general, the magnetization direction in the spintronic devices has been manipulated by applying the external magnetic field or injecting the spin-polarized electrical current into the device, which involve the Joule heating loss. In recent, there are some attempts to control the magnetization by using the electric-field effect [3–6]. The application of the electric-field realize more efficient magnetization manipulation because it only requires a charge accumulation/depletion energy consumption.

This thesis presents an experimental study on the electric-field control of magnetism in the layered structure composed of transition metals ($3d$, $4d$, and $5d$) and oxide dielectric insulators. Our findings not only deepen understanding of the physics underlying the EF modulation of magnetism but also in the field-effect spintronic devices. In this chapter,

we review the basic background of the EF control of the magnetization and other magnetic properties associated with the spin-orbit coupling in various ferromagnetic materials.

1.1 Idea of electric-field effect

The first idea of a field-effect transistor (FET) was proposed in 1925 and credited as a patent by J. Lilienfeld [7]. As shown in Fig. 1.1(a), in the Al-based Al_2O_3/Cu_2S metal-insulator-semiconductor FET (MIS-FET) structure, by applying a voltage between Al and Cu_2S, an transverse electric field through an insulating layer only caused the longitudinal conductance change of Cu_2S channel without the carrier flowing from Al into a semiconductor. This concept is called "electric-field (EF) effect". At that time, however, this proposal was not achieved as a practical device due to underdeveloped semiconductor manufacturing and little apparent understanding of underlying physics. In early-1960, M. Atalla and D. Kahng at Bell Telephone Laboratories invented the modern metal-oxide-semiconductor FET (MOS-FET) on the crystalline Si with stable thermally grown SiO_2 insulator [8]. Fig. 1.1(b) shows a typical *n*-channel-type MOS-FET. The application of the transverse gate EF induces the modulation of the negative carrier density in a Si channel, resulting in the electron conductance change between source-drain electrodes. Si-FET technologies have developed our industry and life in the past five decades. In addition, recently, the EF effect has been known as a tool to modify some charge-density-related phenomena, such as metal-insulator transition [9] and superconducting phase transition [10, 11].

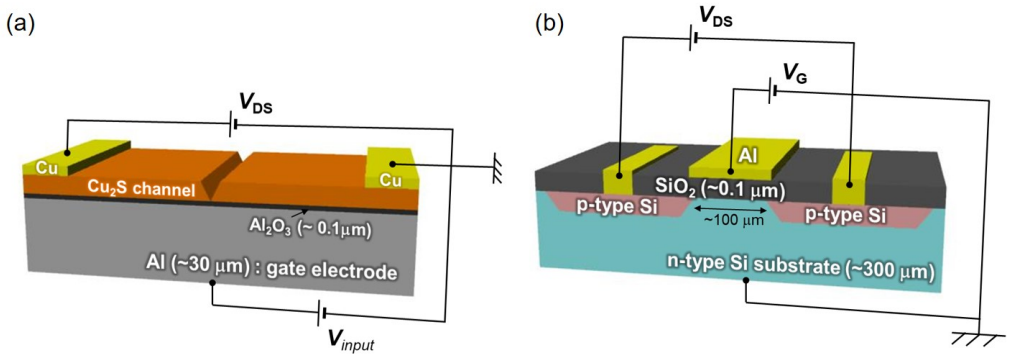

Figure 1.1: Schematics of (a) MIS-FET adopted by J. Lilienfeld and (b) MOS-FET.

1.2 Electric-field effect on magnetism in semiconductors

Controlling magnetism by the application of gate bias, the EF effect on magnetism was first demonstrated in a Mn-doped InAs: (In,Mn)As in 2000 [3]. (In,Mn)As, which is a *p*-type diluted magnetic semiconductor, was synthesized by molecular beam epitaxy [12]. Fig. 1.2 shows the result of the anomalous Hall measurement for each gate voltage. The EF was applied into 5-nm-thick (In,Mn)As through a polyimide layer in this study. A negative bias, which results in hole doping into (In,Mn)As, induced a square hysteresis curve while a paramagnetic-like response was observed for a positive gate voltage application. The ferromagnetism of (In,Mn)As and (Ga,Mn)As is often explained from the *p*-*d* exchange interaction between the local magnetic moment and the holes through Mn-doping [13,14]. Thus, magnetic properties of these materials strongly depend on the number of hole carriers. Therefore, the mechanism of EF effect on ferromagnetic phase transition (= Curie temperature of (In,Mn)As) is due to the change in hole concentration by the EF effect. A little later, the EF contorl of magnetic coercivity in (In,Mn)As was shown using SiO_2 dielectric insulator [15]. In addition, for (Ga,Mn)As [16], the EF control of Curie temperature T_C [17] and a spontaneous magnetic moment [18] were also demonstrated. Further, the EF manipulation of magnetization vector was achieved [19]. This report indicated that the magnetic anisotropy (MA) which determines the magnetic easy axis could be modified by EF. The present T_C of (In,Mn)As and (Ga,Mn)As is still ~200 K [20], but recently room temperature (RT)-EF control of magnetism in the semiconductor was demonstrated in Co-doped TiO_2: $(Ti,Co)O_2$ [21].

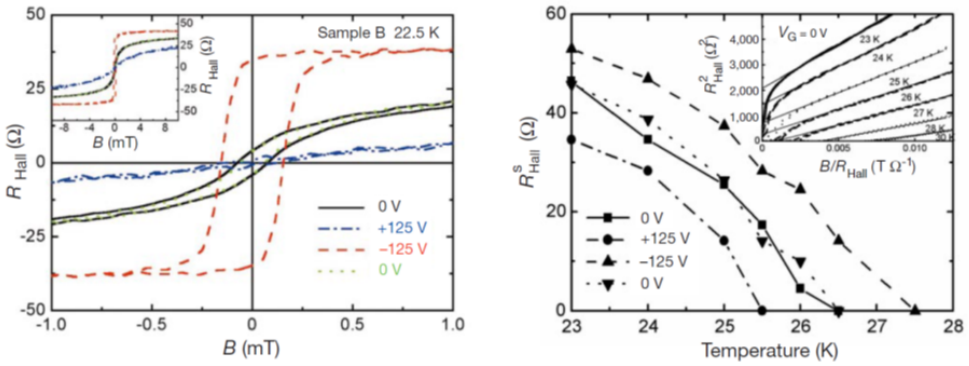

Figure 1.2: The first observation of EF control of the magnetic phase transition in (In,Mn)As at 22.5 K [3].

1.3 Electric-field effect on magnetism in ferromagnetic metals

Following the study in ferromagnetic semiconductors, the EF control of magnetism in ferromagnetic metals started to be examined. However, it was considered to be difficult to observe clear EF effect on magnetism in metals due to the associated short electrostatic screening length (< 1 nm). In 2007, the first demonstration of the EF effect on magnetism was reported for FePd and FePt films of 2 nm using an electric double layer (EDL) [22]. EDL gating allows us to apply a large EF of over 10 MV/cm at solid/liquid interfaces. The magnetization curves of FePt/EDL under each gate voltage V_G were measured by magneto-optical Kerr effect (MOKE) (Fig. 1.3(a)). The clear increase in coercivity is observed increasing the amplitude of negative V_G, where electrons are depleted at the FePt surface. In 2009, the EF effect on the MA at the Fe/MgO interface was observed in a solid-state capacitor consisting of the 0.48-nm-thick ultrathin Fe electrode and the MgO dielectric layer [23]. Fig. 1.3(b) shows the magnetization curves of the Fe/MgO/polyimide system for $V_G = \pm 200$ V, where the gate electric field E_G in the MgO dielectric is $\sim \pm 0.45$ MV/cm, measured by MOKE. The out-of-plane magnetic saturation field under positive V_G application is larger than that under negative V_G application, indicating that perpendicular MA (PMA) energy decreases (increases) by the positive (negative) V_G application. The PMA energy is defined as the difference between the spin-orbit interaction energy along out-of-plane and in-plane magnetization. The EF effect on the MA has been intensively studied in many ferromagnetic metal and alloy films.

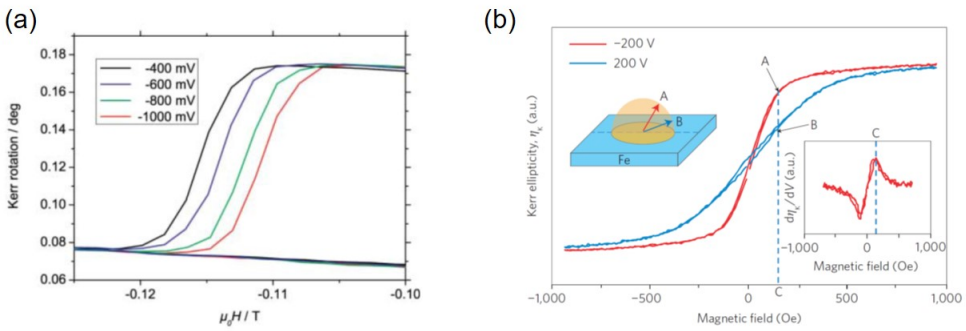

Figure 1.3: The first observation of the EF effect on magnetism of ferromagnetic metals (a) in an EDL capacitor [22] and (b) in a solid-state capacitor [23].

In 2011, as demonstrated for semiconductors, the EF control of the ferromagnetic phase transition has been observed in 0.4-nm-thick Co at around RT [24]. Fig. 1.4(a) shows anomalous Hall resistance curves of a Pt/Co/MgO stack measured by sweeping out-of-plane magnetic field H for $V_G = \pm 10$ V. Clear transition from the square hysteresis under $V_G = +10$ V into the paramagnetic-like response under $V_G = -10$ V is observed. Not only the field dependence of R_{Hall} but also temperature dependence of the spontaneous R_{Hall}, which is proportional to the spontaneous magnetization, was investigated (Fig. 1.4(b)). The change in the falls of the spontaneous R_{Hall} indicates EF-change in T_C. The T_C modulation determined by Arrott plot: R_{Hall}^2 versus R_{Hall}/H plot, is about 10 K for $V_G = \pm 10$ V applications. Assuming that the Co layer sputtered on the fcc(111)-oriented Pt layer has fcc(111) texture [25–27], the change in the electrons numbers in the Co surface Δn_e is estimated ± 0.012 electrons per Co atom by $V_G = \pm 10$ V applications. Subsequently, a giant modulation of T_C of $\sim$100 K across RT was achieved with this structure by using EDL gating [28]. The EDL is formed by using a polymer film containing an ionic liquid: EMI^+–$TFSI^-$ (an ionic liquid film). Temperature dependence of the spontaneous areal magnetic moment for $V_G = 0$ V and $V_G = \pm 2$ V ($E_G \sim \pm 2.5$ MV/cm) was directly measured by a superconducting quantum interference device (SQUID) magnetometer (Fig. 1.4(c)). Δn_e in this system calculated from the capacitance of EDL was ± 0.042 electrons per Co atom by applying $V_G = \pm 2$ V, indicating that this larger change in T_C than that in solid-state capacitor is attributable to the large change in the number of electrons even though the magnitude of applied EF into the Co surface was almost the same order. However, this result is disagreement with the prediction from the Slater-Pauling curve, which is the relationship between the number of electrons and the magnetic moment per atom (and T_C) for $3d$ transition alloys [29]. We will mention about this later. In Fig. 1.4(c), it has been found that the magnetic moment is also modified by the EF application. Indeed, EF-change in a saturation magnetic moment in the Pt/Fe/MgO/EDL [30] system (Fig. 1.4(d)) and a spontaneous magnetic moment in the Pt/Co/Pd/MgO/EDL system [31] and the HfO_2/MgO/Pd/Co [32] system were proved by the direct magnetization measurements.

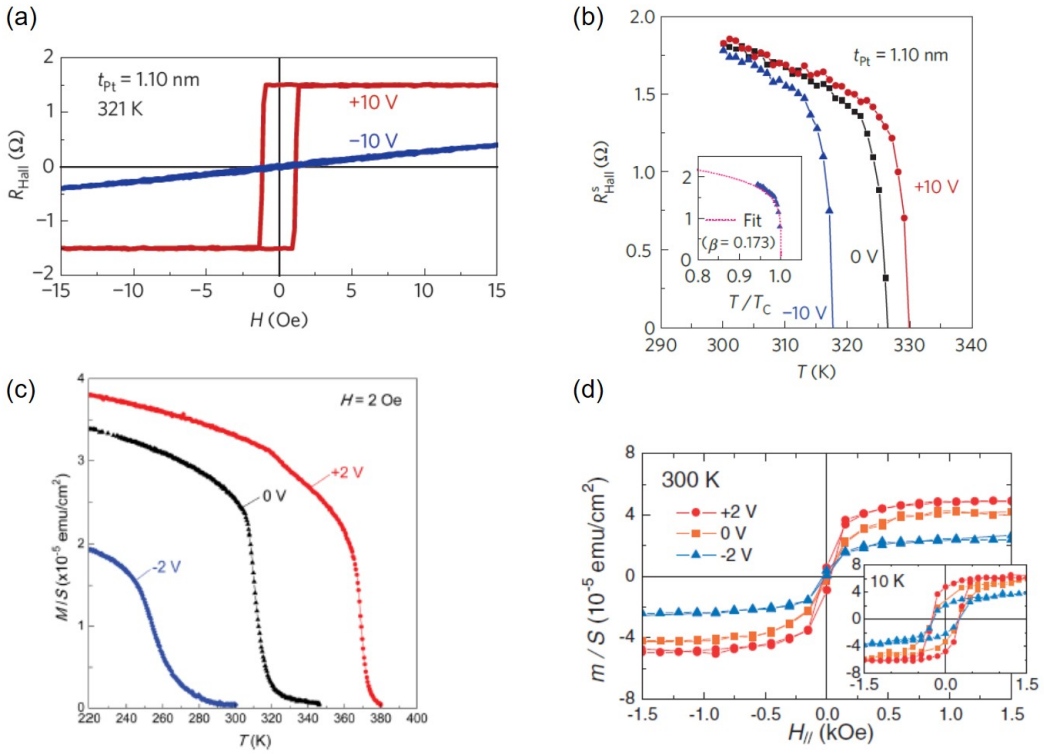

Figure 1.4: (a),(b) The demonstration of the RT-EF control of ferromagnetic phase transition in the Pt/Co/MgO structure using solid-state HfO_2 gating [24]. (a) shows anomalous Hall resistance curves measured by sweeping out-of-plane magnetic field for $V_G = \pm 10$ V ($E_G \sim \pm 2$ MV/cm). (b) The temperature dependence of the spontaneous R_{Hall}. (c) The temperature dependence of the areal magnetic moment in Pt/Co/MgO/EMI$^+$−TFSI$^-$ [28]. (d) Magnetization hysteresis loops at 300 K and 10 K for Pt/0.4-nm-thick-Fe/MgO/ionic-liquid film [30].

Furthermore, the EF applications influence the exchange interaction between ferromagnetic spins. The exchange interaction between two spins, $\boldsymbol{S}_i$ and $\boldsymbol{S}_j$, is written as

$$\mathscr{H}_{Ex} = -J\boldsymbol{S}_i \cdot \boldsymbol{S}_j, \tag{1.1}$$

where J is an exchange coupling constant. Fig. 1.5(a) shows the MOKE images of magnetic domains in the Pt/Co/MgO structure [33]. Clear modification of the magnetic domain width is observed by applying $V_G = \pm 10$ V through 50-nm-thick HfO_2 dielectric layer ($E_G \sim \pm 3.7$ MV/cm). The domain width is described as [34]

$$w_d = 2\sqrt{\frac{A}{K_u}} \exp\left(\frac{4\pi\sqrt{AK_u}}{\mu_0 M_s^2 t}\right), \tag{1.2}$$

where A, K_u, M_s, t, and μ_0 are the exchange stiffness constant, the PMA energy per unit volume, the saturation magnetization, the ferromagnetic thickness, and the vacuum permeability, respectively. In this report, it is shown that the EF modification of $A \propto J$ dominantly caused the change in w_d. In addition, the measurement of the reduction in the magnetization with temperature scales with Bloch's law for the thermal spin wave excitation [35] confirms the EF change in the exchange coupling constant J (Figs. 1.5(b) and (c)) [36]. The EF modulation of J has been also reported in the Ta/CoFeB/MgO/Al_2O_3 by using the MOKE measurement [37] and by the CoFeB/MgO/CoFeB magnetic tunnel junction (MTJ) by using the ferromagnetic resonance (FMR) measurement [38, 39].

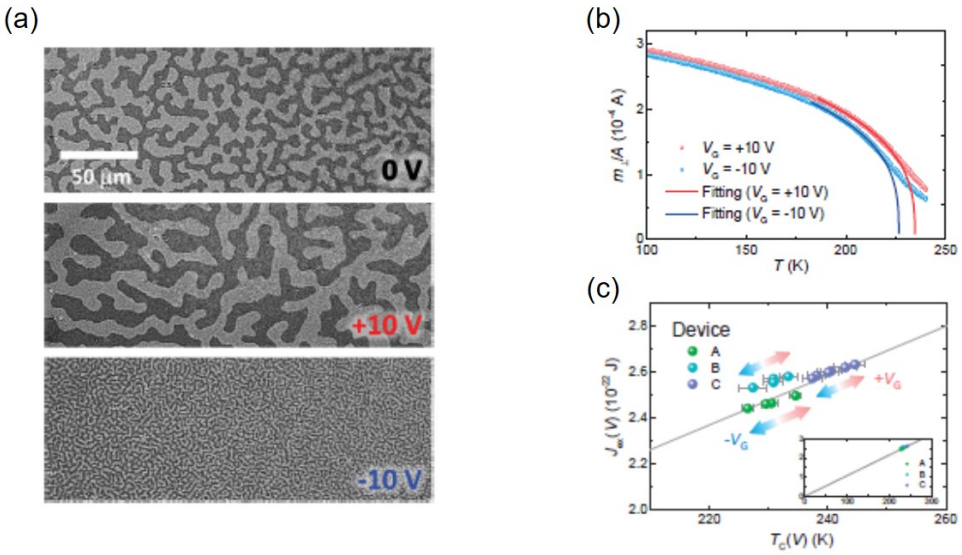

Figure 1.5: (a) The domain structure taken using a MOKE microscope at 320 K for V_G = 0, +10, and −10 V application [33]. (b) The temperature dependence of perpendicular component of the areal magnetic moment with a 200 Oe magnetic field under V_G = ±10 V [36]. (c) V_G dependence of exchange coupling for three Pt/Co/MgO/HfO_2 samples [36].

In addition to the exchange interaction, the EF control of interfacial Dzyaloshinskii-Moriya interaction (iDMI) has been reported [40–44]. Dzyaloshinskii-Moriya interaction (DMI) is an antisymmetric exchange interaction between two spins originated from the spin-orbit interaction [45–47] and described as

$$\mathscr{H}_{DM} = -\boldsymbol{D} \cdot (\boldsymbol{S}_i \times \boldsymbol{S}_j), \tag{1.3}$$

where $\boldsymbol{D}$ is the DMI vector. While DMI was first discussed in bulk materials with a spacial inversion symmetry [48], it has been pointed out that DMI also emerges in the hetero-interface of thin films [49, 50]. The EF effect on iDMI was first demonstrated in the asymmetric Au/Fe/MgO/SiO_2 system by the spin wave propagation method [40]. iDMI gives rise to asymmetric spin-wave dispersion depending on the sign of the wave vector k, which causes a shift of the asymmetric resonant frequency [51]. The top panels of Figs. 1.6 (a) and (b) show the spin wave propagation signals under the in-plane magnetic field of 40 mT and $V_G = 0$ V for the 20-nm-thick Fe film. S_{21} and S_{12} corresponds to the propagation directions of $+k$ and $-k$, respectively. The bottom panels of Figs. 1.6 (a) and (b) show the subtracted signals of S_{21} and S_{12} between $V_G = 0$ V and $V_G = 4$ V. The subtracted signal shifted to lower frequency side, and moreover, the linear increase (decrease) in the subtraction is obtained, which are attributed to the occurrence of the EF change in iDMI. The EF change in the areal iDMI energy is evaluated to be 40 $\mathrm{nJ/m^2}$ at $V_G = 1$ V by the calculation of the difference between S_{21} and S_{12} signals. The spin wave spectroscopy of the EF change in iDMI was demonstrated in some in-plane magnetized films, such as V/Fe/Co/Pd/MgO [43], V/Fe/CoNi/(Pd)/MgO [44], and Pt/Co/MgO/HfO_2 structures [42],. The EF modulation of iDMI in the perpendicularly-magnetized film was investigated by measuring the domain wall (DW) velocity. Fig. 1.6 (c) shows the perpendicular magnetic field H_z dependence of the DW velocity v under $V_G = 0$, and $V_G = \pm 15$ V in the Pt/Co/Pd/MgO/HfO_2 structure. First, v linearly increased with H_z, then v got saturated above ~200 mT. The value of the saturation v (v_s) decreased (increased) by the positive (negative) V_G application. v_s is expressed as [49]

$$v_s = \frac{\pi}{2}\gamma\frac{Dt}{tM_s} = \frac{\pi}{2}\gamma\frac{D}{M_s}, \tag{1.4}$$

where γ and D are the gyromagnetic ratio and the magnitude of the areal iDMI energy. The sign of the EF change in the areal magnetic moment tM_s is consistent with the sign of the EF change in v_s [31], but the small ratio of the tM_s change ($< 1\%$) could not explain this result. Calculated Dt is shown in Fig. 1.6(d). The clear decrease (increase) in iDMI for the positive (negative) V_G application is obtained. In this study, it was discussed that the contribution of the EF change in iDMI dominantly affected the change in the DW motion than that of the EF effect on the MA (Fig. 1.6(e)). The calculated areal iDMI energy change is ~1.7 $\mu\mathrm{J/m^2}$ at

V_G = 1 V, which is much larger than that in the Au/Fe/MgO system. The enhancement of the EF-induced iDMI change by inserting the Pd layer between ferromagnet and MgO layers has been also observed in the V/Fe/CoNi/(Pd)/MgO systems [44].

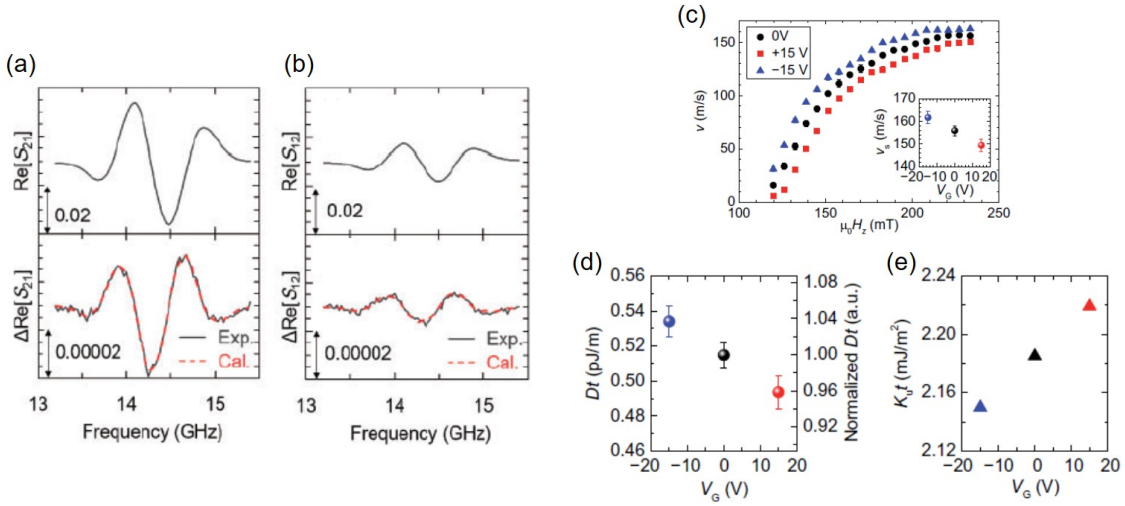

Figure 1.6: (a),(b) Spin wave propagation signals under the in-plane magnetic field of 40 mT for the Au/Fe/MgO/SiO_2 system. Bottom panels show the difference signals between V_G = 0 V and V_G = 4 V. Red dashed lines represent fitting results [40]. (c) The perpendicular magnetic field dependence of the DW velocity under V_G = 0, +15, and −15 V for the Pt/Co/Pd/MgO/HfO_2 system [41]. (d),(e) V_G dependence of the areal iDMI and PMA energy, respectively [41]

.

1.4 Mechanisms of electric-field control of magnetism in ferromagnetic metals

Several possible mechanisms of the EF effect on magnetism have been discussed. They are roughly divided into purely-electronic effects and electrochemical effects. In this section, we focus on the purely-electronic mechanisms. The electrochemical mechanisms, such as a voltage-driven redox reaction [52, 53], will be mentioned later in Chap. 4.

Around the same time as the experimental observation of the EF effect on magnetism in metals [22, 23], the comprehensive first-principles theoretical studies were attempted to understand its microscopic origin. C. Duan *et al.* stated that the change in electron density at the surface of ferromagnet, such as Fe, Ni, and Co, affects the spin-dependent screening of the EF [54]. Fig. 1.7(a) shows calculated EF-induced majority-spin and minority-spin electron charge densities along the z direction normal to the film plane for a 21 Å-thick Fe film. The Fe layer is located between about z = 5.5 and 26.5 Å in vacuum and the applied EF is 100 MV/cm. Because of the electrostatic screening effect, the surface dipoles are created at the Fe surface. Further, the EF-induced charge density is strongly spin-polarized, resulting in the change in the surface magnetization and the surface MA. Subsequently, it was reported that the external applied EF can lead not only a shift of Fermi energy E_{F} due to a change in the number of electrons but also a change in the 3d band structure [55], including the change in the occupancy of 3d orbitals [56]. Fig. 1.7(b) shows the calculated minority-spin band structure of an Fe(001) monolayer, where band 1, 3, 4, 5, and 5* are d_{z^2}, $d_{x^2-y^2}$, d_{xy}, bonding $d_{xz,yz}$, and anti-bonding $d_{xz,yz}$ states, respectively. Although the most of the band structures are similar under each EF application, significant changes in the hybridization of bands 1 and 5 near E_{F} are obtained by applying the EF of 1 eV/Å due to the EF-induced internal coupling between p orbitals and d near the E_{F} of a 3d metal layer (shown as black arrows). In addition, the recent theoretical works have presented the internal hybridization of p electrons and d electrons affects the change in EF-induced screening charge density [57, 58]. Fig. 1.7(c) shows the density of state (DOS) of a freestanding Fe monolayer with an in-plane lattice constant of MgO(001) for the spin-spiral (magnon) states in the EF of 0 (blue) and 100 MV/cm (red), where E_{F} is set to zero. It is found that the pseudogap above E_{F} is

induced by the application of the EF. As shown in Figs. 1.7(d) and (e), the EF affects the p and d electron states individually, resulting the formation of the pseudogap owing to the p-d hybridization. They predicted that the EF-induced change in the number of electron mainly influence on sp electrons because of the EF screening effects, that is, it is possible that the positive EF (for increase in the number of electrons of Co atom) induces the decrease in the number of local d electrons while the sp electrons increases. They also reported that the positive (negative) EF application increases (decreases) T_C of the Co monolayer by calculating the EF-induced magnon formation energy, which is consistent with experimental results introduced above [24, 28]. The EF application can also affect the p-d hybridization at the interface of $3d$ transition metals and oxide, such as Fe(Co)/MgO (hybridization between O-$2p$ and Fe(Co)-$3d$) [59, 60].

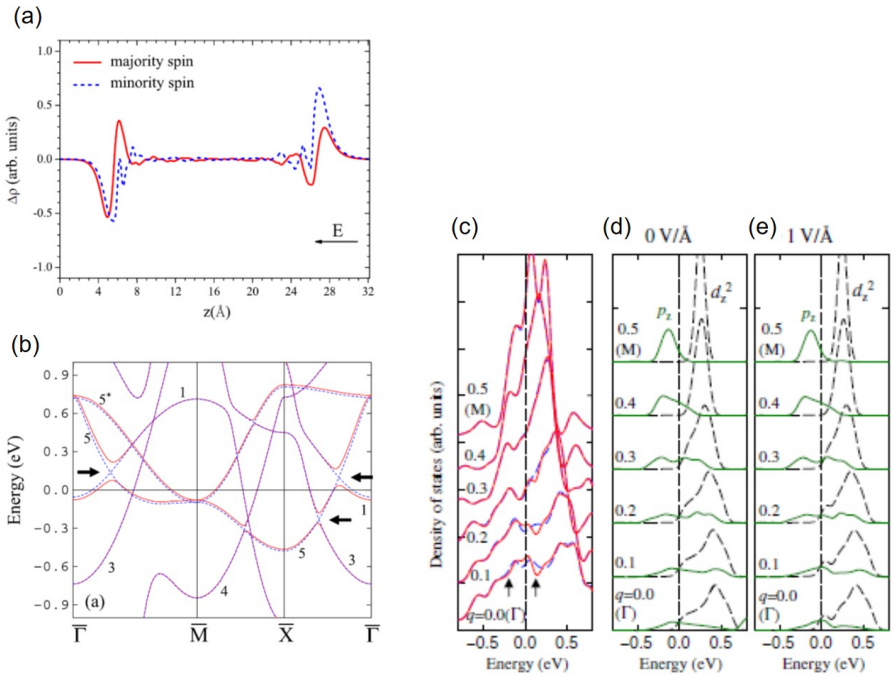

Figure 1.7: (a) EF-induced majority-spin and minority-spin electron charge densities along the z direction normal to the film plane for a 21 Å-thick Fe film [54]. (b) The minority-spin band structure for an Fe(001) monolayer in an external applied EF of 0 (dotted lines) and 1 eV/Å (solid lines) [55]. Black arrows show band gaps induced by the EF application. (c) Calculated DOS for Fe monolayer. Blue and red lines represent the DOS for 0 and 100 MV/cm of EF, respectively [57]. (d), (e) Partial DOS of the p_z and d_{z^2} orbitals for 0 and 100 MV/cm of EF, respectively. The DOS of p_z orbitals is magnified by 40 times with respect to d_{z^2} DOS [57].

Physical origin of the electric-field control of perpendicular magnetic anisotropy

From here, we focus on the origin of PMA and its EF effect. First of all, we discuss about the effect of the MA. The spontaneous magnetization in ferromagnets is derived from the isotropic exchange interaction between spins of ferromagnetic atoms. Therefore, if there is no additional interaction, the magnetization can orient any directions without changing the internal magnetic energy. However, the magnetization in actual magnetic materials prefer certain magnetizing directions. This phenomena is called MA. In general, the energy of MA has the same symmetry as the crystal structure of the ferromagnets, thus MA is also called magnetocrystalline anisotropy (MCA). The origin of MCA is suggested to be the spin-orbit interaction (SOI). The simplest expression of SOI is as follows;

$$\mathscr{H}_{\mathrm{SOI}} = \xi \boldsymbol{L} \cdot \boldsymbol{S}, \tag{1.5}$$

where ξ, $\boldsymbol{L}$, and $\boldsymbol{S}$ are the spin-orbit interaction coefficient, total orbital angular momentum vector, and total spin angular momentum vector. In addition, the shape of ferromagnets affects the determination of the magnetic easy axis. By the existence of the magnetization, the demagnetizing field is generated and gives rise to an anisotropy in a ferromagnet, which we call a shape anisotropy. For the thin-film approximation, the magnetization generally prefers to point out the in-plane direction for the demagnetizing energy of $\mu_0 M_s^2/2$, whereas the bulk MCA has little contribution in ultrathin ferromagnetic films.

The PMA observed in actual thin-layered structures is considered to be by the contribution at the surface or interface of ultrathin ferromagnets, called interfacial MA (or interfacial MCA). A strong PMA emerges for only a limited number of bilayers, such as Cu/Fe [61], Fe(Co)/MgO [62], Ni/Co [63], Pd/Co [25,64], and Pt/Co [25,65]. The microscopic origin of the interfacial PMA is proposed by an interaction with adjacent layers, a lattice mismatching [66] or a surface roughness at the interface [67]. The interfacial PMA was usually studied by x-ray circular dichroism (XMCD) spectroscopy. The XMCD study provides us with the quantitative separation and determination of the spin magnetic moment m_{S}, the orbital magnetic moment m_{L}, and the magnetic dipole moment m_{T}, and their anisotropies [68,69]. m_{S} and m_{L} are proportional to the $\boldsymbol{S}$ operator $(-2\mu_{\mathrm{B}}\langle S\rangle/\hbar)$ and the $\boldsymbol{L}$ operator $(-\mu_{\mathrm{B}}\langle L\rangle/\hbar)$,

respectively. Note that $\langle X \rangle$ denotes the expectation value of $\boldsymbol{X}$. m_{T} corresponds to the intra-atomic magnetic dipole operator $\boldsymbol{T}$ ($\mu_{\mathrm{B}}\langle T \rangle/\hbar$). Considering the higher term in the multipole expansion of the spin-density, $\boldsymbol{T}$ is given as

$$\boldsymbol{T} \quad = \quad \boldsymbol{S} - 3\boldsymbol{r}(\boldsymbol{r} \cdot \boldsymbol{S}), \tag{1.6}$$

where $\boldsymbol{r}$ represents an position unit vector [69]. In general, the α-direction component of $\boldsymbol{T}$ T_α is described as [70],

$$T_\alpha = \sum_\beta Q_{\alpha\beta} S_\beta, \tag{1.7}$$

where $Q_{\alpha\beta}$ is the matrix element of the quadrupole tensor for the charge distribution $\boldsymbol{Q}$, given as [71–73]

$$Q_{\alpha\beta} \quad = \quad \delta_{\alpha\beta} - 3r_\alpha r_\beta = \frac{2}{7\hbar^2}\left(\frac{[L_\alpha,\ L_\beta]_+}{2} - \frac{1}{3}L^2\delta_{\alpha\beta}\right). \tag{1.8}$$

Here, $\delta_{\alpha\beta}$ and $r_{\alpha(\beta)}$ are Kronecker-delta and the electron coordinate, respectively. The tensor element $Q_{\alpha\beta}$ is expressed as a linear relation of the spherical harmonics $Y_l^m(\theta,\ \varphi)$ with $l = 2$. Because the $\boldsymbol{Q}$ is connected to the quadrupole operator of the angular momentum, $Q_{\alpha\beta}$ follows the second equation of Eq. (1.8). Considering the material whose SOI is much smaller than the exchange interaction and the potential arising from the crystal field effect and $\langle S \rangle$ has the isotropic distribution against the spin orientation (such as $3d$ transition metals), $\boldsymbol{T}$ is decoupled from the $\boldsymbol{S}$ term and $\langle T \rangle$ and m_{T} reflect the quadrupole moment [74].

As discussed shortly, the PMA in the ferromagnets is generally considered to be determined by the magnitude of m_{L}. Actually, in the case of Pt/Co interface, the XMCD study confirmed that the hybridization of Co-$3d$ and Pt-$5d$ orbitals increases the perpendicular component of m_{L}, thus resulting in the enhancement of the PMA energy [65]. We note that the m_{T} term is induced by d electrons in environments with the large SOI as well as the asymmetry of the electrical charge distribution discussed above. In general m_{T} can be ignorable for the cubic $3d$ transition bulk metals. However, in the low-dimensional magnetic films and multilayers, m_{T} cannot be neglected and has an impact on the PMA energy [73, 75].

By treating the second-order perturbation of the SOI, the PMA energy is described as follows [73];

$$E_{\mathrm{PMA}} \approx -\frac{1}{4}\frac{\xi}{\hbar}\Big(\langle \Delta L_{\downarrow\downarrow}\rangle - \langle \Delta L_{\uparrow\uparrow}\rangle\Big) + \frac{7}{2}\frac{\xi}{\hbar}\Big(\langle \Delta T'_{\downarrow\uparrow}\rangle + \langle \Delta T'_{\uparrow\downarrow}\rangle\Big), \tag{1.9}$$

where $\langle \Delta L\rangle \equiv \langle L_z\rangle - \langle L_x\rangle$ and $\langle \Delta T'\rangle \equiv \langle T'_z\rangle - \langle T'_x\rangle$ are used. Here, $\langle L_z\rangle$ ($\langle T'_z\rangle$) and $\langle L_x\rangle$ ($\langle T'_x\rangle$) are evaluated for the z and x components of the spin angular momentum, respectively. $\uparrow$ and $\downarrow$ represent the contributions from majority- and minority-spin band, respectively. On the other hand, the orbital magnetic moment and the magnetic dipole term characterized by sum-rule for XMCD spectroscopy [68, 69] have the following relationships;

$$\begin{aligned} \Delta m_{\mathrm{L}} &= m_{\mathrm{L}}^{\perp} - m_{\mathrm{L}}^{\parallel}, \\ &= -\frac{\mu_{\mathrm{B}}}{\hbar}\Big(\langle \Delta L_{\downarrow\downarrow}\rangle + \langle \Delta L_{\uparrow\uparrow}\rangle\Big), \end{aligned} \tag{1.10}$$

$$\begin{aligned} -7\Delta m_{\mathrm{T}} &= -7\big(m_{\mathrm{T}}^{\perp} - m_{\mathrm{T}}^{\parallel}\big), \\ &= -\frac{\mu_{\mathrm{B}}}{\hbar}\Big(\langle \Delta L^2_{\downarrow\downarrow}\rangle - \langle \Delta L^2_{\uparrow\uparrow}\rangle\Big) - 7\frac{\mu_{\mathrm{B}}}{\hbar}\Big(\langle \Delta T_{\downarrow\uparrow}\rangle + \langle \Delta T_{\uparrow\downarrow}\rangle\Big). \end{aligned} \tag{1.11}$$

Therefore, two mechanisms have been proposed as the origin of EF effect on MA [5, 6]. The first and conventional mechanism is the change in the orbital magnetic moment induced by the interfacial charge accumulation (Fig. 1.8(a)) which corresponds to the first term in Eq. 1.9. For the materials whose majority-spin band is fully occupied (e.g. $3d$ transition metals), $\langle \Delta L_{\uparrow\uparrow}\rangle$ term can be ignored. Therefore, the PMA energy has the following relation;

$$E_{\mathrm{PMA}} \approx \frac{\xi}{4\mu_{\mathrm{B}}}\Delta m_{\mathrm{L}}. \tag{1.12}$$

This equation is well-known as the Bruno model in the past three decades [76, 77]. Each d orbitals has different vicinity near E_{F}, so that the charge accumulation/depletion effect induces the change in the orbital occupancy. The latter mechanism is electric quadrupole mechanism corresponding to the second spin-flip term in Eq. 1.9 (Fig. 1.8(b)). Because of EF screening, the external applied EF has inhomogeneous distribution along the out-of-plane direction at the metal surface. By the linkage of such EF and the electric quadrupole, a

spin distribution change is appeared, resulting in an additional uniaxial MA energy through spin-flip excitation processes in the system [78]. The PMA energy and its EF effect arising from the latter mechanism has a great potential to exceed those from the orbital occupancy mechanism in the large SOI and weak exchange splitting materials [78] as well as the small SOI systems [79].

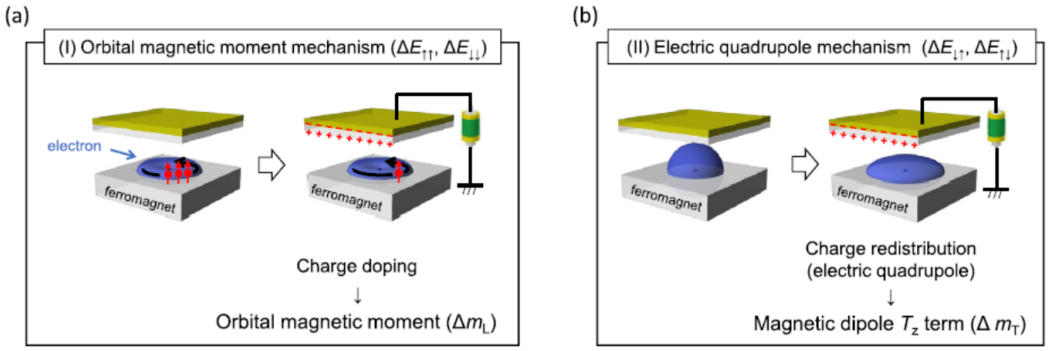

Figure 1.8: The schematics of the considerable mechanisms of EF-induced change in the PMA energy [5, 6].

Recently, these two mechanisms were experimentally verified by using XMCD spectroscopy [78, 80]. It was reported that, when the $3d/5d$-layered transition metals/MgO system is employed, the orbital magnetic moment mechanism cannot completely explained the EF-induced change in PMA [78]. Fig. 1.9(a) shows the XMCD spectra and its numerical integrals at Pt L_3 and L_2 edges of the Fe(0.14)/Pt(0.2)/MgO(5)/polyimide(1500) structure under out-of-plane magnetic field of ±60 mT for $V_G = \pm 200$ V which corresponds to E_G of ~±7 MV/cm in the MgO dielectric. Clear decreases (increases) in XMCD intensities at the both Pt L_3 and L_2 edges were obtained by positive (negative) V_G application, indicating the existence of EF-induced change in magnetic moment in Pt. Figs. 1.9(b) and (c) show V_G dependence of m_L and $m_S - 7m_T$. EF-induced change in $m_S - 7m_T$ was observed whereas there is no significant change in m_L under V_G applications. These results confirmed the existence of the electric quadrupole mechanism in Pt. The first-principle calculation also supports the EF-induced change in m_T dominantly contributes this MA change. Moreover, the sign of EF effect on MA induced by spin-conserved term is opposite to that induced by spin-flip term for the FePt/MgO system [78]. Note that for the calculation of PMA energy

from the second-order perturbation of SOI by the first-principle study, the following equation was often offered [64];

$$E_{\mathrm{PMA}} \approx \xi^2 \sum_{\uparrow,\downarrow} \sum_{o,u} \frac{|\langle\psi_o|L_z|\psi_u\rangle|^2 - |\langle\psi_o|L_x|\psi_u\rangle|^2}{\varepsilon_u - \varepsilon_o}. \tag{1.13}$$

In contrast, in the Fe(0.4)/Co(0.14)/MgO(2) structure, both m_{L} and $m_{\mathrm{S}} - 7m_{\mathrm{T}}$ were modified by V_{G} application as shown in Fig. (d) and (e) [80]. The EF-induced change in the magnetic moments is anisotropic. As the spin momentum has the isotropic distribution to the magnetization direction, the measured $m_{\mathrm{S}} - 7m_{\mathrm{T}}$ change was attributed to be the change in m_{T}. Then, the observed EF-induced change in m_{T} is not by the modulation of $\left(\langle\Delta T_{\downarrow\uparrow}\rangle + \langle\Delta T_{\uparrow\downarrow}\rangle\right)$ term but by the modulation of $\left(\langle\Delta L^2_{\downarrow\downarrow}\rangle - \langle\Delta L^2_{\uparrow\uparrow}\rangle\right)$ term because the large exchange splitting of Co atoms and the full-occupation of Co majority-spin band. These results provides the direct evidence for the application of the conventional Bruno model in the $3d$ transition metal/MgO systems.

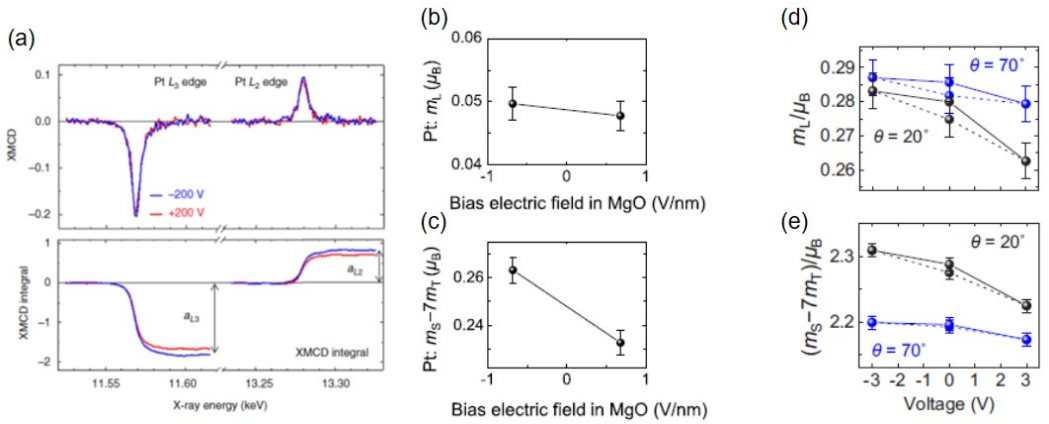

Figure 1.9: (a) XMCD spectroscopy at Pt L edges under an applied gate bias and (b), (c) EF-induced changes in m_{L} and $m_{\mathrm{S}} - 7m_{\mathrm{T}}$ for FePt/MgO system [78]. (d), (e) Voltage-induced changes in m_{L} and $m_{\mathrm{S}} - 7m_{\mathrm{T}}$ for V/Fe/Co/MgO system [80].

1.5 Application of electric-field effect on magnetism for magnetic memory devices

The EF effect on magnetism has attracted much attention in the point of its potential for use in the application for magnetic memory devices. In this section, we introduce some types of magnetic memory devices, including the previous studies on the tunneling magneto resistance (TMR) effect, and the role of the EF effect on magnetism in these memory devices is also discussed.

1.5.1 Magnetic memory devices with magnetic tunneling junction

The discovery of the giant magneto resistance (GMR) effect in 1988 [1, 2] revolutionized our electronics industry and spintronics study. The GMR structure is made of two ferromagnetic layers separated by a spacer non-magnetic metal. The GMR read heads in magnetic hard disk drives (HDDs) (Fig. 1.10(a)) explosively facilitated the improvement in the storage capacity. However, today, the increase in the storage capacity of HDD have slowed to a crawl. In a few decade, a number of alternatives have been suggested [81]. One of the candidates provided by spintronics is magnetic memory devices, such as magnetoresistive random access memory (MRAM) (Fig. 1.10(b)) and racetrack memory (Figs. 1.10(c) and (d)). In magnetic memories, digital data are stored as the magnetization direction of magnetic domains. The most notable characteristic of the magnetization is its non-volatility. The non-volatile feature allows us to consume ultralow stand-by energy, in contrast to dynamic random access memory (DRAM) driving by the charge accumulation/depletion in FETs.

In present magnetic memories, information "reading" operations use the TMR effect. The TMR effect emerges in MTJ, where the nonmagnetic metal layer of the GMR structure is replaced by an insulating layer. Fig. 1.11(a) shows a schematic illustration of the MTJ structure. When two magnetization directions of the ferromagnetic layers are aligned with the parallel configuration, the out-of-plane electrical resistance (R_{P}) gets lower than when two magnetizations are anti-aligned (R_{AP}). In magnetic recording media, these resistance are

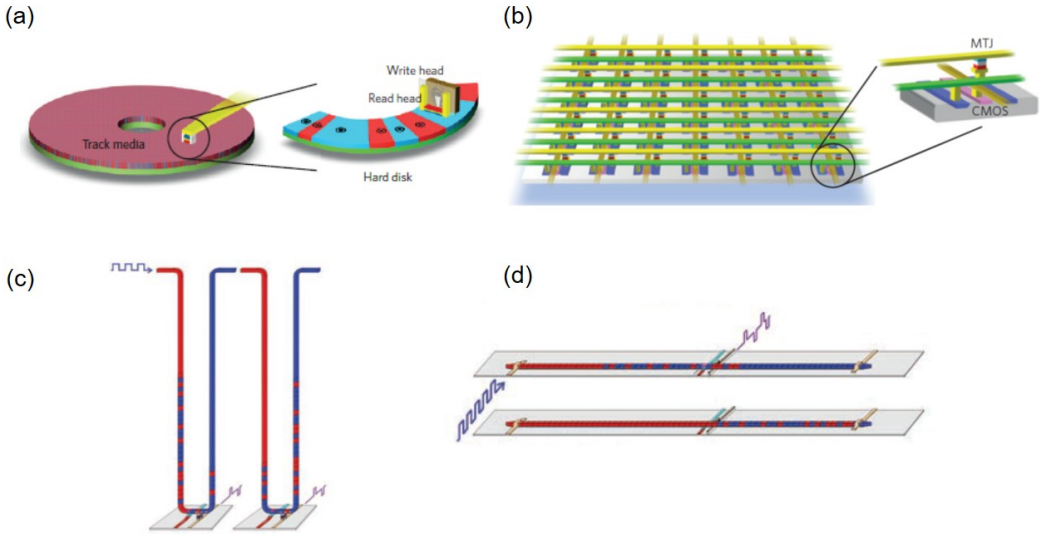

Figure 1.10: (a) Schematic illustrations of (a) HDD, (b) MRAM, and (c) vertical-configuration and (d) horizontal-configuration racetrack memories. Figs. are cited from ref. [82] and ref. [83].

defined as 0 and 1 states in data. MR ratio is defined as

$$\text{MR ratio} = \frac{R_{\text{AP}} - R_{\text{P}}}{R_{\text{P}}}. \tag{1.14}$$

The TMR effect (MR ratio ~14%, only at 4.2 K) was first experimentally observed in the Fe/Ge/Co structure in 1975 [84] by M. Julliere. After a few decade, the RT-TMR effects were shown by using an amorphous Al-oxide as a tunneling barrier [85, 86]. From these discoveries, the experimental and theoretical researches of the TMR effect and the MTJ fabrications were more intensively studied for enhancing the MR ratio [87]. One breakthrough of TMR researches is the observation of the giant TMR ratio (~200%) using a crystalline MgO tunneling barrier in a sputtered CoFe/MgO/CoFe [88] and an epitaxial-grown Fe/MgO/Fe structures [89] in 2004. The spin filtering effect at a crystalline Fe/MgO interface [90], which leads the band-selective transmittance of conduction electrons (Fig. 1.11(b)), exceeded the Julliere limit for the MTJ structures with the 3*d* ferromagnetic electrodes and the amorphous insulating barriers (the MR ratio of ~70%) [84]. In the present fabrication of MTJ devices, a CoFeB/MgO/CoFeB stack is the most common structure [91–96]. In an as-deposited state, the sputtered bottom CoFeB layer is amorphous. When the MgO layer is grown on such

amorphous CoFeB, it is known that MgO is suitable to orient bcc(001) texture [97]. After the deposition of the top CoFeB layer, the bcc(001)-oriented CoFeB/MgO/CoFeB stack can be formed through an appropriate annealing process at a temperature of ~300 – 500°C, resulting in the MR ratio above 600% [93] (Fig. 1.11(c)).

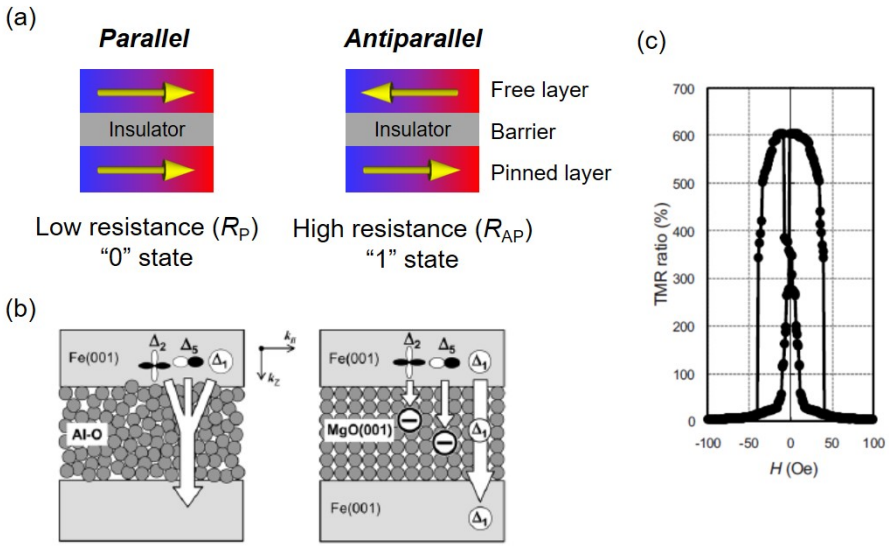

Figure 1.11: Schematics of (a) the MTJ structure and (b) the band-selective transmittance of conduction electrons in an amorphous Al-O and a crystalline MgO barriers. (c) Tunneling magnetoresistance curve in CoFeB/MgO/CoFeB structure at 300 K [93].

In racetrack memories [82], digital data are stored along the ferromagnetic wire (Figs. 1.10(c) and (d)). The DW motion induced by the current pulse injection [98] causes the shift of magnetic domains, while maintaining the bit size, the spacing between two DWs [99]. Information read and write heads are separately located at specific locations. DW-based memories face an issue for the high-density integration because the size of current DW memory devices needs on the order of a few hundred nanometer in contrast to MRAM devices. Many research groups are working for evolving DW memory devices [83, 100]. Recently, nanosized magnetic skyrmion, which is a topological spin texture [101, 102], is expected to be a candidate for racetrack cells thanks to its topological stability and high mobility [50].

1.5.2 Electric-field assisted information writing

The process of information "writing" in the magnetic memories is done by reversing the magnetization direction of one layer (free layer in Fig. 1.11(a)). In general, a magnetic field generated by the induction of the electrical current, which is called Oersted field, has been used for the magnetization reversal. However this method is unsuitable for promoting integration of memories. Development of electronics and spintronics brought us the magnetization reversal by running a polarized electrical current from the top to the bottom and vice versa of the MTJ structure. This effect is called the spin-transfer torque (STT) effect: giving and receiving the spin angular momentum through *s*-*d* exchange interaction between conduction electrons and localized electron in the ferromagnetic layer [103, 104]. A recent perpendicularly-magnetized MRAM device with the STT magnetization-reversal method (STT-MRAM) has achieved a reduction of writing energy consumption to ∼100 fJ/bit [105], which is close to the writing energy for a semiconducting DRAM. Furthermore, another method of the magnetization reversal has been reported in the bilayer consisting of the FM and NM heavy metal layers by the injection of in-plane current into NM layer through the spin-orbit interaction [106, 107], which is called spin-orbit torque (SOT) magnetization switching. The SOT magnetization switch realizes the high-speed operation and high-write-endurance, compared with the STT method. However, magnetization switching by STT or SOT has been required the 10^{10} – 10^{11} A/m^2-orders current density, exhibiting pessimistic Joule heating ($> 10^7 k_B T$) which is dramatically larger than the Landauer limit $\ln 2 k_B T$: a minimum amount of energy required to erase one bit of information asserted by Landauer's principle [108] and even a thermal stability of magnetic memories $60 k_B T$, where k_B is Boltzmann constant [5, 6].

In order to overcome this fundamental problem, the technique of the EF effect on magnetism is attracting a great deal of attention. The first and easiest proposals are that the EF effect on the MA and coercivity is effectively utilized as an assistance of the conventional method using magnetic fields or STT effects [15, 109, 110]. This combination realized an EF manipulation of the spin directions using a static or a pulsed gate EF with a reduction of the switching energy (Fig. 1.12). In 2012, more developed magnetization reversal method using the voltage-induced magnetization precession was demonstrated in the in-plane magnetized FeCo/MgO/Fe MTJ [111] and the perpendicularly-magnetized CoFeB/MgO/CoFeB

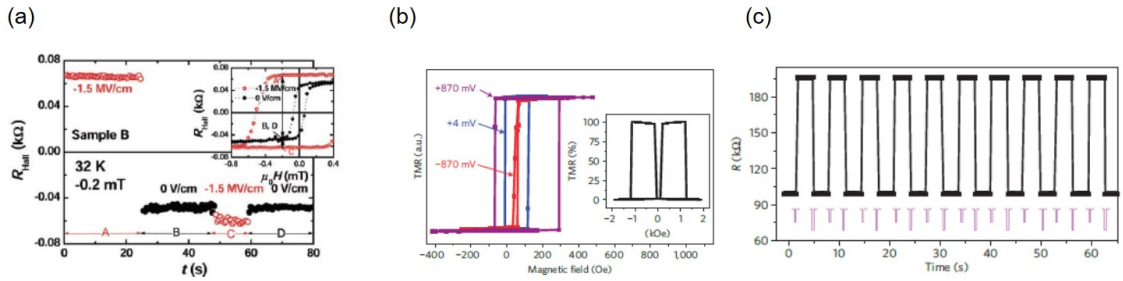

Figure 1.12: (a) The first demonstration of the EF assisted magnetization reversal [15]. This Hall measurement was conducted at 32 K using 4-nm-thick (In,Mn)As and 0.9-μm-thick SiO_2 gate insulator. (b) The first demonstration of the EF assisted STT magnetization reversal in MTJ structure. Normalized minor loops of TMR curve in CoFeB(1.3 nm)/MgO(1.2)/CoFeB(1.6) structure. (c) EF switching of the magnetization and TMR by applying unipolar negative voltage pulses [109].

MTJ structures [112]. Before introducing this method, we explain the expression for the magnetization dynamics: Landau-Lifshitz-Gilbert (LLG) equation. LLG equation is described as

$$\frac{d\boldsymbol{M}}{dt} = -\gamma \boldsymbol{M} \times \boldsymbol{H}_{\text{eff}} + \frac{\alpha}{M_s} \boldsymbol{M} \times \frac{d\boldsymbol{M}}{dt}, \tag{1.15}$$

where γ, $\boldsymbol{M}$, $\boldsymbol{H}_{\text{eff}}$, α are the gyromagnetic ratio, the magnetization vector, the effective field, and damping constant, respectively. The first term indicates the magnetization precesses around the $\boldsymbol{H}_{\text{eff}}$ direction (Larmor precession). The second term means the magnetization relaxation into the $\boldsymbol{H}_{\text{eff}}$ direction (Magnetic damping). When the MA is modified by the EF effect, $\boldsymbol{H}_{\text{eff}}$ is changed by the voltage-torque, resulting the induction of the precessional motion around new $\boldsymbol{H}_{\text{eff}}$.

Fig. 1.13 shows the concept of voltage-induced dynamic magnetization switching using the combination of the EF control of magnetic easy axis and the magnetic precessional motion induced by applying the voltage pulse. Firstly, we assume that the magnetization direction of this sample prefers perpendicular to the plane and stays in up state in the initial state. In addition, when an appropriate gate voltage is applied, the magnetic easy axis can be changed from out-of-plane to in-plane. Fig. 1.13 illustrates the case that the positive gate voltage application induces the decrease in PMA. If the voltage with a short pulse width (~nanosecond) is applied, the magnetization starts to precess around the in-

plane effective field. Then, if the voltage is turned off at the proper timing (the half-turn precession period), the magnetic easy axis gets back to the out-of-plane direction and the magnetization can be stabilized in down state. Fig. 1.14 shows the first demonstration of the voltage-induced dynamic magnetization reversal using an external magnetic bias field to determine the magnetization precession axis [111]. Only negative voltage application induced magnetization switching, confirming the non-existence of the STT contribution (Figs. 1.14(a) and (b)). It has been also confirmed that the switching probability oscillates depending on the voltage pulse width and becomes smaller for the longer duration of the voltage pulse because the relaxed magnetization precession due to magnetic damping causes the decrease in the precession angle (Figs. 1.14(c) and (d)).

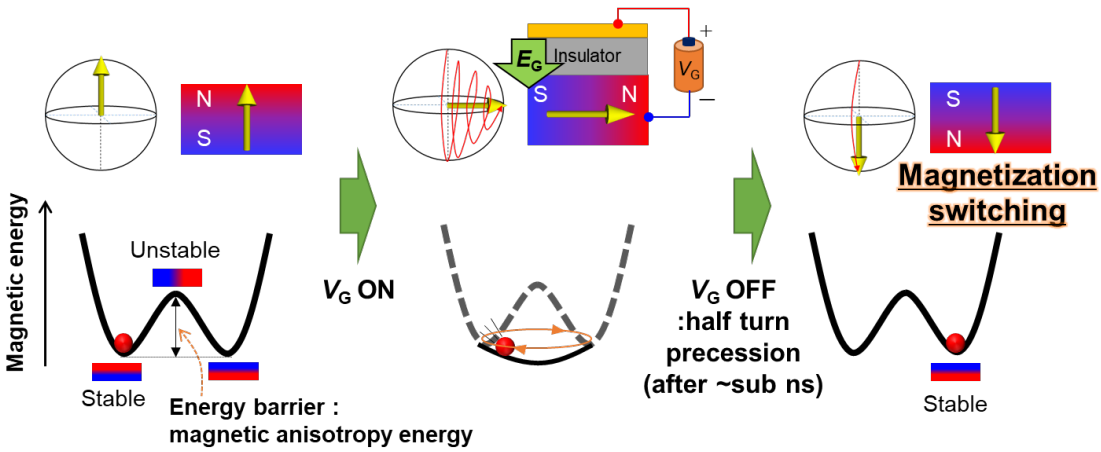

Figure 1.13: Schematics of the concept of the voltage-induced dynamic magnetization switching through the EF effect on magnetic anisotropy and the voltage-induced magnetization precession for a perpendicularly-magnetized film.

The characteristic features of voltage-induced dynamic magnetization switching in the MRAM devices are shown as follows: (i) the switching power is predicted to be ~1 fJ/bit by adopting an areal size and an applied voltage value [5,111], which is smaller than that required in STT switching by two orders of magnitude (experimentally, 6.3 fJ/Vm was achieved in 2.8 nm-thick-MgO based MTJ structure), (ii) the response speed is around nanosecond [111,112], which is also confirmed by the voltage-induced FMR measurement [113], and (iii) the low write error rate (WER) of $10^{-5} - 10^{-6}$ has been demonstrated [114, 115], which is sufficient to realize a practical value 10^{-15} by several verification operations. In addition, it has been

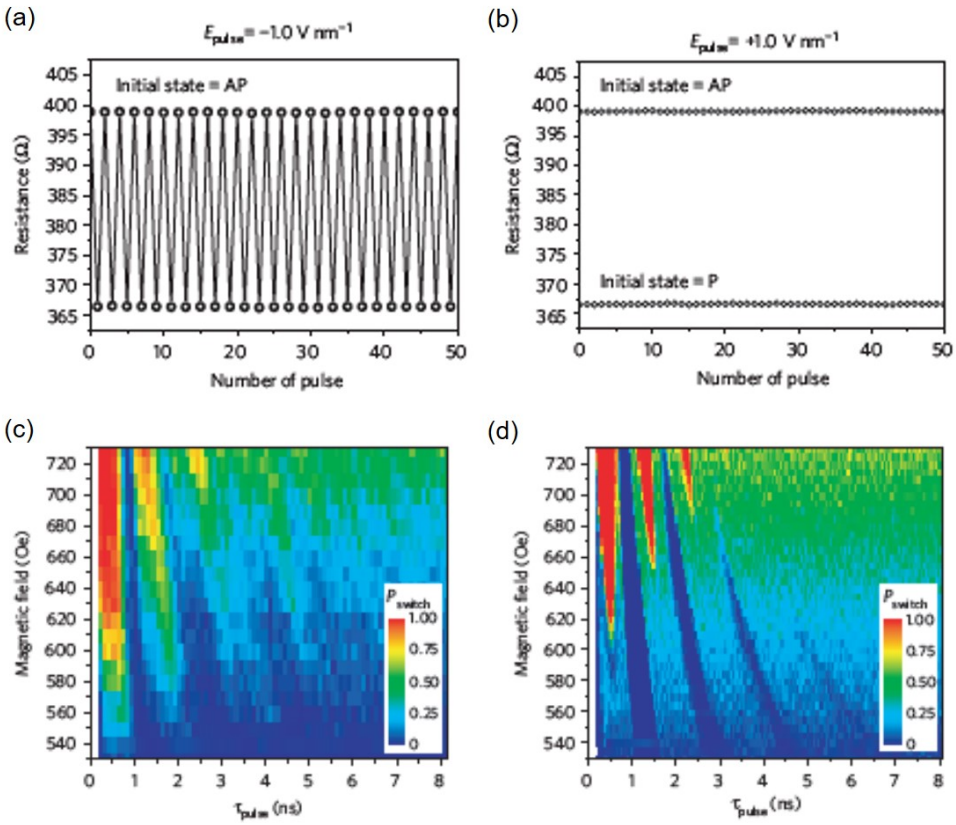

Figure 1.14: The first demonstration of the voltage-induced dynamic magnetization switching [111]. (a),(b) The typical results of repetitive magnetization switching experiments in negative and positive EF pulses, respectively. (c) Experimental and (d) Calculation using a macro-spin model simulation results of switching probability diagram as a functions of the magnetic field and duration time of the voltage pulse.

reported that WER can be reduced by controlling the voltage-pulse shape [116].

For the achievement of purely EF-induced magnetization switching in the nano-sized magnetic film with an efficient PMA ($K_u V > 60 k_B T$), a large efficiency of the EF-control of MA, which is also called the voltage-controlled MA (VCMA) coefficient, (β_S) exceeding 1000 fJ/Vm is fundamentally required. β_S is generally defined as the EF-change in the areal PMA energy divided by E_G. Fig. 1.15 shows the evolution of β_S. Over 1000 fJ/Vm β_S has been demonstrated in some systems by utilizing an electrochemical effect. However, there is only one study with $\beta_S > 1000$ fJ/Vm through the pure electronic mechanism.

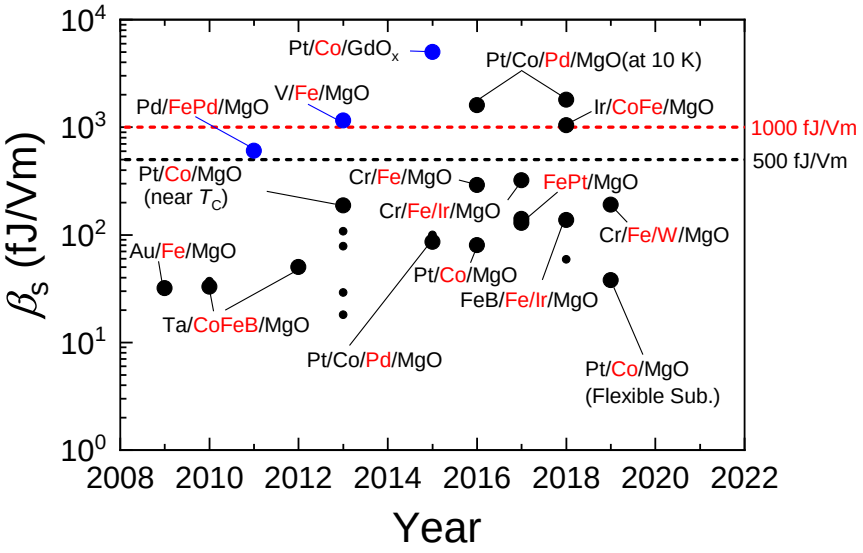

Figure 1.15: The characteristic efficiency of EF-control of MA β_S in various systems [23, 27, 53, 78, 109, 117–133]. Magnetic electrodes of each system, where the gate EF is applied, are shown in red font. β_Ss induced by electrochemical phenomena are colored in blue points.

1.6 Purpose of this work

As mentioned above, the EF control of magnetism, especially controlling of the PMA energy, has been intensively studied because it shows possibilities not only for the realization of more efficient magnetization manipulation but also understanding the interfacial magnetic phenomena originated from spin-orbit coupling. However, most of studies for the EF effect

on magnetism are focusing on the tunnel junctions consisting of 3*d* ferromagnetic metal and alloy electrodes and the MgO tunneling insulator. In order to expand applicability of the EF effect on magnetism, we should investigate the EF effect at the interface of other oxide layers, such as SiO_2 or HfO_2, similar to the study on a semiconductor FET. If the leakage current is further decreased to the extent in ideal FETs, the energy consumption for manipulating magnetization will eventually reach $\sim CV_G^2 = 10$ aJ/bit, where C is a capacitance of a bit cell [134]. In addition, assuming the racetrack memories, the MgO-based MTJ structure is not necessary for EF-assisted information writing. Therefore, we hold two goals in this doctoral thesis: (i) the realization of enhancing the efficiency of the EF effect on MA and the clarification of its microscopical mechanism using 3*d* ferromagnetic Co or 5*d* heavy metal Pt electrode and some types of oxide dielectrics, (ii) the demonstration of brand new EF control of magnetic properties besides MA in the solid-state capacitor structures that have a high-k dielectric HfO_2 layer. Outline of this thesis is shown as follows.

In Chapter 1, we have briefly reviewed the introduction for this thesis. After that, experimental techniques used in this study are explained in Chapter 2. In Chapter 3, we investigate the EF control of MA in 5*d* transition metal Pt stacked on the ferromagnetic Co layer with several types of the oxide gate insulators. The results of x-ray absorption spectroscopy in Pt are also discussed. In Chapter 4, we clarify the mechanisms of the EF effect on magnetism, notably the interfacial charge accumulation and the electrochemical effect, in the Co/HfO_2 structure by changing the fabrication temperature of the HfO_2 dielectric layer. In Chapter 5, we investigate the electrostatic EF control of the exchange bias effect in the similar magnetic stack as Chapter 4. The mechanism of the EF-induced change in the exchange bias field is different from the magnetoelectric effect and the thermally-activated effect. In Chapter 6, we demonstrate the modulation of the interfacial spin-orbit torque by the EF-induced oxide migration in Pd/Co/Pd system. At the end, we summarize obtained results and conclude this study with the future works in Chapter 7.

Chapter 2

Experimental method

2.1 Fabrication of stacked films

We fabricated all of the magnetic stacked films using the sputtering method and some dielectric insulating layers using the atomic layer deposition (ALD) method. In this section, we introduce the essential principles for the method of the thin film deposition and the fabrication processes for device patterning.

2.1.1 Sputtering

Sputtering is a physical vapor deposition method to create thin film stacks. Schematic image of a sputtering system is shown in Fig. 2.1. Before the deposition, the vacuum chamber is purged to a ultra high pressure to remove the air and H_2O and then filled with a high purity inert gas (Ar, Xe, etc.). By applying voltage between two electrode, the inert gas gets ionized. The ionized gas atoms are driven to the target by the applied electric field and hit the target. Then, the particles of the target are ejected and condensed on the substrate. Sputtering deposition generally gives thin films with a better adhesion on the substrate than films fabricated using evaporation techniques and is suited for the mass production.

Direct current (dc) sputtering which uses the dc current as a power source is basically used for the deposition. However, it has primary limitation that the insulating layer (e.g. SiO_2, MgO) due to the charge up effect. In order to overcome this problem, the radio frequency (rf) sputtering method was developed. Alternating the electrical potential by the application

of rf bias can clean the charge up at the surface of insulating targets. The radio frequency at 13.56 MHz is generally used. Magnetron sputtering technique uses a magnet behind the target material. Magnetic field traps the secondary electrons and then promotes the ionization of the inert gas, resulting in the faster deposition and the suppression of the substrate heating effect.

In this study, all of the magnetic stacked films were fabricated by rf magnetron sputtring because of the deposition of MgO layer. The base pressure of the main chamber of our sputtering machine was $\sim 10^{-6} - 10^{-7}$ Pa and the deposition pressure was around 0.2 Pa (Xe) and 0.6 Pa (Ar), respectively. The thickness of thin layers was determined from the deposition rate of each materials which was monitored using the quartz crystal resonator. In addition, we carried out the atomic force microscopy (AFM) and x-ray reflectivity (XRR) measurement for calibrating the thin film thickness. By comparing the thicknesses between the values calculated from the deposition rate and those measured by the AFM or XRR measurement, we determined the actual thickness of the deposited stacked films for each substance.

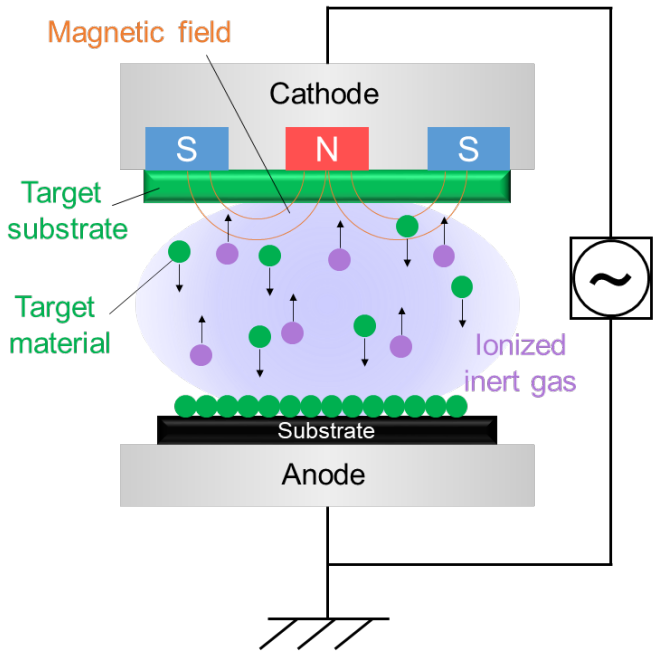

Figure 2.1: A schematic illustration of rf magnetron sputtering.

2.1.2 Atomic layer deposition

Atomic layer deposition (ALD) is a chemical vapor deposition technique for the growth of high-quality thin films and one of the key processes in the fabrication of some semiconductor devices [135]. The characteristic feature of ALD is that two reactants, called as precursors, are alternately dosed and always separated by gas purging. After the excess gas is pumped away by inert gas purging to avoid a gas reaction, the second precursor gas is periodically introduced into the chamber and chemisorbed on the top of the first layer. On the surface, there is a chemical reaction between two precursors, resulting in forming one monolayer coating layer (Fig. 2.2). Finally, one ALD cycle is completed after the excess gas and byproducts are pumped away. This procedure can be repeatedly done as many times as necessary to deposit the desirable thickness. This self-limiting growth nature enables the control of the thickness in the atomic layer scale and the conformal and pin-hole free lamination of the samples.

In this study, we use tetrakis(dimethylamino)hafnium: $Hf[N(CH_3)_2]_4$ and trimethylalminium: $Al(CH_3)_3$ as the main precursors and H_2O as the oxidant precursor, respectively. The reaction formulas are shown below.

$$Hf[N(CH_3)_2]_4 + 2\,H_2O \longrightarrow HfO_2 + 4\,HN(CH_3)_2$$
$$2\,Al(CH_3)_3 + 3\,H_2O \longrightarrow Al_2O_3 + 6\,CH_4$$

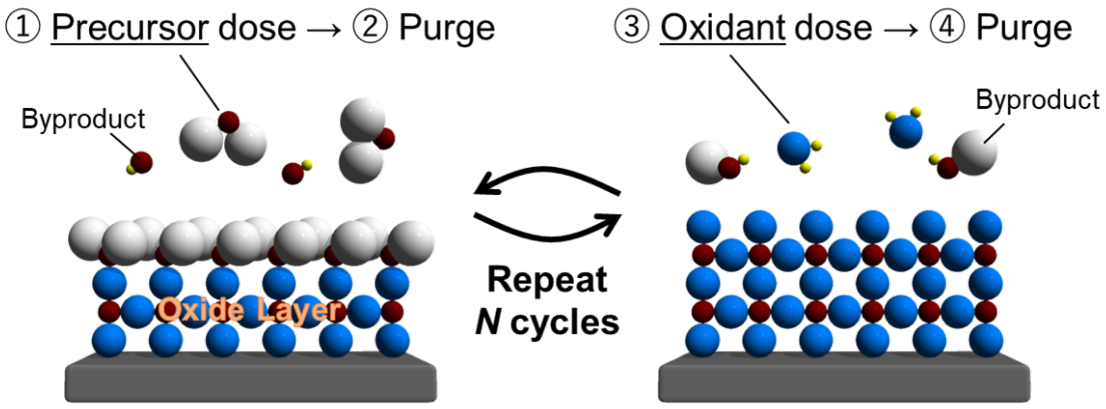

Figure 2.2: A schematic overview of the atomic layer deposition cycle.

2.1.3 Fabrication process for making electric-field effect devices

Most of the deposited films were patterned into the capacitor mesa structure for the experiment of the electric-field (EF) effect using the photolithography and Ar ion milling. The procedure is shown below. Details of the fabrication process is noted in each chapter.

1. After the sputtering deposition, the sample was covered with the positive photoresist (S1813G; Shipley, Ltd.). A spin coater (MIKASA Co., Ltd.) was used to make the photoresist thinner and flatter at 5000 rpm for around 40 sec. After that, the sample was put on a hot plate and baked for around 5 min. at 90°C (Chapter 3-5) or 60°C (Chapter 4, 6). The photoresist protects the sample from additional chemical reaction such as a natural oxidation.

2. A photomask was put on the sample surface. Subsequently, ultraviolet rays were irradiated for 20-30 sec. using the mask aligner M-1S (MIKASA Co., Ltd.).

3. The sample was put into microposit MFCD-26 developer (Rohm and Haas Co.) for about 15 sec, and then into pure water for about 5 sec. The photoresist on exposed parts was rinsed away in this process.

4. The sample was etched with the Ar ion milling apparatus IBE-NS10-TU-DC (EIKO Engineering). The area covered with the photoresist was not etched because the thickness of the photoresist is about $1 - 10$ μm which is much thicker than sample thickness (~10 nm).

5. After removing residual photoresist by a ultrasonic cleaner in acetone and ethanol solutions, the sample was covered with the dielectric oxide layer (~50 nm) by using ALD at 150°C (Chapter 3-5) or 60°C (Chapter 4, 6).

6. Again, the photoresist-S1813G was coated on the sample and baked. Photolithography process was performed using a photomask with the hole cut into a shape of the top electrode.

7. The top electrode was formed by the lift-off method. We use rf sputtering (Ta, Pd, Pt) or resistance heating evaporation system (Cr, Cu, Au).

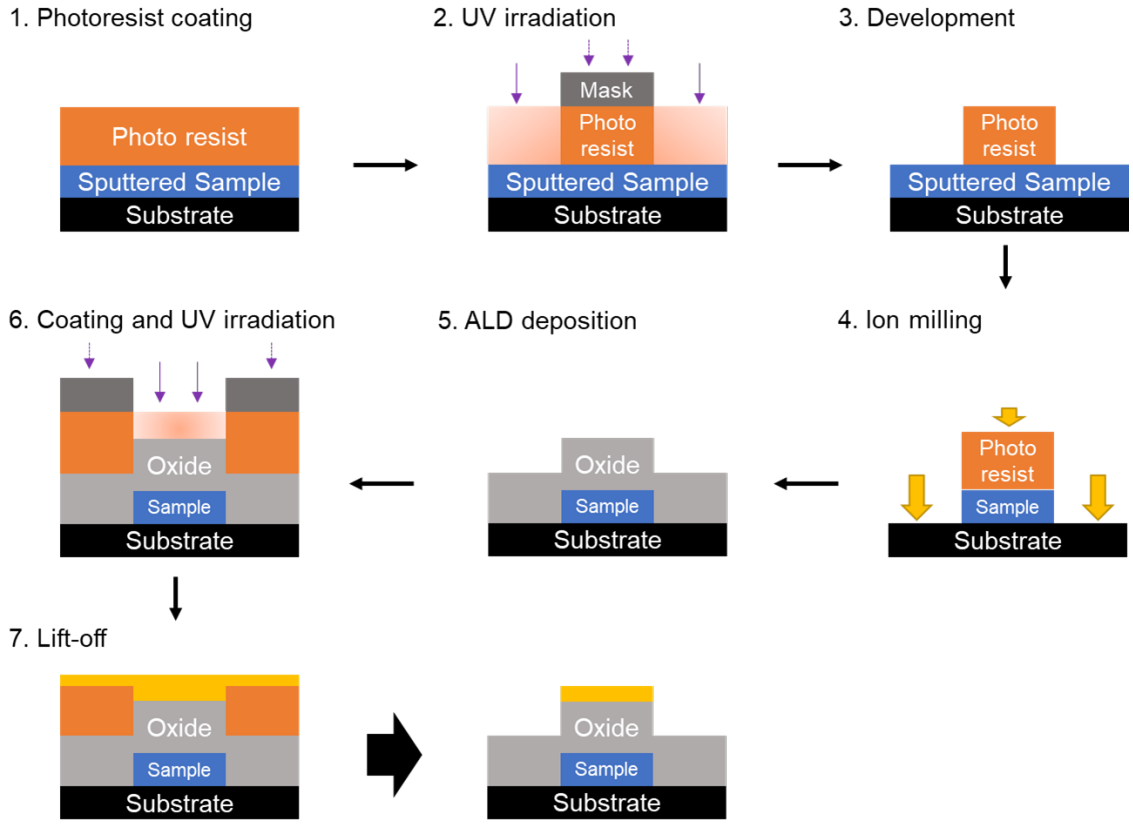

Figure 2.3: A procedure for an EF-field effect device fabrication.

A typical device image for the transport measurement (Sec. 2.4) is shown in Fig. 2.4.

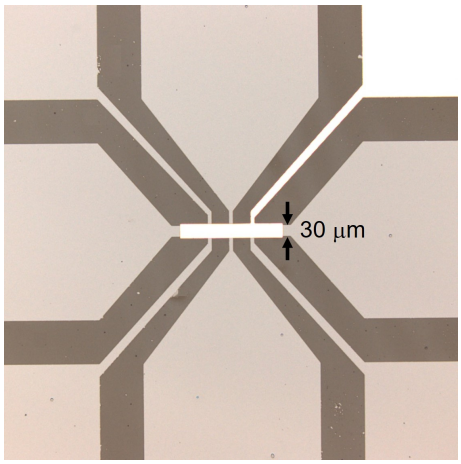

Figure 2.4: A microscope image of a typical capacitor structure cut into a Hall bar shape.

2.2 Structural and chemical analysis

2.2.1 X-ray diffraction

X-ray diffraction (XRD) is a nondestructive method for characterizing the crystal structure. XRD is base on the Bragg's law described as

$$2d \sin\theta = n\lambda, \tag{2.1}$$

where d is a lattice spacing, θ is an angle between the x-ray and the normal on the reflection plane, n is an integer, and λ is an x-ray wavelength (Fig. 2.5), respectively. By the XRD measurement and applying above relationship, we can deduce the crystallinity of the sample. When an x-ray is applied to almost parallel to the sample plane ($\theta < 10°$), x-ray only penetrates around a few nm into the sample. The measurement in this configuration is called x-ray reflectivity of reflectometry (XRR), and XRR gives us the information of each layer thickness of the stacks and the roughness of the interface. In this study, XRD and XRR measurement was performed by using SmartLab (Rigaku Corp.) with Cu-Kα radiation.

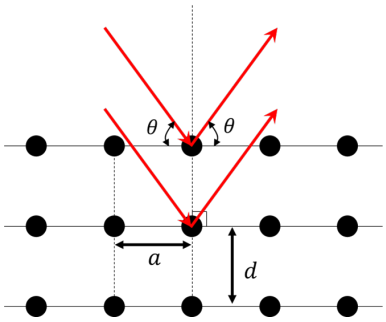

Figure 2.5: Schematics of x-ray diffraction according to Bragg's law.

2.2.2 X-ray photoelectron spectroscopy

When a monochromatic light is irradiated to the materials, the deep-core electron is excited to a vacuum state above Fermi level and a photoelectron is emitted (photoelectric effect). X-ray photoelectron spectroscopy (XPS) is a technique for analyzing the surface state and chemical state by detecting this photoelectron, using x-ray as a probe light. When the photoemission

effect takes place, the energy conservation law is expressed as below;

$$E_{\mathrm{k}}^{\mathrm{V}} = h\nu - E_{\mathrm{b}} - \Phi, \tag{2.2}$$

where $E_{\mathrm{k}}^{\mathrm{V}}$, $h\nu$, E_{b}, and Φ are the kinetic energy of the photoelectron, the photon energy, the electron binding energy relative to the Fermi level, and the work function of the sample, respectively. Photoelectron spectra are recorded by counting emitted electrons over a range of the kinetic energies of electrons. From the intensity of a photoelectron peak and the binding energy, we can determined the chemical state and the elemental identity. The electron energy in the XPS analysis is generally located in the region from 30 to 3000 eV. The XPS analyzing depth is limited from the top 1-10 nm of the samples because these electrons have a strong interaction in the solids. The escaping length depends on the element. Therefore it might be impossible to get the spectra of the target which is in the deeper region of the stacked structure. To overcome this problem, ion-sputtering method and/or angle-resolved method were often used [136]. Ion-sputtering XPS is an easy way for evaluating the depth profile of the chemical information in the sample. However, in ion-sputtering XPS, highly energetic ions hit the surface and break chemical bonds, resulting some structural damages and chemical changes such as a reduction effect. In contrast, angle-resolved XPS is a non-destructive measurement method that varies the emission angle and the escape depth of photoelectrons with reference to the analyzer (Fig. 2.6). In this study, if target materials were located under the oxide capping layer, Ar ion-etching (2 kV) was firstly conducted to etch the oxide layer, and then angle-resolved XPS was performed with the irradiation of Al-$K\alpha$ x-ray.

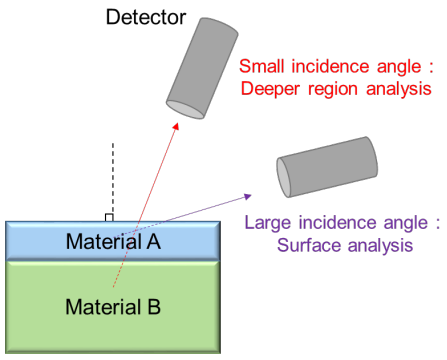

Figure 2.6: Schematics of angle-resolved x-ray photoelectron spectroscopy.

2.3 Magnetization measurement

The magnetization measurement was performed using Superconducting Quantum Interference Device (SQUID) magnetometer. A SQUID device, consisting of the superconducting ring with one or two Josephson junctions, realizes the high sensitive magnetization measurement in exchange for requiring a cryogen. The magnetic moment of the sample taken by an attached pick-up coil changes the number of magnetic flux lines penetrating Josephson junction ring, leading to the change in the Josephson current and potential. Finally, the sample magnetization is converted into a voltage signal through the secondary detection coil.

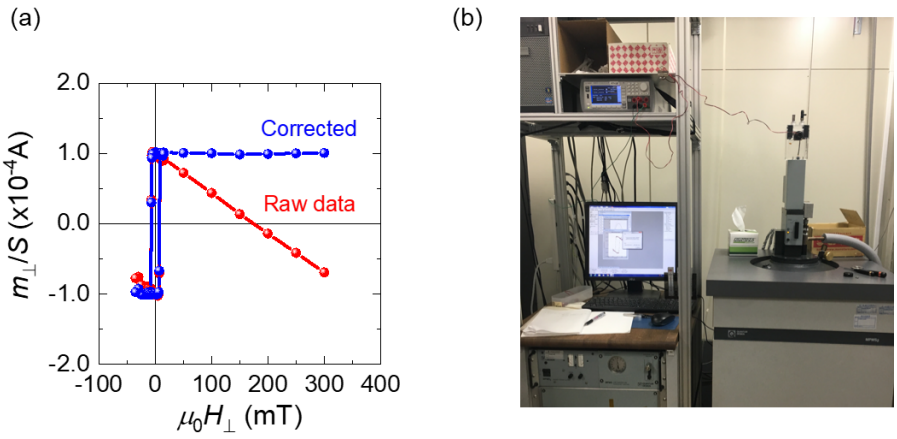

Figure 2.7: (a) The results of the magnetization measurement for the perpendicularly magnetized film. (b) The image of the magnetization measurement system.

In this work, a Magnetic Property Measurement System (MPMS; Quantum Design, Inc.) was utilized. We used a typical rso unit in SQUID measurement in which, to ensure the uniformity of the magnetic field, the amplitude and frequency of the vibration is set to 1.5 cm and 1.0 Hz, respectively. We defined the average value of three times rso measurements as the measured moment of the sample. Because of the larger volume of the substrate, the diamagnetic contribution of the substrate which is proportional to the external magnetic field exceeds the ferromagnetic moment (Fig. 2.7(a)). Therefore, in order to get a real magnetic moment of the sample, we have to subtract the diamagnetic component of the substrate. We calculated the diamagnetic contribution from the linear fitting to the high field data, and subtracted it from the raw data. The corrected ferromagnetic moment is shown as blue plots

in Fig 2.7(a). For the experiment of the EF effect on the magnetic moment, the wiring box was attached to the top of the rso unit (shown in Fig. 2.7(b)). A gate voltage was applied by a Keysight B2901A Precision Source/Measure unit.

2.4 Electrical transport measurement

2.4.1 Longitudinal resistance measurement

The longitudinal resistance was measured with a conventional 2-probe and/or 4-probe method. The schematic illustration of the transport measurement is depicted in Fig. 2.8. In the 4-probe method, the separation of force and sense pads can minimize the influence of contact resistance. While a constant electric current (I) is applied between terminal-1 and terminal-2, the longitudinal voltage drop from terminal-1 to terminal-2 ($V_{2\text{wire}}$) and from terminal-3 to terminal-4 (V_{xx}) were quantified. 2-wire resistance (R_{sheet}) is expressed as $R_{2\text{wire}} = V_{2\text{wire}}/I$. The sheet resistance ($R_{\text{sheet}}$) is calculated from the longitudinal 4-wire resistance ($R_{4\text{wire}} = V_{xx}/I$) as below;

$$R_{\text{sheet}} = \frac{\rho_{xx}}{t} = \frac{w}{L} R_{4\text{wire}}, \tag{2.3}$$

where ρ_{xx}, t, w, L represent the longitudinal resistivity, the thickness of the sample, the channel width, and length, respectively.

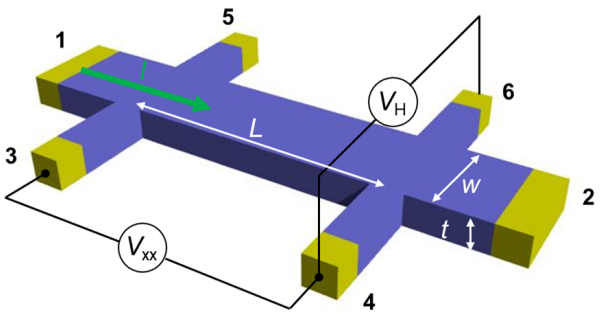

Figure 2.8: Schematics of the electrical transport measurement.

2.4.2 Hall measurement

The Hall measurement is one of the powerful tools to characterize materials properties. By quantifying the voltage between terminal-4 and terminal-6 (V_{Hall}) (Fig. 2.8), we can get a transverse Hall resistance R_{Hall} (= V_{Hall}/I). When a constant current is applied into the ferromagnetic channel which have the magnetization M, R_{Hall} is generally expressed as

$$R_{\mathrm{Hall}} = \frac{R_{\mathrm{OHE}}}{t}\mu_0 H_{\perp} + \frac{R_{\mathrm{AHE}}}{t} M\cos\theta + \frac{R_{\mathrm{PHE}}}{t}(M\sin\theta)^2\cos 2\varphi, \tag{2.4}$$

where $\mu_0 H_{\perp}$ is the out-of-plane component of the external magnetic field, θ is the angle between M and z-axis, φ is the angle between xy-plane projection of M and the current direction, R_{OHE}, R_{AHE}, and R_{PHE} are the proportionality factor of the ordinary Hall effect, the anomalous Hall effect, and the planer Hall effect, respectively. The first term shows the ordinary Hall resistance arising from the Lorentz force acting on the conduction carriers. R_{OHE} is proportional to n^{-1}, where n is a carrier density of the sample, so R_{OHE} of the ferromagnetic metal is quite smaller than that of the semiconductors, because of the large carrier density ($\sim 10^{23}$ cm^{-3}). The ordinary Hall effect depends on the z component of the magnetic field. We subtracted the component of the ordinary Hall effect by the linear fitting to the high field data. The second and third terms show the magnetoresistance derived from the anomalous Hall effect and the planer Hall effect arising due to the spin-orbit interaction and the spin dependent scattering [137]. The component of the planer Hall effect is even function against the coordinates along a magnetic field line. Thus, the component of the anomalous Hall effect can be separated by symmetrization process. Fig. 2.9 shows typical anomalous Hall resistance curves for the sample whose easy axis is perpendicular to the plane direction (Fig. 2.9(a)) and in-plane direction (Fig. 2.9(b)), respectively.

In this study, most of the electrical transport measurements were performed inside Physical Property Measurement System (PPMS; Quantum Design, Inc.) (Fig. 2.10). To prevent the impurities contamination, the chamber was kept in the vaccum of ~10 Torr by using a rotary pump. We employed two types of transport measurements; the dc measurement (Chap. 3-6) and the ac measurement (Chap. 3 and 6). In the dc measurement, we used a Keithley 2401 source meter for the application of the drain-source current and the gate bias, and a Keithley

2110 digital multimeter for the voltmeter. In the ac measurement, an ac current was applied by a Keithley 6221 source unit and the Hall voltage was recorded by SR830 DSP digital lock-in amplifier (Stanford Research Systems, Inc.). To assure a uniform EF application, we have to keep the bias voltage between drain and source terminals smaller than the gate voltage. In our typical samples, the voltage drop from the source terminal to the drain terminal was less than 0.1 V while the gate voltage was 5-15 V.

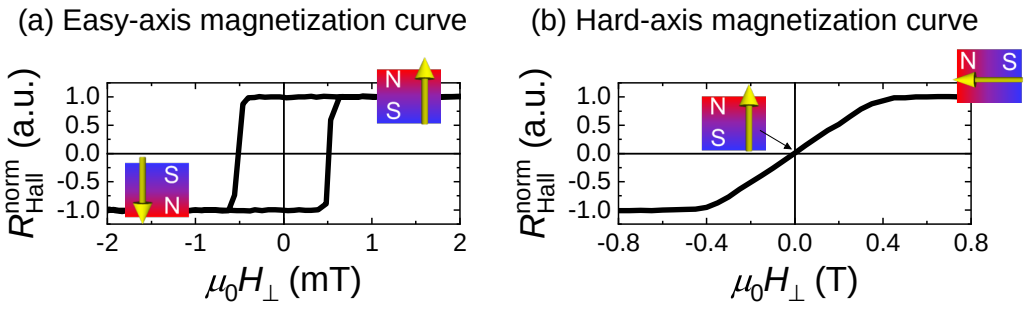

Figure 2.9: (a) Easy-axis anomalous Hall curve (b) Hard-axis anomalous Hall curve.

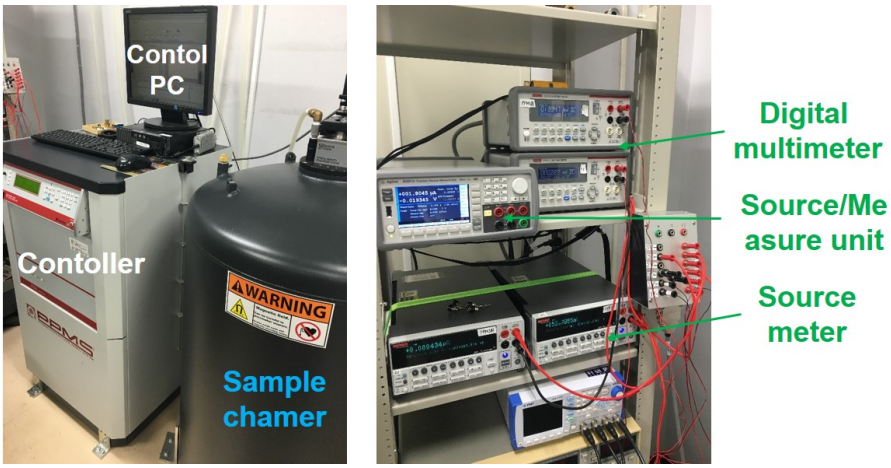

Figure 2.10: Sample chamber and controller of PPMS and electrical instruments.

2.5 Estimation of magnetic anisotropy energy

Magnetic anisotropy (MA) energy, which is the required energy in saturating the total magnetic moment from the easy-axis direction to the hard-axis direction, is expressed as following equation,

$$K_{\mathrm{u}}V = \int_0^{m_{\mathrm{s}}} \mu_0 H_{\mathrm{hard}} \mathrm{d}m, \tag{2.5}$$

where V is the volume of the ferromagnetic layer, m_{s} is the saturation magnetic moment, and H_{hard} is the external magnetic field along the direction of the magnetization hard axis. When we conduct a Hall measurement, Eq. 2.5 is expressed as below:

$$K_{\mathrm{u}}V = m_{\mathrm{s}} \int_0^1 \mu_0 H_{\mathrm{hard}} \mathrm{d}R_{\mathrm{Hall}}^{\mathrm{norm}}. \tag{2.6}$$

Therefore, the magnetic anisotropy energy per unit area can be determined from following equation,

$$tK_{\mathrm{u}} = \frac{tm_{\mathrm{s}}}{V} \int_0^1 \mu_0 H_{\mathrm{hard}} \mathrm{d}R_{\mathrm{Hall}}^{\mathrm{norm}}, \tag{2.7}$$

$$= tM_{\mathrm{s}} \int_0^1 \mu_0 H_{\mathrm{hard}} \mathrm{d}R_{\mathrm{Hall}}^{\mathrm{norm}}, \tag{2.8}$$

$$= \frac{m_{\mathrm{s}}}{S} \int_0^1 \mu_0 H_{\mathrm{hard}} \mathrm{d}R_{\mathrm{Hall}}^{\mathrm{norm}} = \frac{m_{\mathrm{s}}}{S} \times \frac{\mu_0 H_{\mathrm{k}}}{2} \tag{2.9}$$

Here, t, S, M_{s}, and $\mu_0 H_{\mathrm{k}}$ show the ferromagnetic thickness, the total area of the sample, the saturation magnetization, and the anisotropy field, respectively. In this work, the value of m_{s}/S was directly measured by the SQUID magnetometer (Sec. 2.3). $\mu_0 H_{\mathrm{k}}$ was determined from the hard-axis R_{Hall} curves measured by the anomalous Hall measurement (Sec. 2.4). Note that the calculation procedure is slightly different depending on the direction of the magnetic easy axis. In this study, we defined $\mu_0 H_{\mathrm{k}} < 0$ (> 0) and $K_{\mathrm{u}} < 0$ (> 0) when the easy axis is in-plane (out-of-plane) direction, indicating that the increase (decrease) in the MA energy means the enhancement (reduction) of the perpendicular MA (PMA).

Easy axis: In-plane direction

The hard-axis magnetization curve was measured by sweeping an out-of-plane magnetic field (shown in Fig. 2.11(a)). We estimated the anisotropy field from the integration of the shaded area in the normalized R_{Hall} curve (Fig. 2.11(b)).

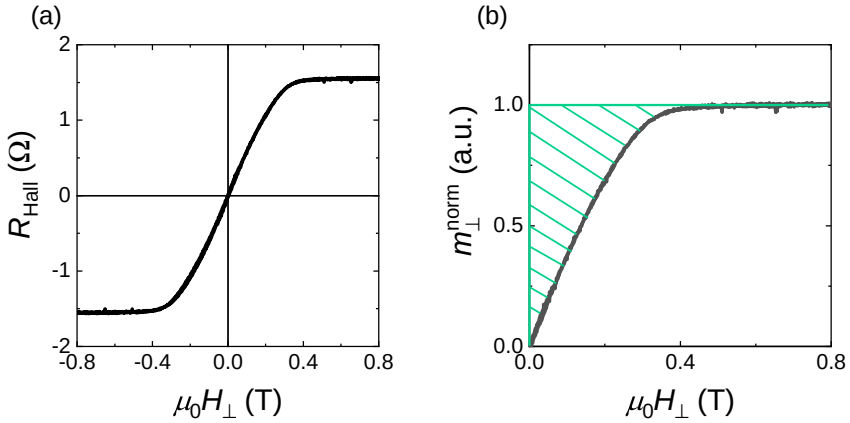

Figure 2.11: (a) Out-of-plane magnetic field dependence of the Hall resistance curve. (b) Out-of-plane magnetic field dependence of the normalized Hall resistance curve. The shaded area represents $\mu_0 H_{\mathrm{k}}/2$ ($\mu_0 H_{\mathrm{k}} < 0$).

Easy axis: Out-of-plane direction

Fig. 2.12(a) shows the R_{Hall} curve measured by sweeping an in-plane magnetic field. The normalized in-plane magnetization curves $m_{\parallel}^{\mathrm{norm}}$ were calculated from following equation,

$$m_{\parallel}^{\mathrm{norm}} = \sin\left(\arccos\left[\frac{R_{\mathrm{Hall}}}{R_{\mathrm{Hall}}(\mu_0 H_{\parallel} = 0\ \mathrm{T})}\right]\right). \tag{2.10}$$

We estimated the anisotropy field from the integration of the shaded area of this normalized R_{Hall} curve illustrated in Fig. 2.12(b).

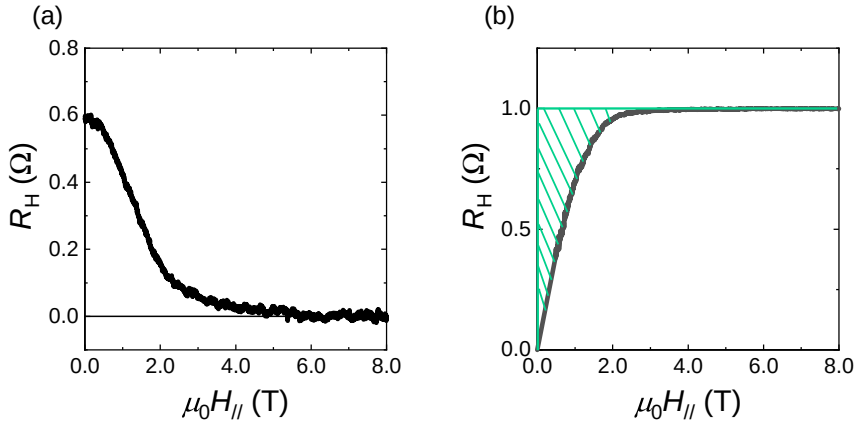

Figure 2.12: (a) In-plane magnetic field dependence of the Hall resistance curve. (b) In-plane magnetic field dependence of the normalized Hall resistance curve. The shaded area represents $\mu_0 H_k/2$ ($\mu_0 H_k > 0$).

2.6 Estimation of electric-field effect efficiency on magnetic anisotropy

In order to estimate the EF effect on MA, the efficiency of EF control of MA (β_S), which is also called the voltage-controlled MA (VCMA) coefficient, is generally used. β_S is expressed as below,

$$\beta_S = \frac{|\Delta(tK_u)|}{E_G}, \tag{2.11}$$

where E_G is a gate electric field applied to the surface of the ferromagnetic electrodes. When the insulating layer is consist of one dielectric material, e.g. the Fe/MgO/Au structure, E_G is easily expressed as V_G/t_{ins}, where V_G and t_{ins} are the gate voltage and the thickness of a dielectric layer. Next, we consider the bilayer capacitor structure whose equivalent circuit is illustrated in Fig. 2.13(a). The bottom dielectric layer (C_2) is faced the target magnetic electrode. The areal capacitance of each layer ($C_{1(2)}/S$) and the voltage drop ($V_{1(2)}$) have

following relationship:

$$\frac{C_1}{S} = \frac{\varepsilon_0 \varepsilon_{r1}}{t_1}, \tag{2.12}$$

$$\frac{C_2}{S} = \frac{\varepsilon_0 \varepsilon_{r2}}{t_2}, \tag{2.13}$$

$$V_1 + V_2 = V_\mathrm{G}, \tag{2.14}$$

where S, ε_0, $\varepsilon_{r1(r2)}$, and $t_{1(2)}$ represent the area of the capacitor, the vacuum permittivity, the relative permittivity of each dielectric material, and the thickness of each dielectric layer, respectively. By applying the principle of charge conservation, we can get $C_1 V_1 = C_2 V_2$. Thus, the bottom voltage drop V_2 is described as

$$V_2 = \frac{\varepsilon_{r1} t_2}{\varepsilon_{r1} t_2 + \varepsilon_{r2} t_1} V_\mathrm{G}. \tag{2.15}$$

In this case, the applied electric field E_G is expressed as V_2/t_2. Therefore, β_S can be described as follows:

$$\beta_\mathrm{S} = \left(\frac{\varepsilon_{r2}}{\varepsilon_{r1}} t_1 + t_2 \right) \frac{|\Delta(tK_\mathrm{u})|}{V_\mathrm{G}}. \tag{2.16}$$

In this study, β_S was evaluated from the slope of the linear relationship between E_G and the PMA energy (shown in Fig. 2.13(b)). We defined the application of the positive (negative) V_G and E_G as the increase (decrease) in the electron density of ferromagnetic layers.

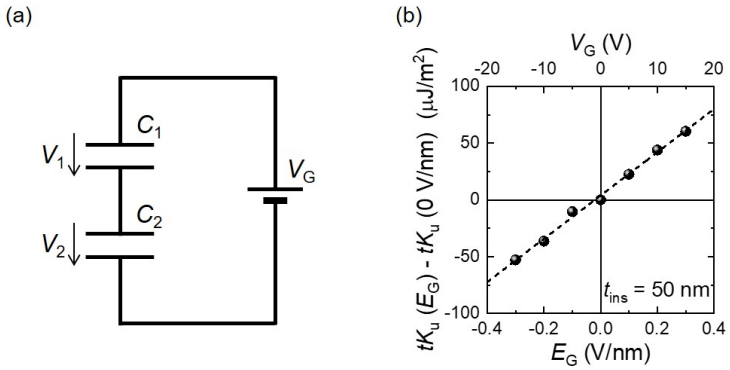

Figure 2.13: (a) Schematic of the equivalent circuit of the bilayer dielectric capacitor structure composed of a series of capacitances. (b) The gate electric field dependence of the change in the areal magnetic anisotropy energy. Dashed line shows the linear fitting of the data.

2.7 Synchrotron radiation measurement

2.7.1 X-ray absorption spectroscopy

X-ray absorption spectroscopy (XAS) is an inner-shell spectroscopy. Inner-shell means that an x-ray interacts primarily with a deep core electron rather than with electrons in a valence state. This spectroscopic method is often used to obtain information about the electronic structure in the materials. An incoming photon by irradiating x-ray interacts with a deep core electron. When the x-ray with a specific energy is irradiated, the excited electron is promoted to some unoccupied states above the Fermi energy and produces a hole in the state. A short time later (about 1 fs), a higher lying electron decays into the hole and emits a x-ray fluorescence. At this time, the absorption spectra shows the dramatic enhancement This edge is called by which core electron is excited; the principal quantum numbers: $n = 1, 2, 3$ correspond to the K-, L-, M-edges, respectively. The absorption spectrum as a function of the incident x-ray energy realizes the element-specific study because each element has a characteristic set of excitation and fluorescence energy.

In the Pt compound systems, L-edge is usually used, which is the main target of Chapter 3 in this study. Since the inner $2p$ core is split into $2p_{1/2}$ and $2p_{3/2}$ by coupling orbital angular momentum and spin angular momentum through the spin-orbit interaction, we can directly observe L-edge spectrum as the two peaks; L_3-edge ($2p_{3/2} \rightarrow 5d$ transition, ~11.57 keV) and L_2-edge ($2p_{1/2} \rightarrow 5d$ transition, ~13.28 keV).

2.7.2 X-ray magnetic circular dichroism

In optics research, the word “dichroism” means the changes in the absorption between left-hand and right-hand circularly polarized lights. The polarized-dependent x-ray absorption is called x-ray magnetic circular dichroism (XMCD). The XMCD measurement provides quantitative information about the magnetic properties, and the magneto-optical sum rule allows to separate the spin and orbital contributions to the total magnetic moment of the

sample using the integrated XAS and XMCD spectra as following equations [68, 69],

$$m_{\mathrm{S}}^{\mathrm{eff}} = -n_{\mathrm{Pt}}\mu_{\mathrm{B}}\left(\frac{A_{L_3}-2A_{L_2}}{S_{L_3+L_2}}\right), \tag{2.17}$$

$$m_{\mathrm{L}} = -\frac{2}{3}n_{\mathrm{Pt}}\mu_{\mathrm{B}}\left(\frac{A_{L_3}+A_{L_2}}{S_{L_3+L_2}}\right), \tag{2.18}$$

$$n_{\mathrm{Pt}} = \alpha S_{L_3+L_2}, \tag{2.19}$$

where $m_{\mathrm{S}}^{\mathrm{eff}}$ and m_{L} are the effective spin magnetic moment and the orbital magnetic moment, respectively. Further, S_{X}, A_{X}, and μ_{B} are the white-line intensity of XAS, XMCD intensity at the L_3 and L_2 edges, and Bohr magneton. n_{Pt} represents the number of holes in the Pt-5d orbitals. α is a proportionality coefficient between n_{Pt} and the XAS integration. In this study, n_{Pt} was estimated on the assumption that 2.7-nm-thick Pt facing on the Co layer, which was fabricated by our sputtering machine [138], has the hole number of the bulk Pt (= 1.8) [139, 140].

The angle dependent measurements in external magnetic fields can give us the anisotropy of the orbital magnetic moment m_{L} and allow us to separate the spin magnetic moment m_{S} and the magnetic dipole moment m_{T} from the effective spin moment $m_{\mathrm{S}}^{\mathrm{eff}}$. The relationships between each moment are given by

$$m_{\mathrm{S}}^{\mathrm{eff}}(\theta) = m_{\mathrm{S}} - 7m_{\mathrm{T}}(\theta), \tag{2.20}$$

$$m_{\mathrm{L}}(\theta) = m_{\mathrm{L}}^{\perp}\cos^2\theta + m_{\mathrm{L}}^{\parallel}\sin^2\theta, \tag{2.21}$$

$$m_{\mathrm{T}}(\theta) = m_{\mathrm{T}}^{\perp}\cos^2\theta + m_{\mathrm{T}}^{\parallel}\sin^2\theta, \tag{2.22}$$

$$m_{\mathrm{T}}^{\perp} + 2m_{\mathrm{T}}^{\parallel} = 0, \tag{2.23}$$

where $m_{\mathrm{X}}^{\perp}$ and $m_{\mathrm{X}}^{\parallel}$ are the out-of-plane and in-plane component of m_{X}. The above relationships are established on the assumption that the spin moment has the isotropic distribution. Actually, in 3d transition metals, where the exchange interaction dominantly contributes, compared with spin-orbit interactions and crystal fields, the value of m_{S} and m_{T} were independently evaluated by the angle dependence of XMCD measurements [70, 141]. Although the spin-orbit interaction in Pt is large, the theoretical first-principles investigation has shown the above relationships also are applicable to Pt [74].

In this study, the synchrotron radiation measurements at the Pt L-edge were carried out at SPring-8 BL39XU (Japan Synchrotron Radiation Research Institute (JASRI)). The external magnetic field ($\mu_0 H = \pm 2$ T or ± 7 T) was applied for saturating magnetization to out-of-plane ($\theta = 0°$) and in-plane direction ($\theta = 83°$) using a 7 T-superconducting magnet. θ is defined as Fig fig:MCD. Circularly polarized x-rays ($P_c > 95\%$) were generated by using silicone(111) double-crystal monochromator and a diamond x-ray phase retarder of 1.4-mm thickness. The beam spot size of the x-ray was 0.5×0.5 mm^2 ($\theta = 0°$) or 0.3×0.5 mm^2 ($\theta = 83°$), respectively. Each XAS spectrum was counted by x-ray fluorescence yield mode using a for-element silicone drift detector. The photon helicity is reversed at 0.5 Hz while the x-ray energy was scanned around Pt-L edges.

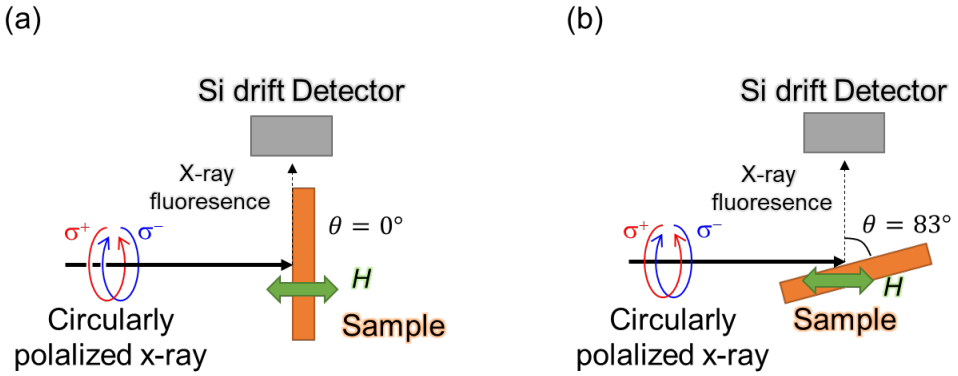

Figure 2.14: Setup scheme for XAS and XMCD measurement under (a) out-of-plane (b) in-plane magnetic field.

We evaluated the energy-dependent XAS spectrum by averaging spectra on the opposite circular-polarized x-ray irradiations, described as

$$\mathrm{XAS} = \bar{I}(E) = \frac{I^+(E) + I^-(E)}{2}, \tag{2.24}$$

where $I^+(E)(I^-(E))$ is the intensity whose incident photon momentum is parallel (antiparallel) to the magnetization direction of the samples. The XMCD spectra was calculated by

$$\mathrm{XMCD} = \Delta I(E) = I^+(E) - I^-(E). \tag{2.25}$$

In order to remove the background which is independent of magnetic field, we averaged

the spectra measured for the reversed magnetization. The averaged XMCD intensity was evaluated by

$$\mathrm{XMCD} = \Delta I(E) = \frac{\Delta I(E,H) - \Delta I(E,-H)}{2}. \tag{2.26}$$

As shown in Figs. 2.15(b) and (d), the intensity of XAS and XMCD spectra was normalized by taking into account the ratio of the XAS edge jump: $L_3 : L_2 = 2.22 : 1$ [142].

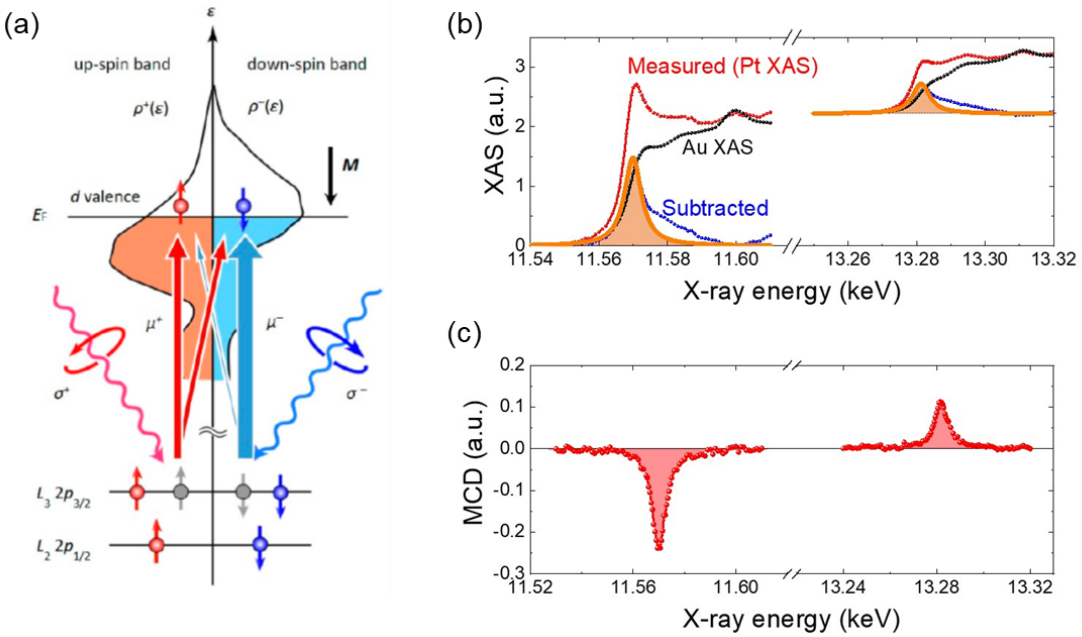

Figure 2.15: Schematics of XAS and XMCD measurement. (a) The excitation of Pt-2p electron into 5d state [6]. (b) XAS and (c) spectrum at L_3 and L_2 edges.

Chapter 3

Electric-field control of magnetic anisotropy in Pt/Oxide system

Electric-field (EF) control of magnetic anisotropy (MA) enables ultralow-power consumption magnetization switching in spintronic memory devices. Efforts to realize efficient EF manipulation of the magnetization direction have been extensively adopted with regard to $3d$-ferromagnet/MgO-based magnetic tunnel junctions. However, a new perspective of the material design is required to further improve the EF effect on MA. Here, we investigated the EF effect on MA in $5d$-Pt/oxide structures. Gate EF was applied to the surface of the Pt layer stacked on the ferromagnetic Co film using several types of oxide dielectric insulators. The efficiency of the EF-induced change in the perpendicular MA (PMA) energy β_S of the Pt/oxide system was comparable with β_S of $3d$ transition metal/MgO, but had increased by a factor of seven as the temperature decreased. In addition, β_S strongly depends on the thickness of the Pt electrode, whereas β_S for Co/oxide system showed little temperature dependence and no thickness dependence. Element-specific hard x-ray absorption spectroscopy (XAS) and x-ray magnetic circular dichroism (XMCD) measurements indicated that the proximity-induced orbital magnetic moment of Pt atoms related to the enhancement of β_S. We also examined the adjacent oxide dependence of β_S in the Pt/oxide system. β_S depended on the type of the interfacial oxide layer rather than the capacitance. The results of the XMCD spectroscopy and the measurement of the spin-orbit torque effective field anticipated that this strong oxide dependence was caused by changing the electronic state at the Pt/oxide interface.

3.1 Introduction

As aforementioned, the EF effect on magnetism for metal ferromagnets/oxide system is generally believed to originate from the modulation in 3*d* electronic structures. Recently, the EF effect has been also observed for structures with ultrathin paramagnetic 4*d* and 5*d* metals inserted at the 3*d*-ferromagnet/oxide interface [31,32,58,78,123,125,128–130,133]. One of the 4*d* transition metals, Pd, is typically a non-magnetic material. However, the Fermi energy E_F of bulk Pd is located near the local peak of the density of states, suggesting that the Stoner criterion is nearly satisfied [143]. In addition, in several 4*d* and 5*d* elements, such as Pd, Pt and Ir, that are close to a ferromagnetic layer, a magnetic moment is induced by *d* orbitals hybridization. This is known as the ferromagnetic proximity effect [128, 140, 144–146]. Fig. 3.1 shows the demonstration of the EF effect on magnetism for a magnetic capacitor structure with a Pd electrode and a thickness of 1-2 nm inserted at the Co/MgO interface. A large gate EF produced by an electric double layer (EDL) was applied through an MgO dielectric layer into the Pd layer (Fig. 3.1(a)). Fig. 3.1(b) shows the result of the direct magnetization measurement. The areal magnetic moment was changed by $V_G = \pm 2$ V application at low temperature, indicating that the proximity-induced magnetic moment in Pd can be modulated by the EF effect [31]. EDL gating manifested the EF-induced magnetism in the non-magnetic Pt/EDL system [147]. Furthermore, the EF effect on MA was observed in this system [123, 125, 129]. At 300 K, a linear EF-induced change was observed in PMA energy with β_S of 86 fJ/Vm. In contrast, at low temperature, a non-linear EF-induced change in MA was reported with a dramatic β_S over 1000 fJ/Vm (Fig. 3.1(c)). These results suggest that a non-magnetic metal layer inserted at a ferromagnets/oxide interface plays a key role in the enhancement of the EF effect on magnetism.

As shown in Fig. 3.2, the first-principles calculations have predicted that inserting 4*d* and 5*d* transition metal, with a huge spin-orbit coupling constant, would effectively contribute to an increase in the EF effect on MA [148]. In the last few years, the enhancement of β_S has been demonstrated experimentally by introducing Pt [78], W [130, 133], and Ir [128, 130] between Fe and MgO layers. In particular, a large β_S up to 320 fJ/Vm has been achieved in the solid-state magnetic tunnel junction (MTJ) with an Ir-doped Fe electrode. Theoretical calculations confirm the mechanism of the EF-induced MA in the FeIr/MgO system is because

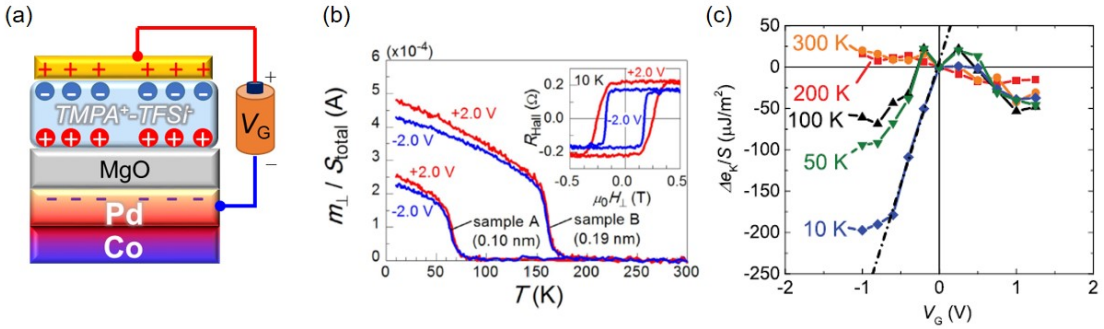

Figure 3.1: (a) The schematic of Co/Pd system with EDL gating. (b), (c) The demonstration of EF-effect on the magnetic moment in Pd layer and perpendicular MA energy in Co/Pd/MgO/EDL system [31, 125].

of the modulation of the majority spin in Ir-5d orbitals based on the conventional Bruno model ($\delta E_{\uparrow\uparrow}+\delta E_{\downarrow\downarrow}$ shown in Fig. 3.2(b)) [128]. In contrast, the contribution of the charge reordering mechanism ($\delta E_{\uparrow\downarrow}+\delta E_{\downarrow\uparrow}$) is very small; this is different from the Pt insertion case [78].

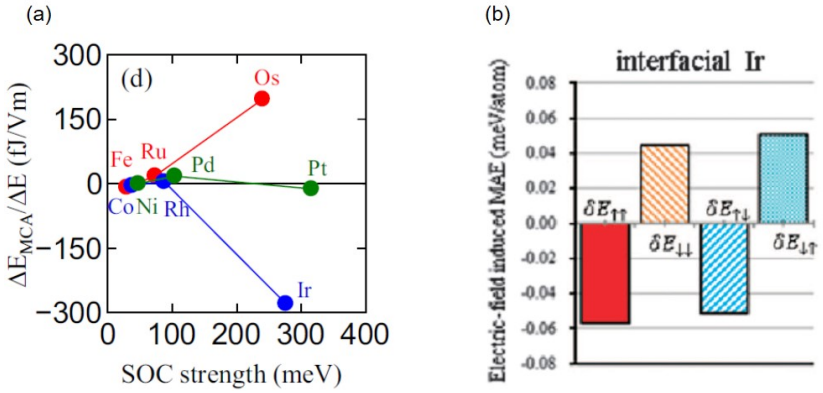

Figure 3.2: (a) First-principle calculation of β_S for Au/Fe/X/MgO structure with insertions of X elements, where X is 3d (Fe, Co, Ni), 4d (Ru. Rh, Pd), and 5d (Os, Ir, Pt) [148]. (b) First-principle calculation of EF-induced MA energy for the interfacial Ir atoms in Cu/FeIr/MgO structure [128].

The EF control of magnetism in the Pt insertion system has also been studied in the EDL capacitor comprised of a Co/Pt/MgO stack [58, 149]. However, previous reports have confirmed a very tiny EF-induced change in the magnetic moment and coercivity (PMA) compared to that in similar structures made of the Co/Pd/MgO/EDL system [31,123,125,129] and FePt/MgO system [78]. To elucidate this difference, we investigated the EF effect on MA in 5d transition metal Pt electrode stacked on ferromagnetic Co layer. We applied

EF through four types of oxide dielectric layers: MgO, HfO_2, Al_2O_3, and SiO_2. We also examined the temperature dependence of the efficiency of the EF-induced change in MA on ferromagnetic-induced Pt using the solid-state capacitor.

3.2 Fabrication of Pt/oxide structure

The layered structure of the measurement sample is shown in Fig. 3.3. The bottom electrode stack, consisting Ta/Pd/Co/Pt, was deposited on semi-insulating GaAs(001) or thermally oxidized Si substrate using rf magnetron sputtering at room temperature under inert Xe gas with a pressure of 0.2 Pa. Following removal of the samples from the sputtering chamber to the air, the samples were processed into a 30-μm-wide or 120-μm-wide Hall bar mesa pattern with 500-μm-square electrode pads. This was done for source-drain contacts and probing Hall and 4-wire voltages using photolithography and Ar ion milling (detailed conditions specified in Sec. 2.1.3). The surface of the samples was then covered with a dielectric oxide layer. We prepared six types of dielectric layers shown in Fig. 3.3. MgO and SiO_2 layers were deposited by rf sputtering and HfO_2 and Al_2O_3 layers were deposited in an atomic layer deposition (ALD) chamber at 150°C under ~0.3 Torr N_2 condition. Each time of exposing Pt surface to the air and 150°C-annealing time of all samples was aligned for 10 min and 2 h, respectively. Finally, Cr(2)/Au(10) or Al(35) for the top counter electrode was evaporated using the lift-off process. Note that, in this chapter, numbers in the parentheses show nominal thickness in nanometer orders and the layer thickness of material-X is described as t_X (e.g., the thickness of Pt t_{Pt}).

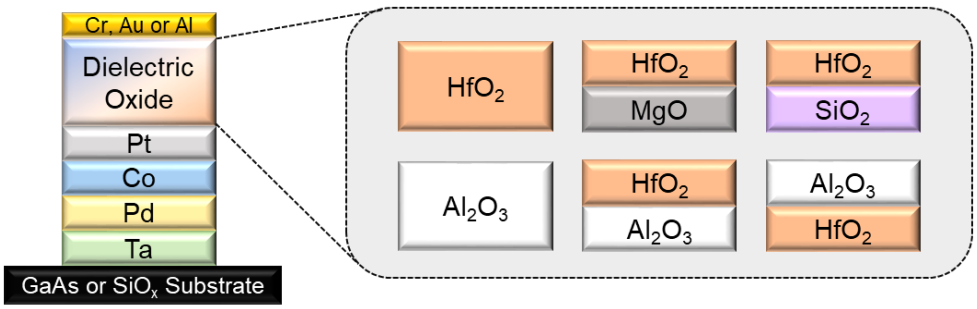

Figure 3.3: The schematics of the layered structure studied in this chapter.

The x-ray diffraction (XRD) measurement performed using the conventional θ-2θ method (Fig. 3.4) confirmed that the fcc(111)-oriented Pt layer and the fcc(111) or hcp(0002)-oriented Co layer were separately stacked. Further, all the dielectric oxide layers were presumed to have an amorphous or polycrystalline texture [27]. To evaluate the oxidation of the Co and Pt layers, x-ray photoelectron spectroscopy (XPS) measurements were conducted. Figs. 3.5(a) and (b) show the normalized XPS spectra of Co-2p and Pt-4f states, respectively. The experimental XPS spectra (orange lines) shown in the figures are the average results of the data obtained by changing the angle of the incident x-ray (21.875-78.125°) from the normal to the plane. The blue lines show the total intensity synthesized by Gaussian fitting analysis in terms of contributions from the Co metal (Pt metal) and the Co oxide (Pt oxide) This confirms that the present Co and Pt layers existed in purely metallic states. In addition, Fig. 3.5(c) suggested that the difference in the oxide layer close to the Pt surface did not affect the chemical state of the top Pt layer.

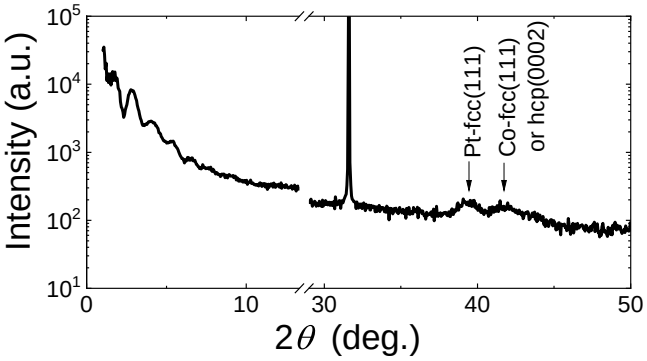

Figure 3.4: XRD profile for Ta(3.3)/Pd(3.1)/Co(2.4)/Pt(1.0)/HfO_2(50) deposited on GaAs substrate.

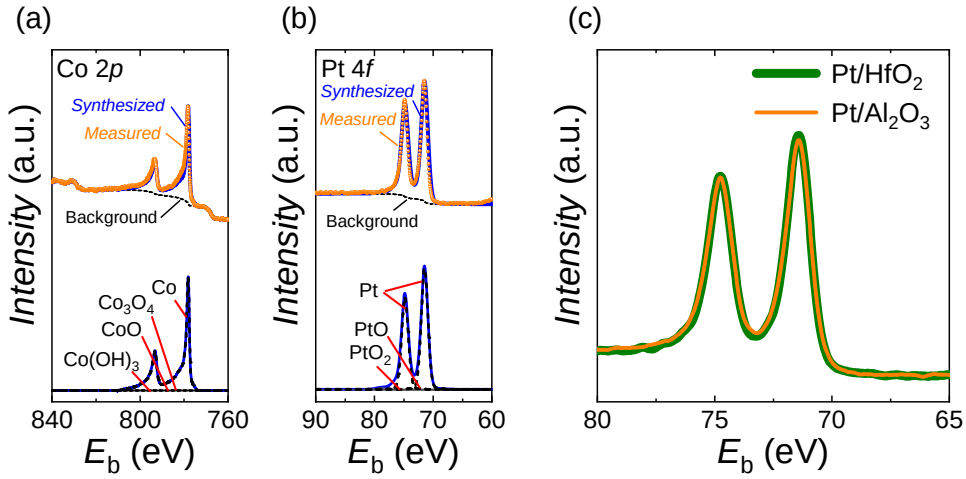

Figure 3.5: XPS spectra and Gaussian fitting analysis for the (a) Co-2p and (b) Pt-4f in the Co(2.4)/Pt(1.0)/HfO_2(2) sample. (c) Pt-4f XPS spectra for Co(2.4)/Pt(1.0)/HfO_2(2) and Co(2.4)/Pt(1.0)/Al_2O_3(2) samples

3.3 Electric-field control of magnetic anisotropy in Pt/HfO_2 structure

Perpendicular magnetic anisotropy

Prior to the gating experiments, we investigated the MA for the Ta/Pd/Co/Pt/HfO_2 structures stacked on the GaAs substrate (i.e., the Co(t_{Co})/Pt(t_{Pt})/HfO_2(t_{HfO_2}) sample) The layer structure is shown in Fig. 3.6(a). Figs. 3.6(b) and (c) represent the results of the anomalous Hall measurement at 300 K for Co(0.4)/Pt(0.7)/HfO_2(50) sample. A square hysteresis was shown by sweeping perpendicular magnetic field $\mu_0 H_\perp$, indicating the strong interfacial PMA caused at Pd/Co and Co/Pt interface [25, 65]. Fig. 3.6(d) shows the temperature T dependence of the PMA energy per unit area tK_u, calculated by the hard axis magnetization curve (Fig. 3.6(c)) and the direct magnetization measurement (Sec. 2.5). It was found that tK_u linearly increased with the decrease in T.

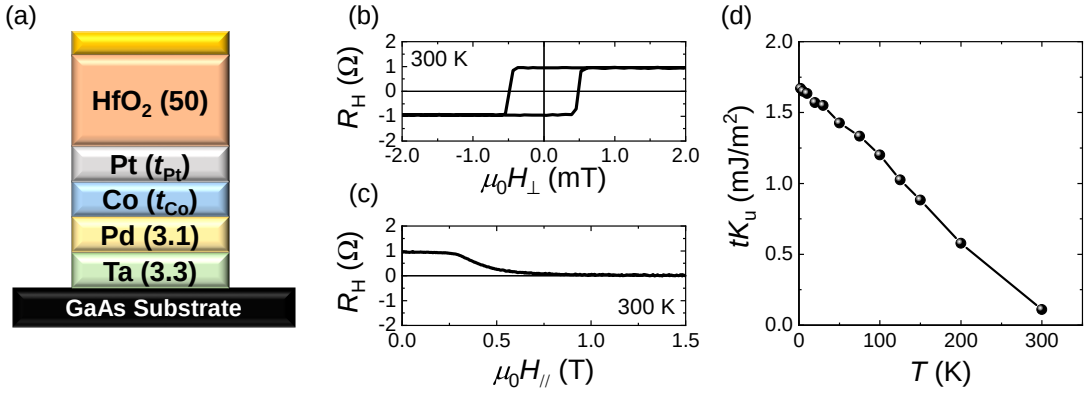

Figure 3.6: (a) The layer structure for Co/Pt/HfO_2 sample, where each layer thickness was shown in the parentheses. (b) Out-of-plane magnetic field $\mu_0 H_\perp$ and (c) In-plane magnetic field $\mu_0 H_\parallel$ dependence of the Hall resistance R_{Hall} for Co(0.4)/Pt(0.7)/HfO_2(50) sample. (d) T dependence of the PMA energy per unit area tK_u for Co(0.4)/Pt(0.7)/HfO_2(50) sample.

Temperature and Pt thickness dependences of electric-field effect on perpendicular magnetic anisotropy

From here, we focus on the EF effect on the MA in the Co/Pt/HfO_2 sample. Figs. 3.7 show the out-of-plane (Figs. 3.7(a) and (c)) and in-plane (Figs. 3.7(b) and (d)) magnetization curves at 300 K and 10 K under the gate voltage V_G = ±15 V (E_G = ±3 MV/cm) for the perpendicularly-magnetized Co(0.4)/Pt(0.7)/HfO_2(50) sample. The vertical axes were normalized by the saturated R_{Hall} value. Note that the positive (negative) V_G and E_G induces the accumulation (depletion) of electrons at the Pt/oxide interface. The clear EF-induced increase (decrease) in both coercivity H_c and the saturation field was obtained by applying positive (negative) E_G. The EF-induced change in tK_u ($\Delta(tK_u)$) was shown in Fig. 3.7(e). The positive (negative) E_G application resulted in the enhancement (reduction) of PMA, the opposite response to systems with 3*d*-transition metals/MgO [23, 117], FePt/MgO [78], and FeIr/MgO interfaces [128]. In addition, Fig. 3.8 shows that there was no hysteretic EF change in the H_c and tK_u and a very small sheet resistance R_{sheet} change (~0.001% at 1 V) was obtained by the repetitive Hall measurement at 10 K under changing V_G value. This suggests that the voltage-driven chemical effects were not the origin of the present EF effect.

Red plots in Fig. 3.9(a) show the T dependence of the EF control efficiency of PMA energy (β_S) for Co(0.4)/Pt(0.7)/HfO_2(50) sample. There was rapid increase in β_S as T decreased by ~590%; from 39 ± 3 fJ/Vm (at 300 K) to 268 ± 8 fJ/Vm (at 10 K). In contrast, β_S for the perpendicularly-magnetized Co(0.4)/MgO(2.0)HfO_2(50) sample increased by approximately 100%; from 24 ± 2 fJ/Vm (at 300 K) to 47 ± 3 fJ/Vm (at 10 K) (purple plots in Fig. 3.9(a)). Here, the error bars in Fig. 3.9(a) indicated the linear fitting errors. The observed temperature dependence of β_S in the Co/MgO system has the same tendency as the CoFeB/MgO system [150]. On this basis, it can be deduced that the present dramatic increase in β_S was attribute to the 5*d*-Pt layer insertion. The dramatic increase in β_S layer with the decrease in T was also observed in the in-plane-magnetized Co/Pt/HfO_2 films, where t_{Co} = 2.4 nm (see in Fig. 3.9(b)). In Fig. 3.9(b) we found that the magnitude of β_S strongly depended on the top Pt thickness. The Pt thickness dependence of β_S for Co(2.4)/Pt(t_{Pt})/HfO_2 samples is shown in Fig. 3.10(a). The decrease in β_S with the increase in t_{Pt} was obtained at all measurement

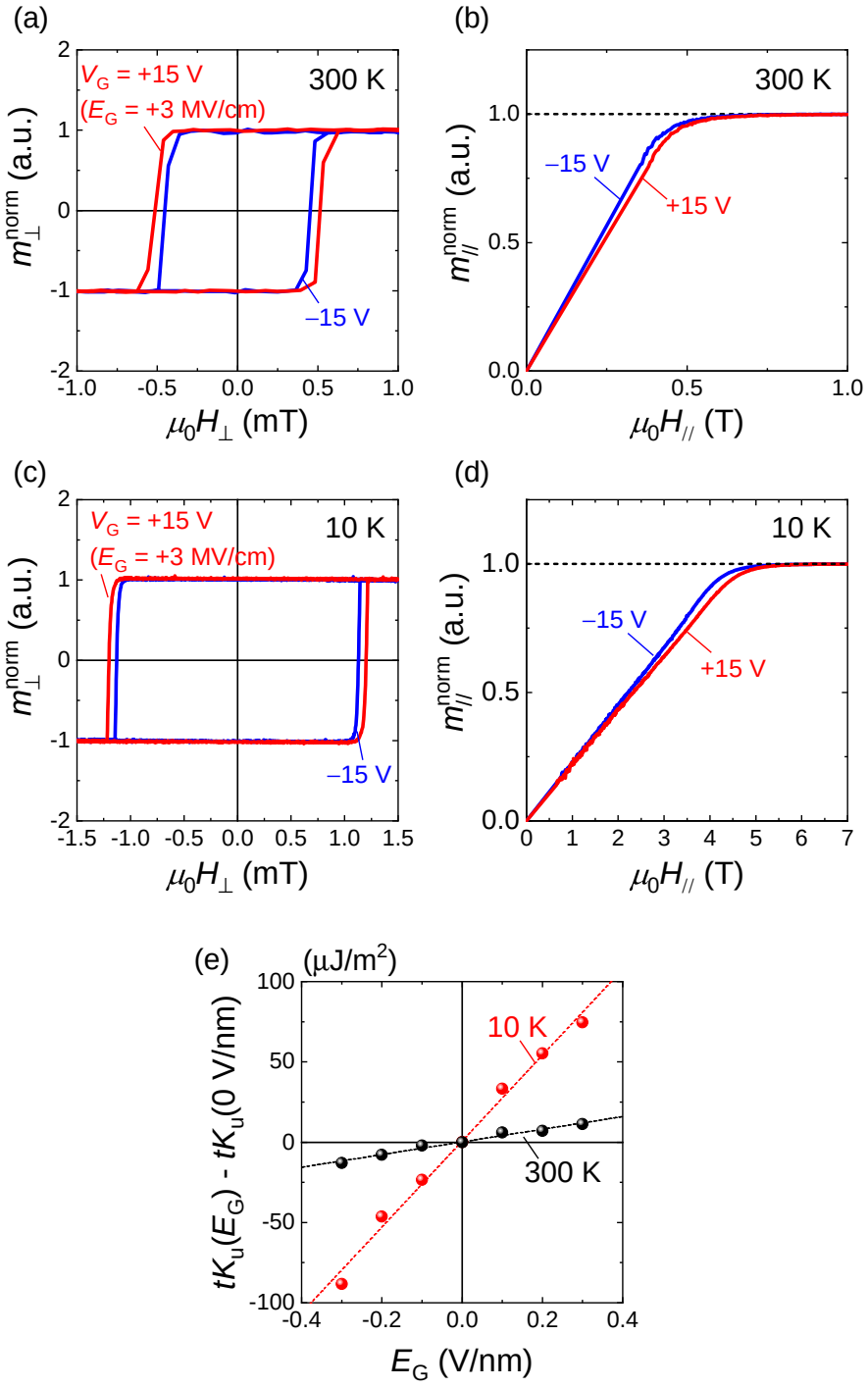

Figure 3.7: (a) [(c)] The normalized out-of-plane and (b) [(d)] in-plane magnetization curves at 300 K [10 K] under the gate voltages $V_G = \pm 15$ V for Co(0.4)/Pt(0.7)/HfO$_2$(50) sample. (e) E_G dependence of tK_u subtracted from $tK_u(0\text{V/nm})$ at 300 K and 10 K. Dashed line shows the linear fitting of the data.

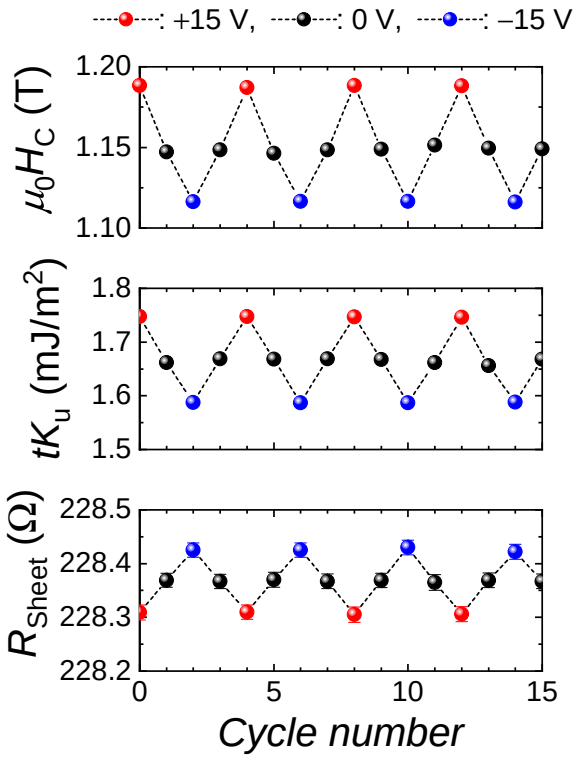

Figure 3.8: H_c, tK_u, and R_{sheet} as a function of the cycle number of each Hall measurement.

temperatures. Conversely, in the Co/MgO system, the β_S value was almost independent of electrode thickness t_{Co}.

In previous experimental studies for a Co/Pt bilayer, the proximity-induced magnetic moments of Pt was found to decrease with the distance from Pt/Co interface as an exponential function with a characteristic proximity length of approximately 2 nm by XMCD measurement at room temperature (see in Fig. 3.11(a)) [140]. In addition, as shown in Fig. 3.11(b) and (c), it was confirmed that the proximity length of ~2 nm had remained the same for the most part, even at 10 K [26]. These phenomena are similar to the observed t_{Pt} dependence of β_S. Due to the electrostatic screening effect, the applied EF only interacts with the Pt surface. Therefore, we have deduced that the amount of the proximity-induced Pt magnetic moment at Pt/oxide interface is crucial for the enhancement of β_S. In contrast, a uniform distribution of the magnetic moment is obviously characterized in the 3*d* ferromagnetic metal layer, which is consistent with virtually no t_{Co} dependence of β_S. The impact of the interfacial Pt magnetic moment on the peculiar T dependence of β_S is discussed later.

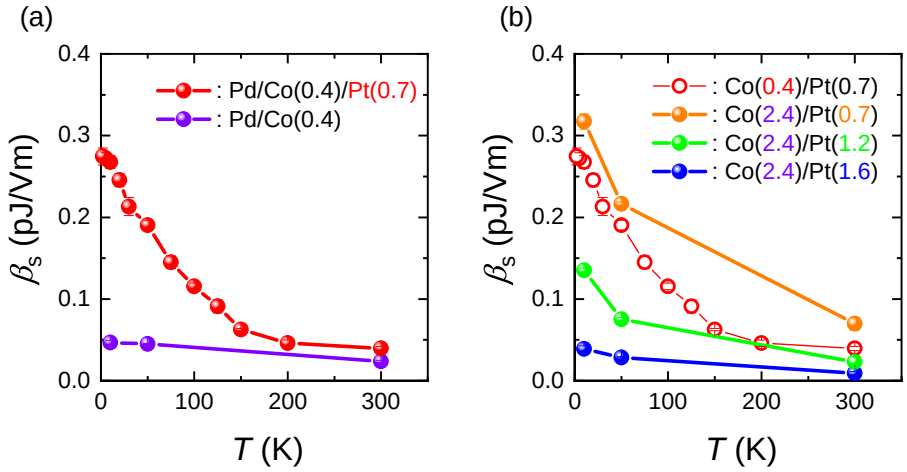

Figure 3.9: (a) T dependence of β_S for in-plane-magnetized Co(0.4)/Pt(0.7)/HfO$_2$(50) sample (red) and Co(0.4)/MgO(2.0)HfO$_2$(50) sample (purple). (b) T dependence of β_S for Co(2.4)/Pt(0.7)/HfO$_2$(50) sample (orange), Co(2.4)/Pt(1.2)/HfO$_2$(50) sample (green), and Co(2.4)/Pt(1.6)/HfO$_2$(50) sample (blue). Red circles indicate β_S for Co(0.4)/Pt(0.7)/HfO$_2$(50) sample which is same data in Fig. 3.9(a).

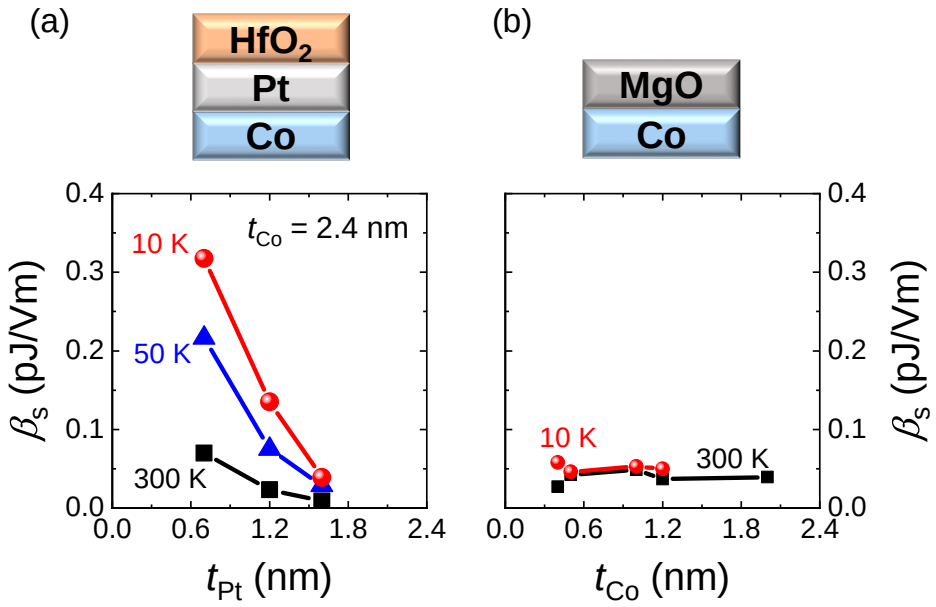

Figure 3.10: (a) t_{Pt} dependence of β_S in Co/Pt/HfO_2 system. (b) The t_{Co} dependence of β_S in Co/MgO system.

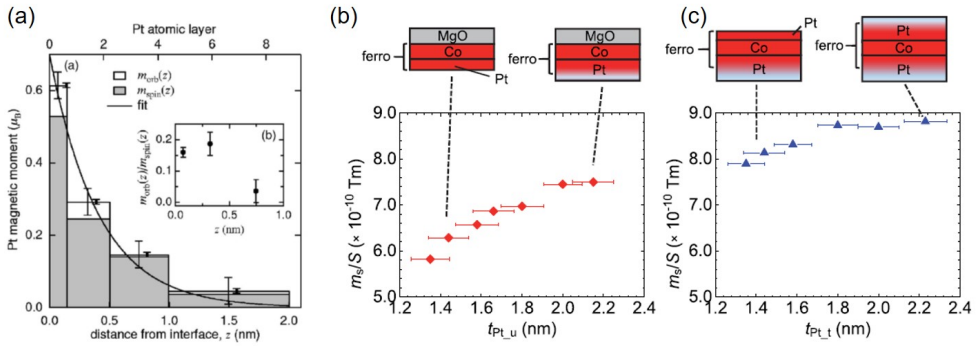

Figure 3.11: (a) The distribution of the Pt spin magnetic moment and orbital magnetic moment as a function of the distance from Co/Pt interface [140]. (b) Underlayer Pt and (c) top Pt thickness dependence of the areal saturation magnetic moment measured by SQUID magnetometer [26].

X-ray absorption and magnetic circular dichroism spectroscopy

To further investigate the Pt magnetic moment, we conducted XAS and XMCD measurements. In our synchrotron radiation measurements, the 50-nm-thick HfO_2 dielectric layer and the GaAs substrate were replaced by $HfO_2(t_{HfO_2})/Al_2O_3(t_{Al_2O_3})$ and a thermally oxidized Si substrate, respectively. This was in order to suppress the fluorescent x-rays of Hf-$L_{\beta 2}$ (9.346 keV), Ga-K_α (9.241 keV) , Ga-K_β (10.262 keV), As-K_α (10.52 keV), and As-K_β (11.722 keV) which may have a negative impact on the Pt-L_α (9.441 keV) and L_β (11.069 keV) yield. Figs. 3.12(a)-(d) show the results of the XMCD spectroscopy with the gate bias applications for the Co(3.0)/Pt(0.4)/HfO_2(5)/Al_2O_3(45) sample. The sample was cooled with out-of-plane magnetic fields of ±2T for saturation of the sample magnetization. To eliminate background drifts, the V_G values were applied in the order: +15 V (+15 V-1st) → −15 V (−15 V-1st) → −15 V (−15 V-2nd) → +15 V (+15 V-2nd). Figs. 3.12(a) and (b) show XAS and XMCD spectra measured at L_3 and L_2 edges of Pt at 32 K under $V_G = \pm 15$ V. The clear XAS and XMCD signals indicate the proximity-induced magnetic moment in Pt. The magnitude of observed normalized XMCD intensities was consistent with the previous reports using Co/Pt systems [58, 140]. Fig. 3.12(c) demonstrates the difference in the XAS spectra ΔXAS, defined as XAS(+15 V-1st [2nd]) − XAS(−15 V-1st [2nd]). The EF change in the XAS intensity corresponding to the unoccupied density of states of Pt near the E_F was only slightly observed in ΔXAS-1st data, but was absent in the ΔXAS-2nd data. In addition, no EF-induced XMCD change ΔXMCD was apparent in Fig. 3.12(d) although the β_S and $\Delta(tK_u)$ between +15 V and −15 V at 20 K for our sample were ~470 fJ/Vm and 160 μJ/m^2. This was larger than those in the FePt/MgO system where $\beta_S = 140$ fJ/Vm and the maximum $\Delta(tK_u)$ was 37 μJ/m^2 [78]. Then, we repeatedly measured the peak XMCD peak intensity at the x-ray energy of 11.579 keV under out-of-plane magnetic field of +2T as changing the V_G sign. However, no significant EF-induced change in XMCD was obtained in the histograms of the peak XMCD intensity at Pt-L_3 edge for $V_G = +15$ V and −15 V (Fig. 3.12). The lack of change in the XMCD intensity by applying EF observed in our sample may attributable to the fact the background drifts were not completely eliminated in this set-up, although the magnitude of EF-change in tK_u was the largest compared to the previous work [58, 78].

We then examined the high-field angle-dependent XMCD spectroscopy without applying

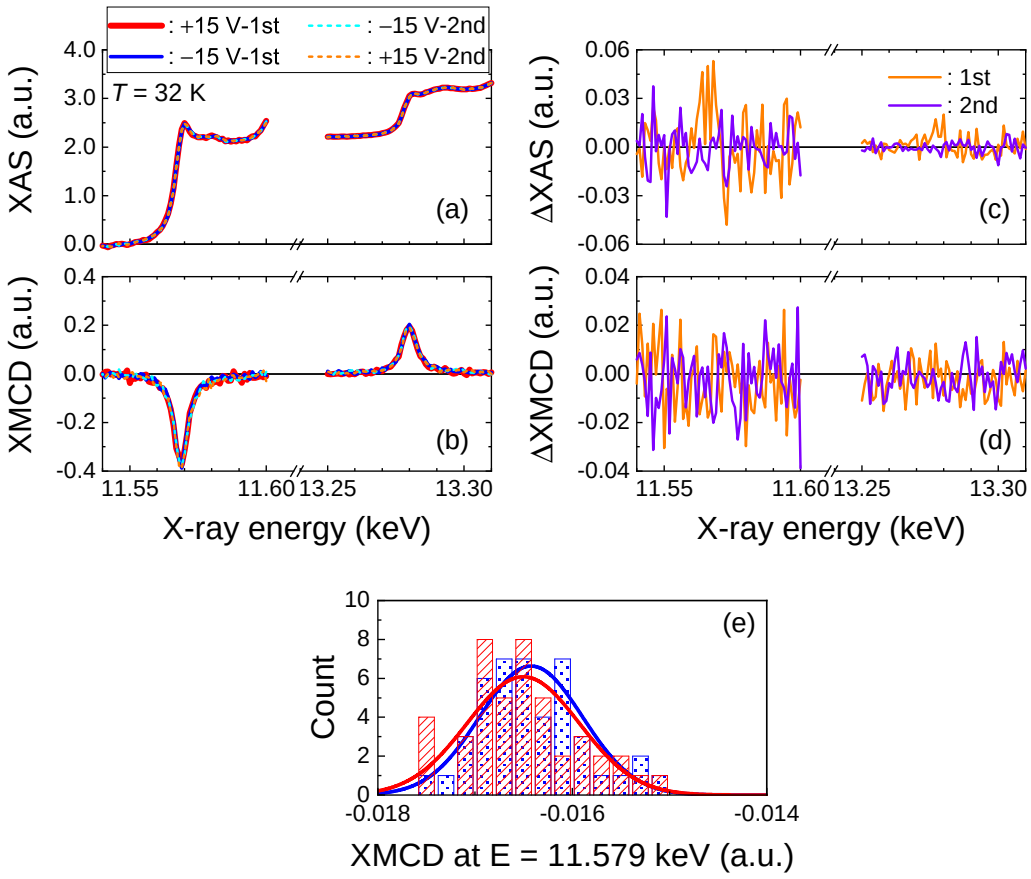

Figure 3.12: (a) XAS and (b) XMCD spectra at 32 K under V_G = ±15 V. (c), (d) The XAS and XMCD intensities for 1st (2nd) V_G = +15 V subtracted from those for 1st (2nd) V_G = −15 V. (e) The histograms of the XMCD intensity at the x-ray energy of 11.579 keV under V_G = ±15 V for the sample of Co(3.0)/Pt(0.4)/HfO_2(5)/Al_2O_3(45).

the external E_G. The spectra of Pt-L_3 and L_2 edges was recorded in external magnetic fields of ±7T parallel to the direction of x-ray propagation at angles of 0° (out-of-plane) and 83° (in-plane) with respect to the surface normal. The sample structure used in this experiment was Ta(1.9)/Pd(3.1)/Co(0.45)/Pt(0.7)/HfO_2(5)/Al_2O_3(45), where it had no counter electrode. We checked the magnetization saturation of this Co/Pt film in both configurations by the initial transport experiments in our lab. Fig. 3.13(a) and (b) show XAS and XMCD spectra at Pt-L_3 and L_2 edges measured at various temperatures from 300 K to 10 K under out-of-plane magnetic fields of ±7 T for the perpendicularly-magnetized Co(0.45)/Pt(0.7)/HfO_2(5)/Al_2O_3(45) sample. As T decreased, the peak of XMCD spectra at Pt-L_3 edge decreased quicker than that at Pt-L_2 edge. On the other hand, in XMCD spectra under in-plane ±7 T-magnetic fields

(Fig. 3.13(d)), such characteristic temperature dependence was not observed.

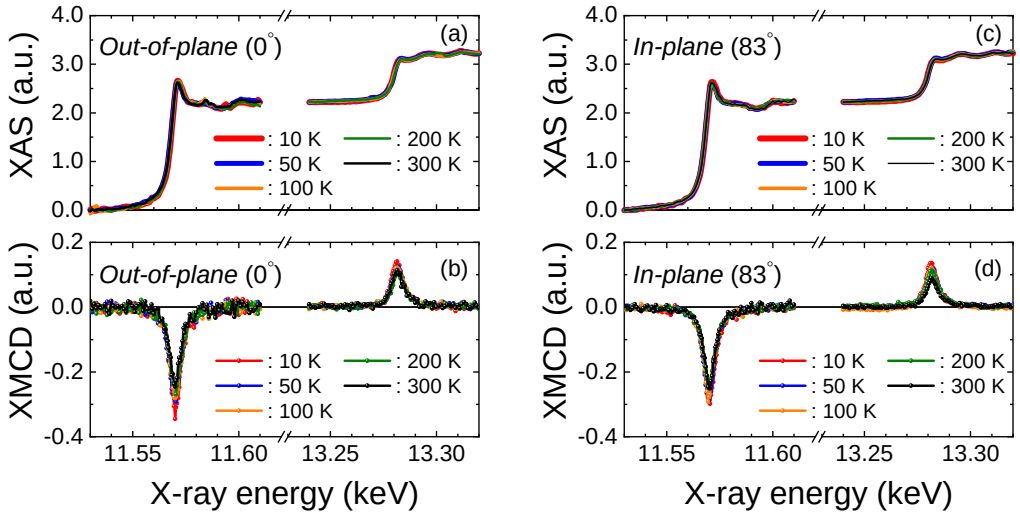

Figure 3.13: The out-of-plane [in-plane] configuration of (a) [(c)] XAS and (b) [(d)] XMCD spectra of Co(0.45)/Pt(0.7)/HfO$_2$(5)/Al$_2$O$_3$(45) sample in terms of T.

For quantitative analysis, we applied the sum rules [68,69] for the angle-dependent XMCD spectroscopy in Pt-L_3 and L_2 edges on the postulation that the spin density distribution of Pt atoms is isotropic [74]. Fig. 3.14(a) shows T dependence of m_S and $m_S + m_L^{\perp}$, where m_S and $m_L^{\perp}$ are the spin magnetic moment and the out-of-plane component of the orbital magnetic moment, respectively. Both m_S and $m_S + m_L^{\perp}$ increased as T decreased, which was supposed to result in the T dependence of the spontaneous magnetic moment of Pt in the Pd/Co(0.4)/Pt(0.7)/HfO$_2$ sample as shown in Fig. 3.14(b). The proximity-induced magnetic moment in the Pt layer was estimated by the direct magnetization measurement using a SQUID magnetometer [31,146] for the Co/Pt/oxide sample and the Co/oxide sample. The temperature dependence of the spontaneous magnetic moment for the Pd/Co(0.4)/Pt(0.7)/HfO$_2$ sample and the Pd/Co(0.4)/MgO sample is shown in Fig. 3.14(b). Here, the horizontal axis was normalized by the Curie temperature T_C and the vertical axis $m_{\perp}^{*}$ was normalized by the value of a magnetic moment at $T/T_C = 1$.

Fig. 3.15(a) shows T dependence of the out-of-plane $m_L^{\perp}$ and in-plane $m_L^{\parallel}$ components of the orbital magnetic moment. $m_L^{\perp}$ quickly increased as T decreased while the weak T dependence of $m_L^{\parallel}$ was shown, which was attributable to the different T dependence of

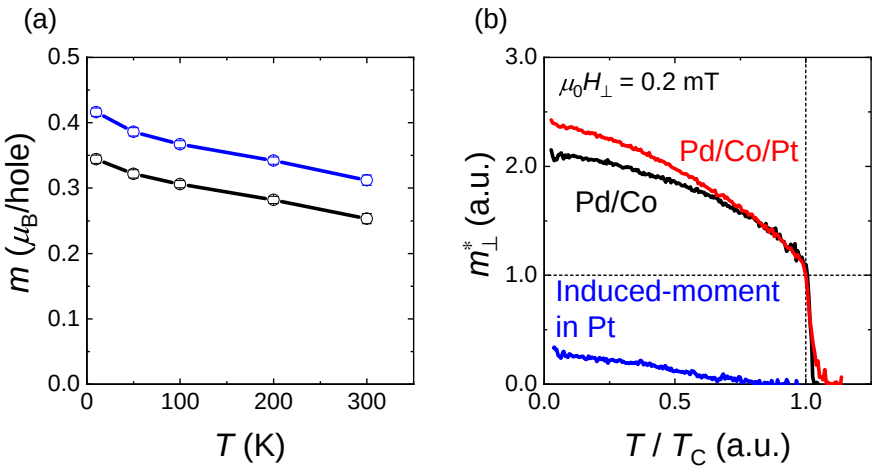

Figure 3.14: (a) T dependence of m_S and $m_S + m_L^{\perp}$. (b) The normalized temperature T/T_C dependence of the normalized magnetic moment $m_{\perp}^{*}$ for Pd/Co(0.4)/Pt(0.7)/HfO_2 sample and Pd/Co(0.4)/MgO sample.

XMCD between L_3 and L_2 edges of Pt (Figs. 3.13(b) and (d)). In addition, the increase in the difference between $m_L^{\perp}$ and $m_L^{\parallel}$: $\Delta m_L = m_L^{\perp} - m_L^{\parallel}$ was obtained at low temperature. In contrast, the magnetic dipole m_T had no significant T dependence (see in Fig. 3.13(c)). The appearance of $m_L^{\perp} - T$ and $\Delta m_L - T$ was similar to the T dependence of β_S. In Fig. 3.13(d), we obtained that the hole number of Pt in its $5d$ orbitals n_h^{Pt} decreased with the decrease in T, indicating that the band structure of Pt-$5d$ orbitals had altered by changing T. One possible explanation for this temperature dependence of the band structure is the internal lattice strain induced by the difference in thermal expansion coefficient between the deposited film and the substrate as proposed for the Co/Pd/MgO system [125, 129]. Free-standing films or bulk materials may show the isotropic reduction in atomic distance as temperature decreases. However, the existence of substrate prevents its shrinkage, and thus the magnitude of in-plane compressive strain in films will decrease with the temperature reduction. Moreover, first-principles calculations have predicted that strain-induced modification of electronic structures have a great impact on the PMA energy and the EF effect [151, 152]. The changes in lattice condition and resultant modulation of the internal strain in Pt may be a possible source of the observed temperature dependence β_S.

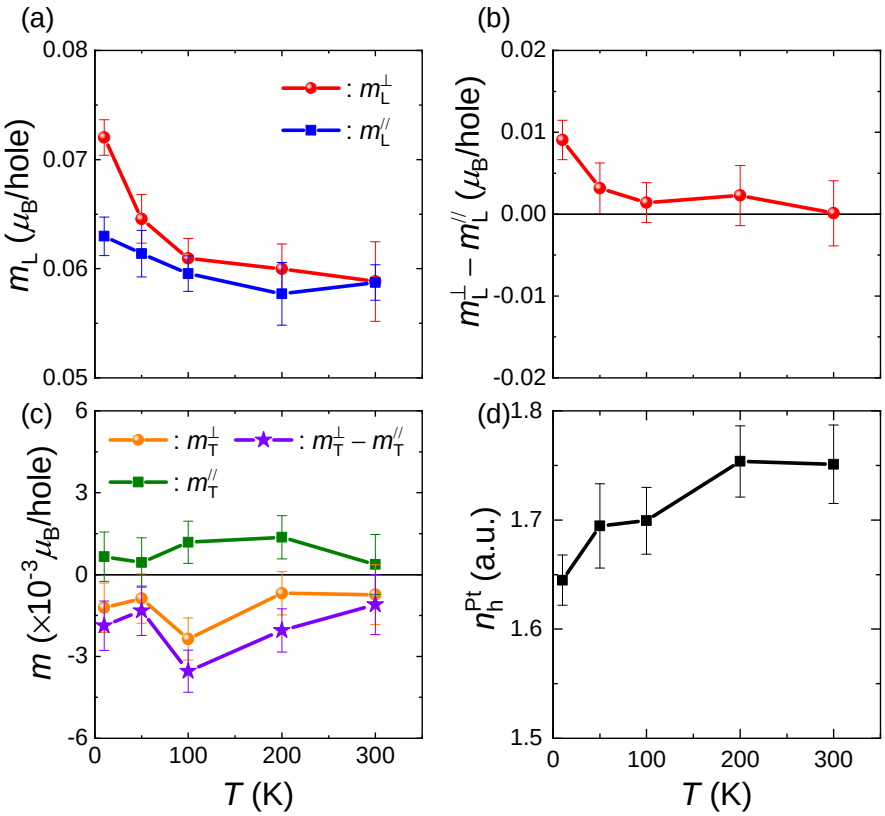

Figure 3.15: (a),(b) T dependence of out-of-plane $m_L^{\perp}$ and in-plane $m_L^{\parallel}$ components of the orbital magnetic moment and the difference $\Delta m_L = m_L^{\perp} - m_L^{\parallel}$. (c) T dependence of out-of-plane $m_T^{\perp}$ and in-plane $m_T^{\parallel}$ components of the magnetic dipole moment and the difference $\Delta m_T = m_T^{\perp} - m_T^{\parallel}$. (d)$T$ dependence of the hole number of Pt-5d orbitals n_h^{Pt}.

3.4 Interfacial oxide dependence of electric field control of magnetic anisotropy in proximity-induced ferromagnetic Pt

We have demonstrated a relatively large EF effect on MA in proximity-induced Pt/HfO_2 interface, compared to those in similar structures consisting of Co/Pt/MgO/EDL [58, 149] and even in the 3*d*-Co/MgO interface. In order to clarify this difference, we investigated the oxide dielectric layer dependence of the EF modulation of the MA effect. Firstly, we take a look at the results for the Pt/MgO structure. Figs. 3.16(a) and (b) show the out-of-plane and in-plane normalized magnetization curves measured at 10 K under the gate voltages of ±15 V for the Co(0.4)/Pt(0.7)/MgO(2)/HfO_2(50) sample. H_c and the saturation field at $V_G = +15$ V are larger than those at $V_G = -15$ V. However, although the measurement temperature was 10 K, a slight EF-induced modulation of H_c and PMA had occurred, the same tendency as EDL gating [58, 149]. β_S in the Pt/MgO interface (~8 fJ/Vm), which is the slope of the blue linear fitting line in Fig. 3.16(c), was about 34 times smaller than the Pt/HfO_2 interface (~270 fJ/Vm). However, the difference in the accumulated charge between the two capacitors was only 10%. Interestingly, this difference can be seen by only reversing the order of two dielectric layers. Fig. 3.16(d) shows the V_G dependence of $\Delta(tK_u)$ for the Co(0.4)/Pt(0.7)/HfO_2(25)/Al_2O_3(25) sample and the Co(0.4)/Pt(0.7)/Al_2O_3(25)/HfO_2(25) sample. The Pt/HfO_2/Al_2O_3 sample has about twice as large $\Delta(tK_u)$ as the Pt/Al_2O_3/HfO_2 sample. We note that there is almost no difference in the ratio of the V_G change in R_{sheet} (Fig. 3.16(e)), implying no difference in the charge accumulation at the Pt surface between the Pt/HfO_2/Al_2O_3 sample and the Pt/Al_2O_3/HfO_2 sample. This phenomena is against the scaling relations between the capacitance and the EF effect on PMA that was reported in the 3*d* transition alloy CoFeB/MgO system [153].

From here, we defined the new quantity $\beta' = \Delta(tK_u) \times t_{ins}^{total}/V_G \neq \beta_S$, where t_{ins}^{total} represents the total thickness of the insulating layers. Of course, β_S is the powerful tool for the evaluation of the EF effect on the PMA energy, but β_S contains information of the dielectric constant of the adjacent oxide. Thus, β_S is not suitable for the quantitative comparison of the EF-induced change in the MA among the samples with the different interfacial dielectric

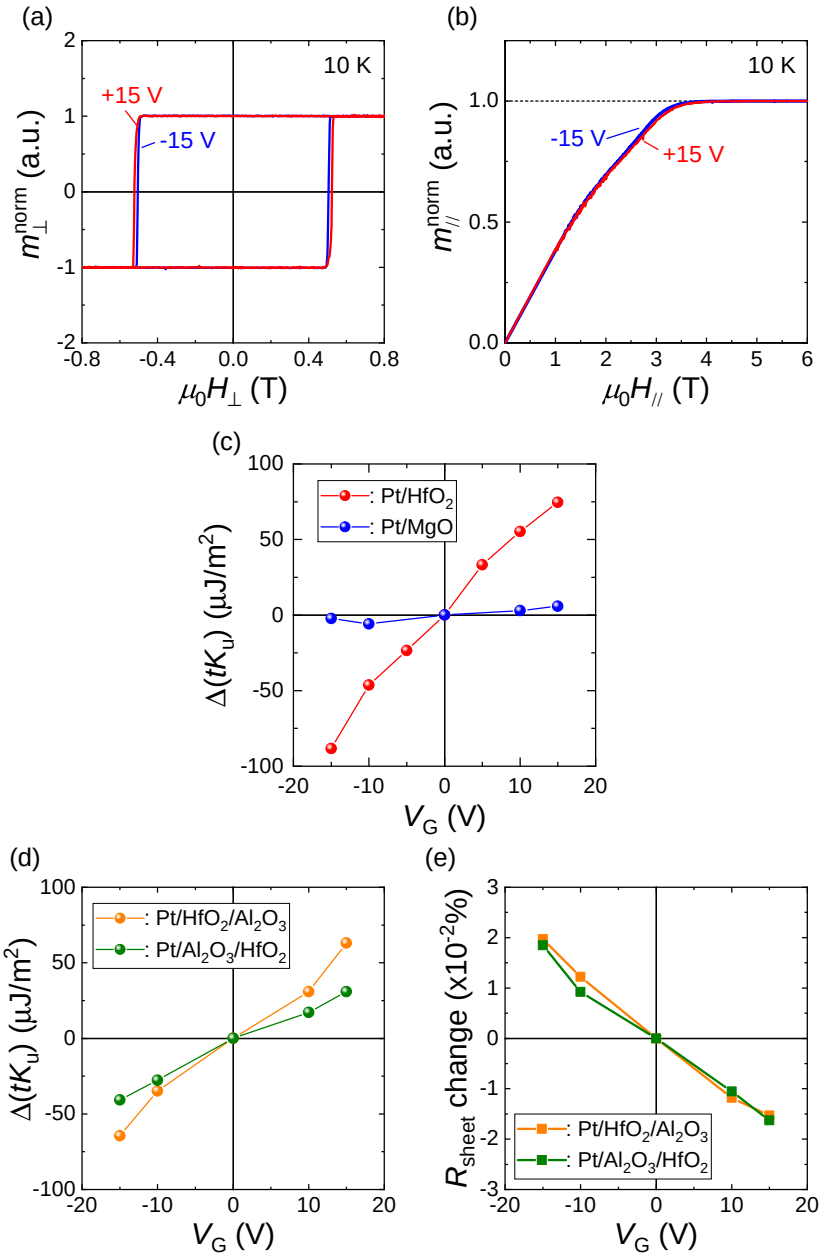

Figure 3.16: (a) The normalized out-of-plane and (b) in-plane magnetization curves under the gate voltages $V_G = \pm 15$ V for Co(0.4)/Pt(0.7)/MgO(2.0)/HfO_2(50) sample. (c) V_G dependence of $\Delta(tK_u)$ for Co(0.4)/Pt(0.7)/MgO(2.0)/HfO_2(50) sample and Co(0.4)/Pt(0.7)/HfO_2(50) sample. (d), (e) V_G dependence of $\Delta(tK_u)$ and the ratio of R_{sheet} change for Co(0.4)/Pt(0.7)/HfO_2(25)/Al_2O_3(25) sample and Co(0.4)/Pt(0.7)/Al_2O_3(25)/HfO_2(25) sample, respectively. Dashed lines show the linear fitting of the data. All graphs show the results at 10 K.

layer, as present case. Therefore, we first compared the EF effect by using β' which includes no information of the permittivity and simply manifests the PMA energy modulation characteristic as one field-effect device. Fig. 3.17 shows β', the areal capacitance C_S, m_s/S, tK_u at V_G = 0 V (tK_u(0 V)), and R_{sheet} for six Co/Pt/oxide samples. From left to right, the horizontal axis represents Pt/HfO_2(50), Pt/HfO_2(25)/Al_2O_3(25), Pt/SiO_2(2)/HfO_2(50), Pt/Al_2O_3(25)/HfO_2(25), Pt/Al_2O_3(50), and Pt/MgO(2)/HfO_2(50) structures. Here t_{Co} and t_{Pt} are 0.4 and 0.7 nm, respectively. β', m_s/S, tK_u(0 V), and R_{sheet} were measured at 10 K. The value of C_S and the permittivity of each dielectric material were quantified using an LCR meter (Keysight E4980A) at 300 K. Fig. 3.17 shed light on a number of aspects.

Materal	Permittivity
HfO_2	19.6
SiO_2	4.1
Al_2O_3	10.8
MgO	9.6

Table 3.1: Permittivity for each dielectric oxide.

Firstly, m_s/S and R_{sheet} show no definite dependence of the oxide layer. This implies that the effective ferromagnetic thickness and the crystal structure are almost the same for all samples. Secondly, tK_u(0 V) strongly depends on the interfacial oxide, suggesting that there is a strong interfacial PMA at the Pt/oxide. Lastly, there is no systematic relationship between β' and C_S. However, compared with the samples that have the same Pt/oxide interface, e.g. the Pt/HfO_2(50) sample and the Pt/HfO_2(25)/Al_2O_3(25) sample, β' and C_S appear to have one-to-one correspondence. This is attribute to the difference in C_S and the consequential difference in the magnitude of stored charge at Pt/oxide interface. For a further fundamental evaluation of the efficiency of the EF effect on the MA, we calculated the change in the PMA energy per unit accumulated charge by EF application: $\Delta(tK_u)/\Delta(C_S V_G)$. Fig. 3.18 shows $\Delta(tK_u)/\Delta(C_S V_G)$ for six Pt/oxide samples. These results indicate that the Pt/oxide interface plays a crucial role in the determination of the PMA energy and the EF-controlled MA.

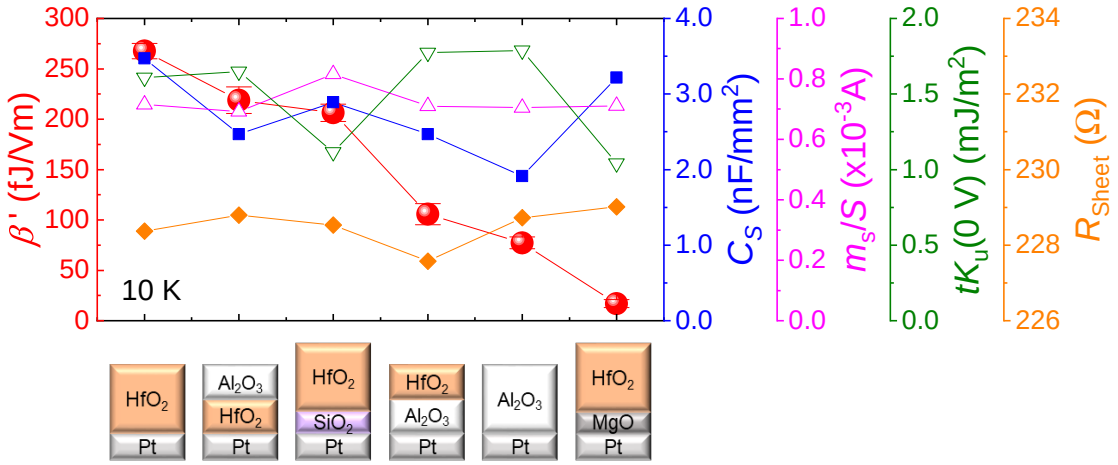

Figure 3.17: β', C_S, m_s/S, $tK_u(0\ \mathrm{V})$, and R_{sheet} for six Pt/oxide samples.

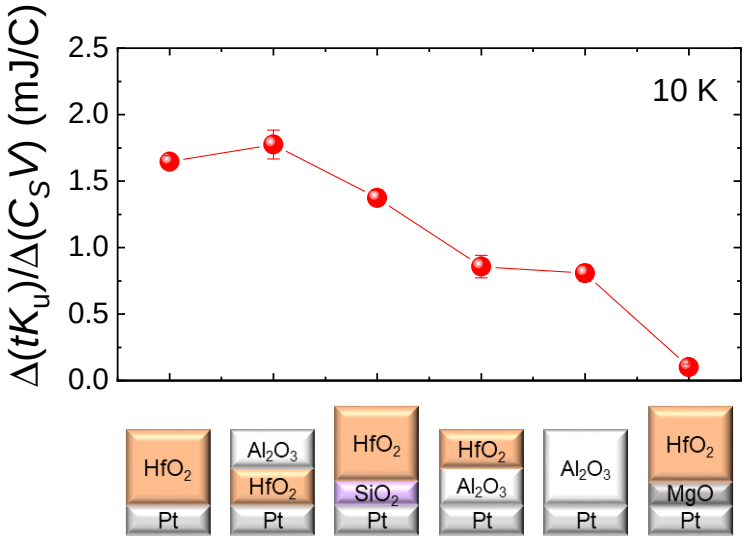

Figure 3.18: $\Delta(tK_u)$ per unit accumulated charge $\Delta(C_S V_G)$ for six Pt/oxide samples.

We focus on the investigation of oxide dependence of the Pt magnetic moment using synchrotron measurements. We conducted the XAS and the XMCD spectroscopy at 10 K under the external magnetic field of ±7 T with two (out-of-plane and in-plane) configurations for three samples: Co/Pt/HfO_2/Al_2O_3 (HfO sample), Co/Pt/Al_2O_3/HfO_2 (AlO sample), and Co/Pt/MgO/HfO_2/Al_2O_3 (MgO sample), in which t_{Co}, t_{Pt}, $t_{\mathrm{HfO_2}}$, $t_{\mathrm{Al_2O_3}}$, and t_{MgO} are 0.45, 0.7, 5, 45, and 1.5 nm, respectively. Note that the HfO sample was the same sample used

for the examination of temperature dependence of magnetic moments in Pt. Fig. 3.19(a) and (b) present the out-of-plane configuration of the XAS and XMCD spectra at the L_3 and L_2 edges of Pt for the HfO, AlO, and MgO samples. The peak intensity of the XMCD at the L_3 edge was comparable for three samples, whereas there was a distinct difference in the XMCD at L_2 edge was obtained. Fig. 3.20 shows the m_S, n_h^{Pt}, the out-of-plane and the in-plane components of m_L and m_T, and their differences for three Pt/oxide samples. m_S and $m_S + m_L^{\perp}$ (Fig. 3.20(a)) were almost the same value for the three samples; this is consistent with the result of the magnetization measurement. The Δm_L term of the MgO sample shows little contribution compared to the HfO and AlO samples even after accounting for the error bar, which explains the tendency of the PMA energy attributed to the Bruno mechanism [77] as shown in Fig. 3.17. In contrast, the magnitude of the Δm_T for the HfO sample corresponding to the PMA energy through the spin-flip process was about half the size as those for the AlO and MgO samples. Thus, we denote that the electronic structure of Pt-5*d* bands strongly depends on the interfacial oxide layer or a cation of the oxide.

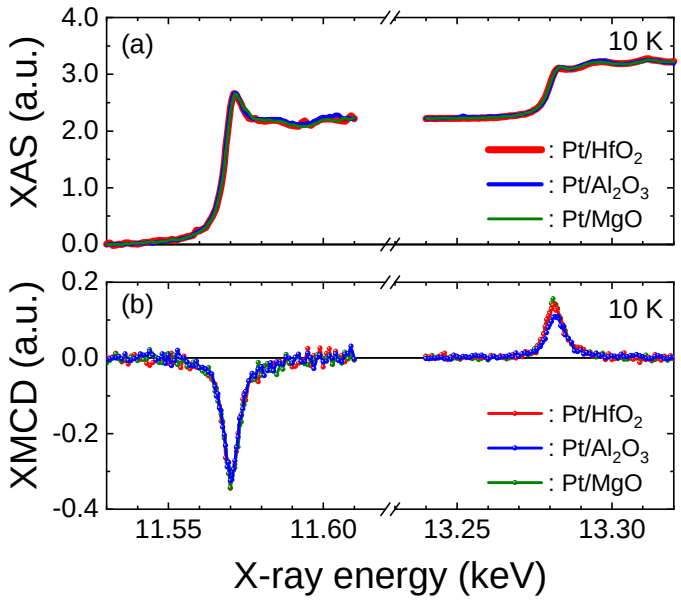

Figure 3.19: The out-of-plane configuration of (a) XAS and (b) XMCD spectra for the sample of Co/Pt/HfO_2(5)/Al_2O_3(45) (HfO sample; red), Co/Pt/Al_2O_3(45)/HfO_2(5) (AlO sample; blue), and Co/Pt/MgO(1.5)/HfO_2(5)/Al_2O_3(45) (MgO sample; green), where t_{Co} and t_{Pt} are 0.45 and 0.7 nm, respectively.

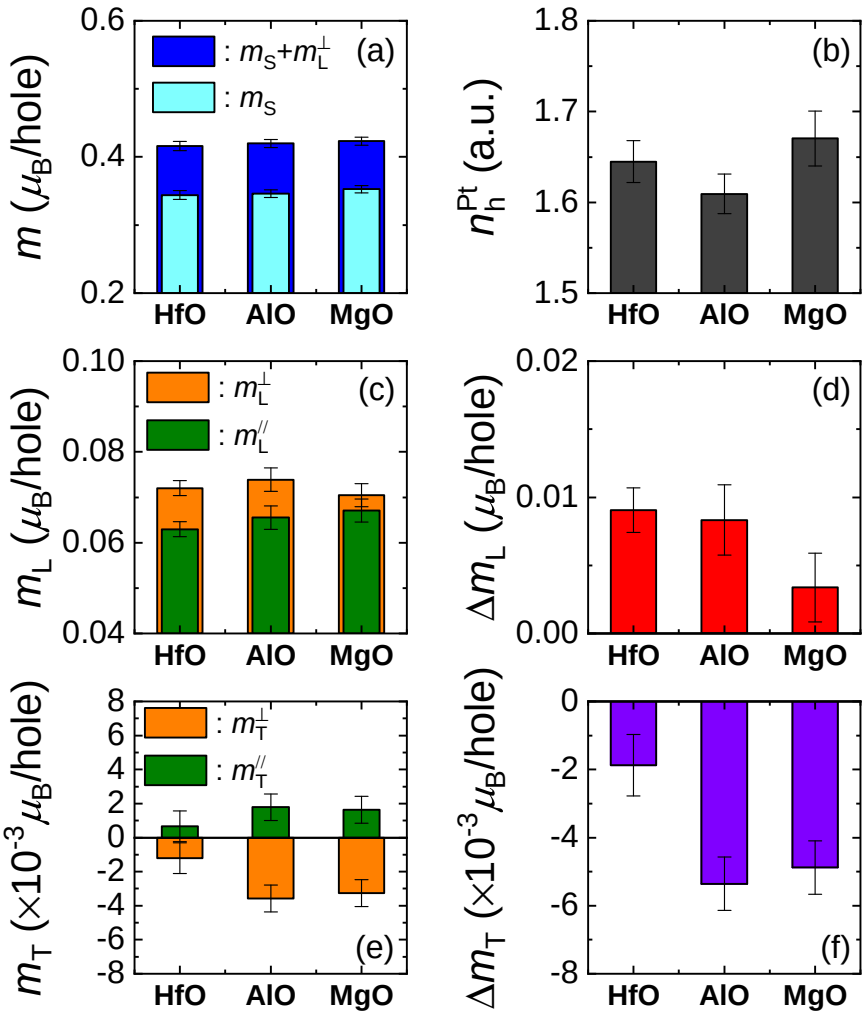

Figure 3.20: (a) m_S and $m_S + m_L^\perp$, (b) n_h^{Pt}, (c) $m_L^\perp$ and $m_L^\parallel$, (d) Δm_L, (e) $m_T^\perp$ and $m_T^\parallel$, and (f) Δm_T at 10 K for HfO sample, AlO sample, and MgO sample.

Then, we discuss the origin for the difference in Pt-5*d* electronic state arising from Pt/oxide interface. One possible explanation for this was the charge-transfer effect between a ferromagnetic atom and an oxygen atom [154]. The previous *ab* initio calculations for the Co-O bonding confirmed that oxygen absorption at the Co surface causes the degree of the exchange splitting and the spin and orbital magnetic moments via deprivation of charge from the topmost Co atom to an O atom. In an analogous scenario, the charge-transfer effect from a Pt atom to an O atom due to the high electro-negativity of the oxygen (Table. 3.2) can affect the band structure of the Pt-5*d* orbitals. It was anticipated that the strength of this electron depletion effect depends on the amount of oxygen at the interface. The oxygen concentration ratio of each oxide material is shown in Table 3.2. The number of transferred electrons from the Pt atom at Pt/HfO_2 and Pt/SiO_2 interfaces was supposed to be larger, compared to Pt/Al_2O_3 and Pt/MgO interfaces. Thus, the E_F shift to low energy may cause the magnetic properties sensitively because the peak of Pt-5*d* DOS is located just under the E_F. We deduce the difference in the efficiency of the EF effect on the PMA energy between Pt/HfO_2 and Pt/SiO_2 interfaces was attributable to the difference in the electro-negativity of the cation (Hf and Si). Assuming the Pt-O-cation bonding, the oxygen adsorption deprives many electrons from the topmost Pt atoms, but subsequently the neighboring cation atoms recover some electrons back to Pt to balance the charge. The electro-negativity of Hf atoms was larger than that of Si atoms, hence the E_F reduction for the Pt/HfO_2 system was suggested to be larger than that for Pt/SiO_2 system.

	Pt	O	Hf	Si	Al	Mg
Atomic number Z	78	8	72	14	13	12
Oxygen concentration ratio x (AO_x)	-	-	2	2	1.5	1
Electro-negativity	2.3	3.4	1.3	1.9	1.6	1.3
SOI coeffeicient ξ (mRy)	46.1	1.7	16.2	1.5	0.67	~0

Table 3.2: Oxygen concentration ratio x, Atomic number Z, and spin-orbit interaction (SOI) coeffeicient ξ of each element used in this study.

Another possibility is the interfacial Rashba spin-orbit interaction [155]. Theoretical studies have predicted that the Rashba magnetic field [156] can make an important contribution to the enhancement of the PMA energy. This is due to the interface potential gradient

at the surface or interface of large spin orbit materials. Considering the Rashba effect in the surface states, the single particle energy $\varepsilon_{k\sigma}$ is described as

$$\varepsilon_{k\sigma} = \frac{\hbar^2}{2m}(k - \sigma k_0)^2 - E_R, \tag{3.1}$$

where k, σ, m, and E_R are the momentum vector, the spin quantum number (± 1), the mass, and the effective Rashba electric field, respectively. The momentum shift k_0 and E_R are expressed as following;

$$k_0 = \frac{e\xi mE}{\hbar^2}, \tag{3.2}$$

$$E_R = \frac{1}{2}\left(\frac{e\xi}{\hbar}\right)^2 mE^2, \tag{3.3}$$

where e is elementary charge, ξ is the spin-orbit coupling coefficient, and E is the internal electric field taken to be perpendicular to the plane corresponding to the difference in the work function $\Delta\Phi_w$ and the applied E_{G}. In terms of the magnetic material, by transforming of eq. 3.1, the additional magnetic anisotropy generated by the Rashba effect K_R, follows

$$K_R = E_R\left[1 - \frac{2U}{Js}\right]\cos^2\theta \propto \xi^2 E^2, \tag{3.4}$$

$$U = \frac{\hbar^2}{2m}\left(\langle k_x^2\rangle_\uparrow - \langle k_x^2\rangle_\downarrow\right), \tag{3.5}$$

where θ is the angle between z axis and the magnetization vector, J is the exchange coupling constant, and s is the order parameter. Without voltage application, we regard E as $\Delta\Phi_w$. In our sample, the value $\Delta\Phi_w$ between Pt and the four oxides falls within the range of 0.65-0.75 eV [157, 158]. The values of ξ for the cations in each oxide material are shown in Table 3.2. ξ strongly depends on the atomic number and the difference among four oxides was larger, compared to $\Delta\Phi_w$. Therefore, ξ of cations in the oxide dielectric may dominantly determine the magnitude of E_R and K_R. On the other hand, $\Delta\Phi_w$ between $3d$-Co and the oxides was estimated to be almost zero, resulting in little contribution of the Rashba effective field in the $3d$ transition metals/oxide interface even if there are some differences in ξ.

In order to elucidate the contribution of the Rashba effect, the harmonic Hall resistances

attributed to spin-orbit torque (SOT) were measured by applying in-plane ac electrical current. The SOT phenomena and detailed procedure of the harmonic Hall measurement and analysis are introduced in Chap. 6. What should be underscored here is that SOT possesses two contributions; damping-like (DL) SOT and field-like (FL) SOT, and they are expected to be mainly dominated by different phenomena: DL-SOT for the spin Hall effect in the heavy metal layer [107] and FL-SOT for the Rashba spin-orbit coupling at the interface [106, 159].

Sample structures studied in this measurement were from a thermally oxidized Si substrate side Ta(1.6)/Co(3.2)/Pt(0.7)/HfO_2(5) and Ta(1.6)/Co(3.2)/Pt(0.7)/MgO(2)/HfO_2(5). Note that the magnetic easy axis of both samples was in-plane direction. To the extent possible elimination of the contribution of spin Hall effect-driven SOT, Pd underlayer was not adopted. For the harmonic Hall measurement, the sputtered and ALD-laminated films were processed into a 15-μm-wide Hall bar. During the Hall measurement, an ac current of 4 mA with a frequency of 13.14 Hz was applied along the source-drain channel of the sample, and Hall resistances were measured by rotating the external magnetic field H in the in-plane direction from 0° to 360° in increments of 5°. Fig. 3.21(a) and (b) show $[\mu_0(H + |H_k|)]^{-1}$ dependence of $R_{DL} + R_{ANE}$ and $(\mu_0 H)^{-1}$ dependence of R_{FL}, respectively. Here R_{DL}, R_{FL}, and R_{ANE} are the contribution of DL-SOT, FL-SOT, and the anomalous Nernst effect to the out-of-phase Hall resistance, respectively. The slope in Fig. 3.21(a) was almost same, whereas the slope on Fig. 3.21(b) for the Pt/HfO_2 sample definitely differed from the Pt/MgO sample. Note that the y-intercept in Fig. 3.21(a) represents the thermoelectric contribution to the second harmonic resistance (R_{ANE}). The SOT effective fields evaluated from the value of these slopes are shown in Fig. 3.22, in which H_{DL}, H_{FL}, and H_{Oe} represent DL-SOT and FL-SOT effective fields, and the Oersted field generated by applied current into non-magnetic layers, respectively. Fig. 3.22(a) illustrates that a similar DL-SOT effective field was observed, largely reflecting the same magnitude of the spin current generated by the spin Hall effect between two samples. This is because each layer thickness of non-magnetic metal (Pt and Ta) and R_{sheet} (=105 Ω) were the same for two samples. For exactly the same reason, the difference in H_{Oe} can be dismissed. Thus, the difference in the effective field shown in Fig. 3.22(b) is attributed to the difference in the FL-SOT effective field, suggesting that the Rashba-effective field and anisotropy exists at the Pt/oxide interface. Although the SOI of

oxide is smaller than that of Pt, our experimental results imply the magnitude of the Rashba effect can be modified by changing the oxide layer.

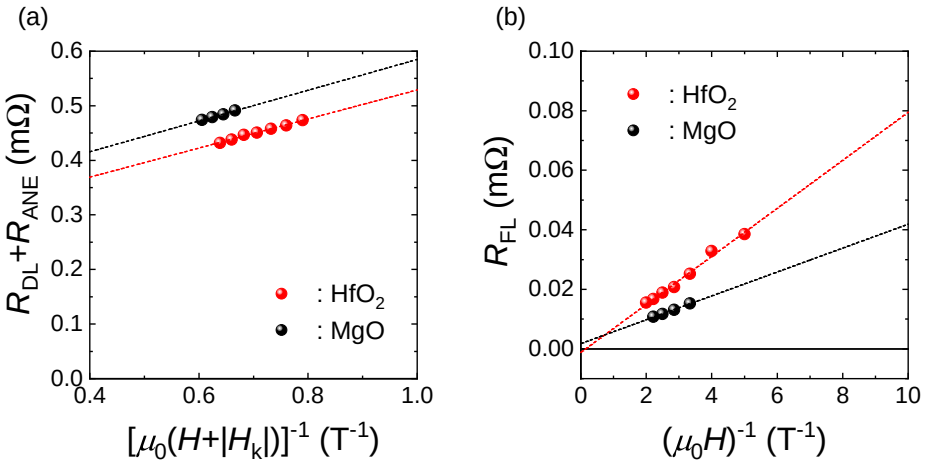

Figure 3.21: (a) $[\mu_0(H + |H_k|)]^{-1}$ dependence of $R_{DL} + R_{ANE}$. (b) $(\mu_0 H)^{-1}$ dependence of R_{FL}.

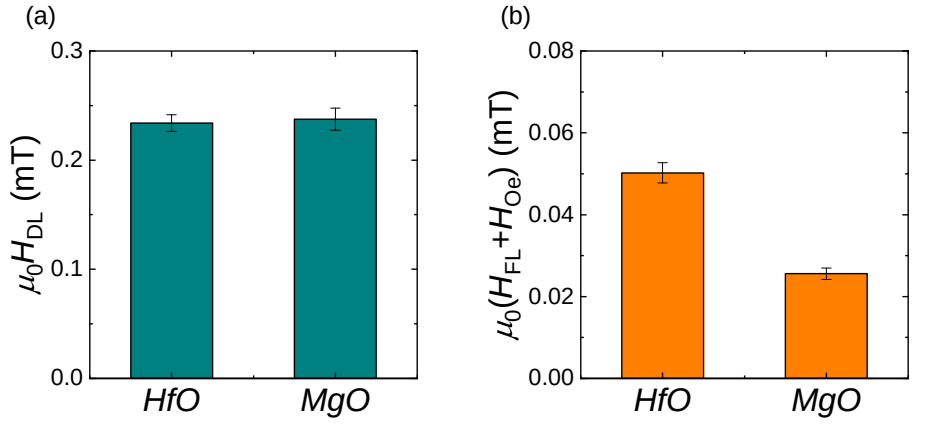

Figure 3.22: (a) H_{DL} and (b) $H_{FL} + H_{Oe}$ for Pt/HfO_2 and Pt/MgO samples.

3.5 Summary of this chapter

In this Chapter, we demonstrated new discoveries about the EF effect on MA through the investigation of the Co/Pt/oxide system where the magnetic moment was induced into Pt by the ferromagnetic-proximity effect. First, the efficiency of EF-induced modulation of the PMA energy at the Pt/oxide interface demonstrated a peculiar temperature dependence, quickly increasing at low temperature, compare to the 3d-Co/oxide interface. Second, the efficiency increased with the reduction of the top Pt thickness. The XAS and XMCD studies suggest that the amount of the induced orbital magnetic moment at the Pt/oxide interface relate to the efficiency enhancement. Finally, we found that neighboring oxide dielectric materials plays a crucial role in the PMA energy and its EF effect. The efficiency of the EF control of MA in the Pt/oxide system systematically changes in the order of the atomic number of the cation in oxide. In addition, we confirmed that the magnitude of the orbital moment and the magnetic dipole moment in the Pt atom differed depending on the adjacent oxide by the XMCD spectroscopy. We deduced that the oxides contribute the generation of some internal effective electric fields, resulting in the change in the electronic state in the Pt-5d orbitals. The SOT measurement also provided evidence supporting the fact that the effective field induced by the internal Rashba effect can be modified by changing the oxide. For further quantitative evaluation of the underlying physics of the EF-induced change in the Pt/oxide stacked structures, a elaborate theoretical investigation is required. The interface between a thin non-magnetic metal and a gate dielectric oxide with strong spin-orbit coupling would have unprecedented potential for not only the enhancement of the EF-control efficiency on the PMA energy but also other magnetic properties, including the spontaneous magnetic moment and the Curie temperature.

Chapter 4

Electric-field control of magnetic anisotropy and phase transition in Co/HfO_2 system

We investigated the electric-field (EF) effect on magnetism in the stacked structure of $Pt/Co/HfO_2$. The ultrathin Co film has the naturally oxidized surface. The EF was applied to the oxidized Co surface through two types of the gate dielectric layer consisting of HfO_2. The HfO_2 layers were formed by an atomic layer deposition (ALD) technique with the different fabrication temperature. The efficiency of the EF control of the magnetic anisotropy (MA) in the sample with the HfO_2 layer deposited at the appropriate temperature for the ALD process is much larger than that in an unoxidized Co electrode. The EF-change in the coercivity and the channel resistance reproducibly follows to the applied gate bias, and the resistance modulation is at most ~0.02%. On the other hand, in the sample with the HfO_2 layer deposited at a much lower temperature than the ALD temperature window, the magnetic properties drastically changed by the EF application. Not only the MA but the saturation magnetic moment is modulated by the EF and a much larger change in the channel resistance (>10%) is observed. The observed EF response of these properties is very slow, gradual and non-volatile, suggesting that a electrochemical redox reaction dominantly works as the mechanism of the EF effect, called as a magneto-ionic effect. The ac frequency response for the capacitive properties, and the x-ray photoelectron spectroscopy (XPS) measurement also

support the difference in the mechanism of the EF effect on magnetism.

4.1 Introduction

As previously mentioned, the mechanism of the EF control of magnetism has been basically considered to be the modification of the electronic states at the FM/insulator interface. However, recent studies shows the electrochemical effect, such as the oxidation/reduction (redox) reaction caused by a voltage-driven ion migration, a charge trap effect and/or other electromigrations, can also induce the change in magnetism [27, 52, 53, 160–169]. In the system using a liquid gating (e.g. an electrolyte and an ionic liquid) this magneto-ionic effect, which is similar to the a battery devices consisting of two electrochemical cells, has been reported. Some XPS studies proved that the magnetic properties were modulated by the change in the oxidation state induced by the application of the gate voltage V_G in FePt/$LiPF_6$ [161] and Co/MgO/$TMPA^+TFSI^-$ systems [27]. Recently, in the all-solid-state capacitor structure, the large change in magnetism induced by the electrochemical effect has been also observed. Figs. 4.1(a) and (b) show the results of XAS and XMCD spectra at Fe-L_3 and L_2 edges in FeCo/MgO (as-grown sample) and FeCo/MgO/SiO_2 (patterned sample). A clear broadening of Fe-L_3 and L_2 edge peak to the high energy and the considerable reduction of the MCD intensity confirm the oxidation of FeCo layer due to the patterning process. Figs. 4.1(c) and (d) are the results of the EF modification of XAS and XMCD spectra for the patterned sample. The enhancement of the amplitude of XAS and XMCD and vanishing the peak shoulder by applying the positive V_G suggest that the Fe oxidation state could be controlled by the voltage application. Moreover, in the Co/GdO_x system, the dramatic change in magnetism induced by the voltage-driven reversible oxygen ion migration has been reported [52, 53, 165]. Fig. 4.2 shows the evidence of the voltage-induced reversible oxygen migration using XAS and XMCD measurement [52] or a direct mapping of the oxide ion by polarized neutron reflectometry [165].

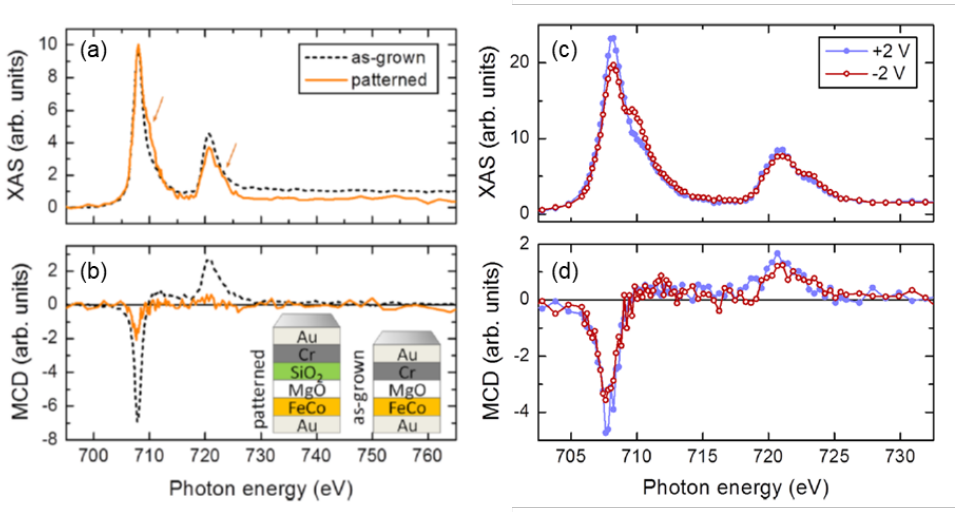

Figure 4.1: (a) XAS and (b) XMCD spectra at Fe-L_3 and L_2 edges for the as-grown and the patterned samples. (c) XAS and (d) XMCD spectra at Fe-L_3 and L_2 edges for the patterned sample under a voltage of ±2 V [164].

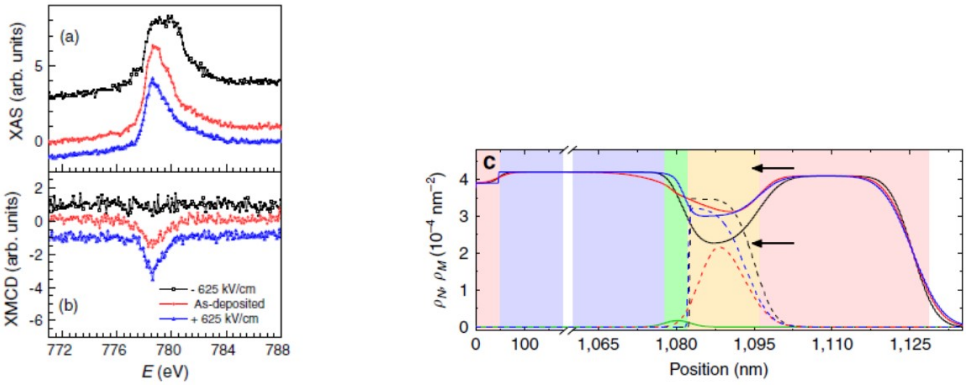

Figure 4.2: (Left figure) Normalized XAS and XMCD spectra at Co-L_3 edge after the gate voltage application. [52] (Right figure) Depth dependence of the real and magnetic component of nuclear scattering length density extracted from the polarized neutron reflectometry. Green and yellow region show GdO_x and Co, respectively [165].

The characteristics of the EF effect on magnetism driven by the electrochemical effect are quite different from those of purely electrostatic charge accumulation effect. First, we can achieve a drastic EF effect on magnetism more easily. For example, in the Co/GdO$_x$ system, the dramatically large efficiency of the EF control of MA ($>$ 10000 fJ/Vm) has been reported [52, 53]. Second, the operating speed is limited at most sub ms and strongly depends on the temperature and the external bias voltage, indicating that this effect is a thermal activation phenomena. Third, the repetitive endurance on the magnetization operation process is lower because the change in magnetism is accompanied by the change in the chemical and/or structural properties. However, recent studies have reported over 2000-cycles-magnetization switching by the voltage-induced H^+ pumping [169]. Fig. 4.3 shows the results of magneto-ionic switching on the magnetic easy axis by the proton accumulation/depletion at the Co/GdO$_x$ interface. Fig. 4.3 also shows no degradation in the magnetism after 2000-cycles H^+ pump treatment.

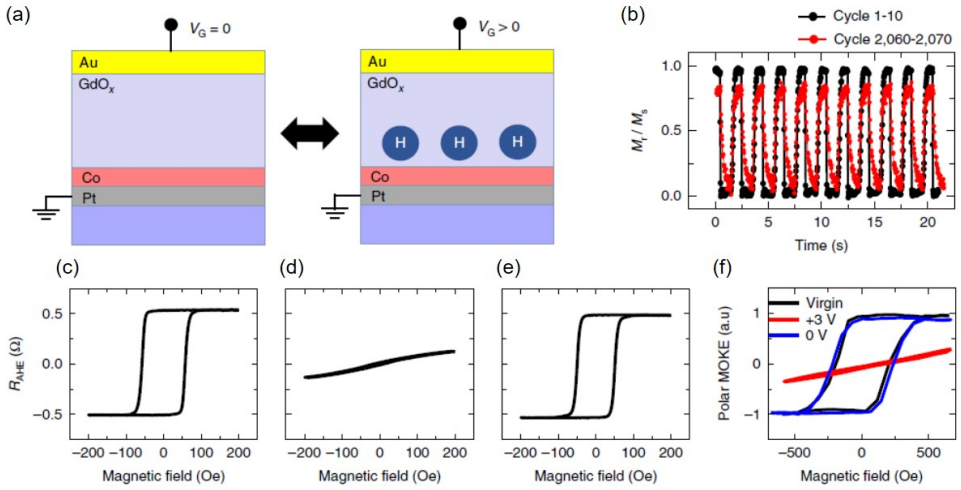

Figure 4.3: The results of magneto-ionic switching on magnetism by the voltage-induced hydrogen pumping in Co/GdO$_x$ system [169].

For both pursuing the underlying physics of the EF effect on magnetism and expanding the possibility of the application of the field-effect spin devices, we clarify these two effects; the electrostatic charge accumulation and the electrochemical reaction, and make choice as necessary.

4.2 Fabrication of Co/HfO_2 structure

The schematic illustrations of the measurement samples and device structure are shown in Fig. 4.4. The stack composed of Ta(3.3)/Pt(3.0)/Co(1.0) was deposited on an intrinsic Si(001) substrate by rf sputtering using a Xe process gas at room temperature (numbers in the parentheses show nominal thickness in nanometer orders). The same stack with a MgO(2.0) capping layer was also prepared as a reference sample. After the deposition, the samples were exposed to the air for ~10 min. The surface of the sample without the MgO cap was suggested to be naturally oxidized (Co/CoO_x sample). Subsequently, the surface of the sample was covered with a 5-nm-thick HfO_2 layer by ALD method in order to prevent further oxidation. The ALD deposition temperature of the HfO_2 was 150°C and 60°C. Note that 150°C is within the ALD window and 60°C is far below the ALD window [170]. For the electrical transport measurement, the samples were patterned into a 30-μm-wide Hall bar structure with the electrode pads by photolithography and Ar ion milling. After that, the whole surface of the samples was covered with a 40 (or 45)-nm-thick ALD-HfO_2 gate insulator. The deposition temperature was the same as the deposition before the Hall patterning. Finally. the counter electrode consisting of Cr(2)/Cu(50)/Au(10) was formed by using lift-off process.

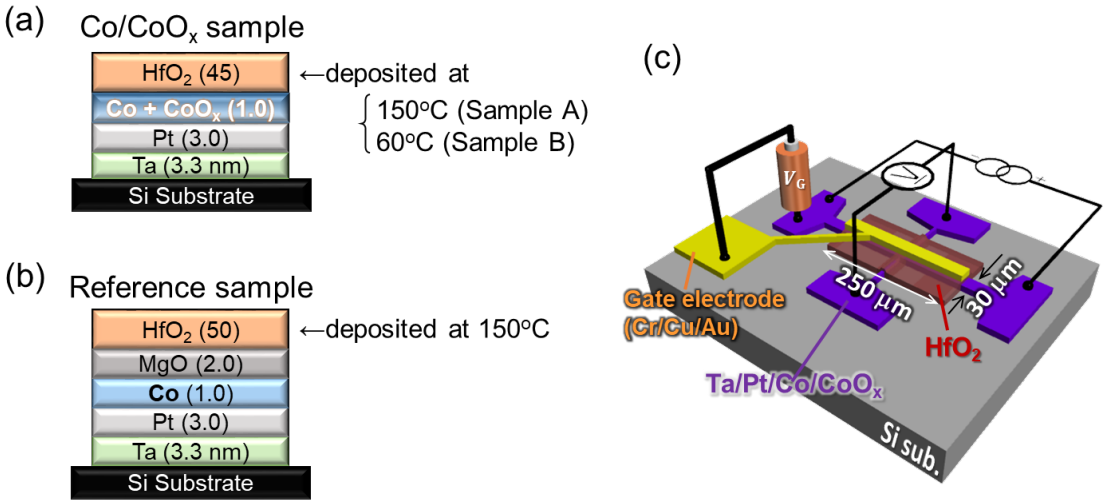

Figure 4.4: (a), (b) The layered structure for Co/CoO_x (naturally-oxidized) and reference (non-oxidized) samples, respectively. (c) Schematic illustration of the device structure and experimental setup [171].

4.3 Basic properties of Co/HfO_2 structure

Before the EF effect measurement, the basic properties including the structural, chemical, and magnetic properties of the Co/CoO_x and the reference samples were investigated. All measurements were carried out at room temperature. The oxidation state of two samples was determined using XAS (shown in Fig. 4.5(a)). Note that the deposition temperature of the HfO_2 insulating layer was 150°C in both samples for XAS measurement. The XAS measurement were performed at SPring-8 BL25SU. The XAS intensity for the Co/CoO_x sample shows clear splitting of Co L_3-edge, which confirms the formation of CoO_x on the Co surface. On the other hand, no clear appearance of the this oxidation state in the reference sample [172]. Our previous XPS experiment also shows that the Co layer was not oxidized [27]. Fig. 4.5(b) shows the cross-sectional annular dark-field scanning transmission electron microscopy (STEM) image for the Co/CoO_x sample [173]. The sample for the STEM measurement was deposited on a polished quartz substrate. The STEM measurement was conducted with the cooperation of Research Center for Magnetic and Spintronic Materials in National Institute for Materials Science. The continuous layers with smooth interfaces can be observed. Pt underlayer was suggested to orient along fcc(111) direction, which is consistent with our previous researches [26, 27].

In order to measure the 2-wire resistance $R_{2\text{wire}}$ and the anomalous Hall resistance R_{Hall}, a dc current of 40 μA and the out-of-plane external magnetic field was applied to the samples. Magnetization curves observed in R_{Hall} are shown in Fig. 4.6(a). A clear square hysteresis curve was shown in the Co/CoO_x sample, indicating that this sample had out-of-plane easy axis, whereas the curve for the reference sample suggested that the perpendicular to the plane direction was a hard axis for the magnetization. Fig. 4.6(b) shows the out-of-plane field dependence of the areal magnetic moment $m_\perp/S$ for the two samples measured using a SQUID magnetometer. Here, S is the total area of the magnetic mesa device. Similar magnetization curves as those observed in R_{Hall} graph can be obtained. The saturation values of $m_\perp/S$ were 0.63 mA and 1.65 mA for the Co/CoO_x sample and the reference sample, respectively. The effective ferromagnetic thickness $t_{\text{Co}}^{\text{eff}}$ and the oxidation thickness of the Co layer t_{CoO} are calculated to 0.38 and 0.62 nm, respectively. Since the areal perpendicular magnetic anisotropy (PMA) energy derived from Pt/Co interface [25, 65] was expected to

be unchanged after natural oxidation, two scenarios were considered to be the reason of the enhancement in PMA observed in Co/CoO$_x$ could be caused from Co/CoO$_x$ interface and/or the bulk Co internal. The modification of the interfacial PMA resulted from the hybridization of Co-O orbits [59, 62, 174–176] is one possible contribution of this effect. However unlike the previous experimental studies [174–176], in our case, the saturation $m_\perp/S$, i.e., the effective t_{CoO} was dramatically decreased after natural oxidation. Thus the decrease in the demagnetization energy and the crystalline anisotropy energies due to the reduction of t_{CoO} could more effectively cause the increase in the total areal PMA energy.

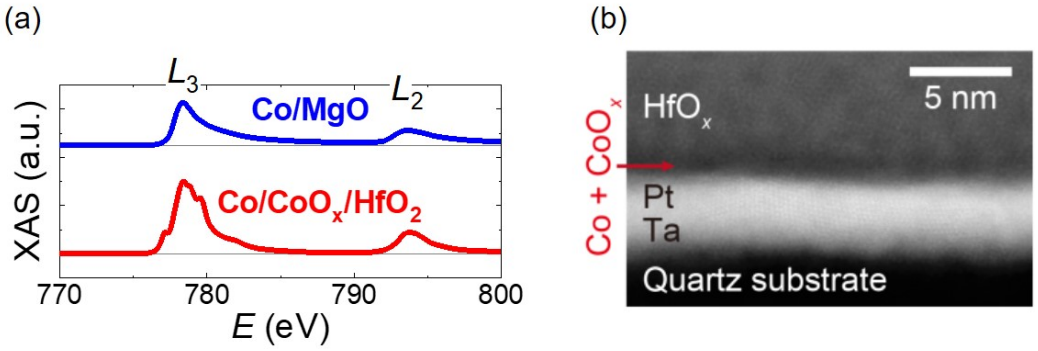

Figure 4.5: (a) The polarization-averaged XAS spectra for the Co/CoO$_x$ sample and the reference sample [172]. (b) Cross-sectional annular dark-field scanning transmission electron microscopy image for the Co/CoO$_x$ sample [173].

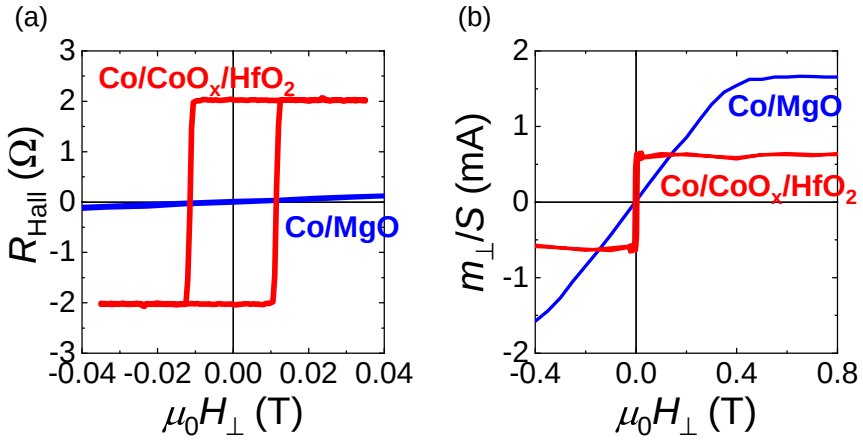

Figure 4.6: The results of (a) Hall measurement and (b) magnetization measurement for the Co/CoO$_x$ sample and the reference sample [171].

4.4 Electric-field effect on magnetism in 150°C-HfO_2

Hall measurement

First, we take a look at the results of EF control of magnetism using HfO_2 dielectric layer with the optimal fabrication condition. Fig. 4.7(a) shows the R_{Hall} loops under $V_{\mathrm{G}} = +7,\ 0,\ -7$ V measured by sweeping an external out-of-plane magnetic field. Even though CoO_x existed on the Co surface, a clear increase (decrease) in the coercivity H_{c} was obtained at $V_{\mathrm{G}} = +7\,(-7)$ V, which is same tendency as the previous study [177]. Fig. 4.7(b) shows the hard axis magnetization curves for positive and negative V_{G}s. From these curves, we calculated the areal MA energies at each V_{G}. The efficiency of the EF control of MA β_{S} was determined to be ~230 fJ/Vm, which was much larger than the values for the unoxidized samples [27,121,178]. We realized the surface oxidation is one of the way to enhance the EF control of MA. We consider the in-plane hybridization of Co and O orbits causes this present enhancement on EF effect, which is analogous to the previous study [59]. Figs. 4.8 (a) and (b) show the theoretical calculation results of Fe/MgO and Fe/FeO/MgO system. Ref. [59] shows that the additional in-plane orbital hybridization between Fe and O pushes the d_{xy} and d_{xz} bands above Fermi energy, resulting that the change in MA and EF effect on MA.

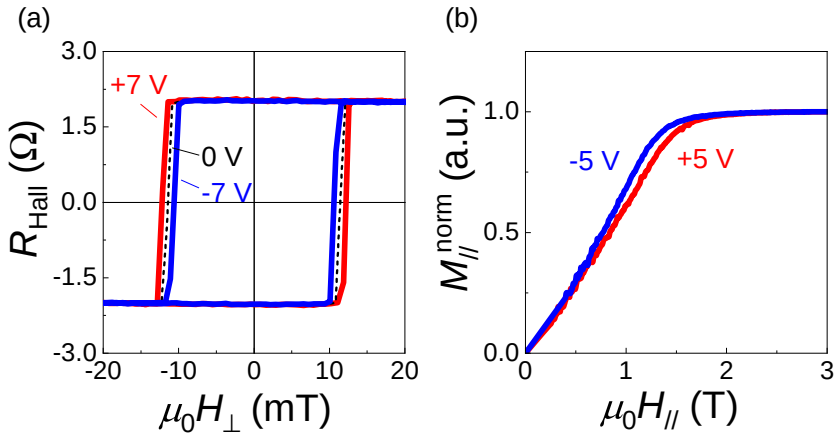

Figure 4.7: The results of EF gating experiment for the sample with 150°C-HfO_2. The vertical axis of (a) is Hall resistance and (b) is the normalized in-plane component of the magnetization [171].

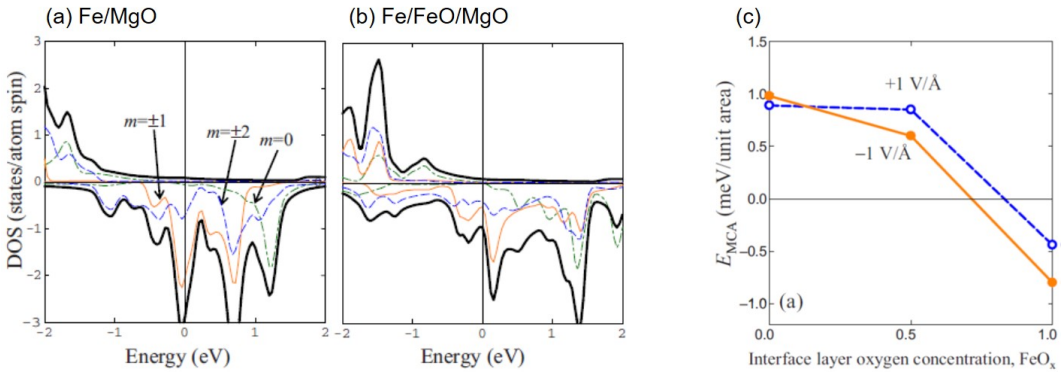

Figure 4.8: Density of states for the interfacial Fe layer for (a) Fe/MgO and (b) Fe/FeO/MgO systems. (c) Interfacial oxygen concentration dependence of MA for the external positive and negative electric field [59].

Repetitive transport measurement

In order to check the reversibility and reproducibility of the change in H_c, we repeatedly measured the R_{Hall} loops in an isochronal manner while controlling V_G value. Fig. 4.9 shows, from the top panel, V_G, $\mu_0 H_c$, squareness ratio R^r_{Hall}/R^s_{Hall}, which is the ratio of the remanent R_{Hall} to the saturated R_{Hall}, 2-wire resistance R_{2wire}, and gate leak current I_G as a function each Hall loop measurement. Here, I_G means the current flowing between the top gate electrode and the source contact. The measurement time for measuring one Hall loop and the interval between each measurement were 35 s and 60 s, respectively. H_c is changed following to the applied V_G value and always recovers promptly to the initial value at V_G = 0 V, confirming the reversible EF-control of H_c. Further, I_G is not changed if V_G is set to the constant value and the change in R_{2wire} was <~0.03% [179], which suggests that there is no onset of an irreversible chemical effect and the charge accumulation effect can be reasonably explained for the EF effect on H_c and PMA in the present sample.

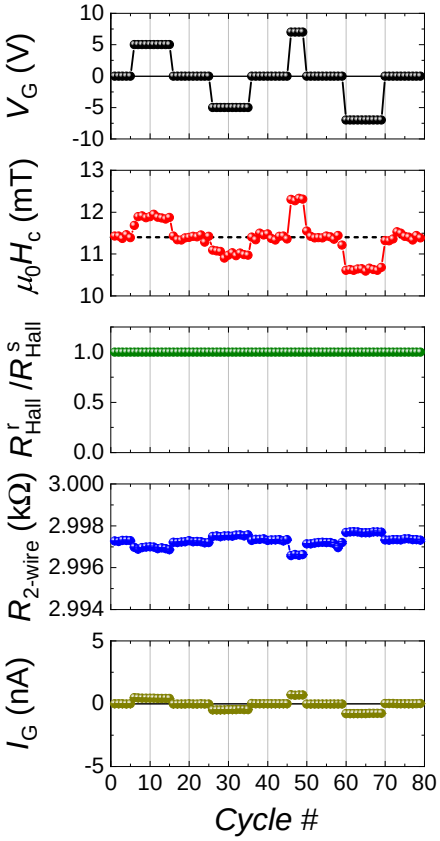

Figure 4.9: Gate voltage V_G, coercivity $\mu_0 H_c$, squareness ratio R^r_{Hall}/R^s_{Hall}, 2-wire resistance R_{2wire}, and gate leak current I_G as a function of the cycle number of each Hall loop measurement for the sample with 150°C-HfO_2 [171].

4.5 Electric-field effect on magnetism in 60°C-HfO_2

Repetitive transport measurement

In contrast to Sec. 4.4, the results of a similar experiment for the sample with 60°C-HfO_2 show a clear sign of the irreversible chemical-like effect. In Fig. 4.10, H_c, R^r_{Hall}/R^s_{Hall}, and R_{2wire} gradually changed after switching V_G, suggesting that a much slower modulation of the electronic state dominantly appeared than that induced by the charge accumulation. In addition, the magnitude of I_G was larger than that in the sample with 150°C-HfO_2, implying that this I_G is probably dominated by the reaction current at the surface of oxidized-Co and/or the ion current in the HfO_2 layer. Furthermore, the change in R_{2wire} is up to -8.1% and +2.8%

for V_G = +5 V and −5 V, which is two orders of magnitude larger [180] than that in the sample with 150°C-HfO_2. To examine the result more carefully, the typical R_{Hall} loops at each cycle are shown in Fig. 4.11. A clear square hysteresis can be seen at the initial state (cycle #1). H_c was slightly increased in the first positive V_G(= +5 V) application (~cycle #10). Then, the application of the negative V_G(= −5 V) reduces H_c as shown in the curves for cycle #30-40, but R^r_{Hall}/R^s_{Hall} remains at ~1. In keeping V_G = −5 V, the curve had almost no coercivity, and R^r_{Hall}/R^s_{Hall} became zero (cycle #50–60). We note that the Co layer was defined as the anode side during the negative V_G application, and the oxidation reaction is expected to be dominant. Thus, the curve with no coercivity obtained here probably resulted from a transition into the paramagnetic phase caused by the reduction of the effective ferromagnetic Co thickness. When V_G was switched back to zero (~cycle #63), the paramagnetic-like curve was kept, indicating that no further voltage-driven chemical reaction was induced. Subsequently, H_c increased and R^r_{Hall}/R^s_{Hall} recovered to ~1 at the beginning of the second positive V_G application (cycle #70-120), but gradually decreased even though V_G remained +5 V (cycle #130-170). In this case, the curve was changing from the square shape into the linear response, suggesting that the gradual easy axis switching from out-of-plane to in-plane direction occurred due to the enhancement of demagnetizing energy attributed to the increase in the effective ferromagnetic thickness by the redox reaction [52, 53]. After applying the negative V_G for a short time, the square hysteresis is reappeared (cycle #200), evidencing that PMA became dominantly. The non-volatility feature was also seen when V_G was set to 0 V (cycle #180-190 and cycle #210-260), indicating again that the chemical reaction was absent. To summarize, the results obtained here clearly indicated that the change in magnetism was induced by the electrochemical reaction in this sample.

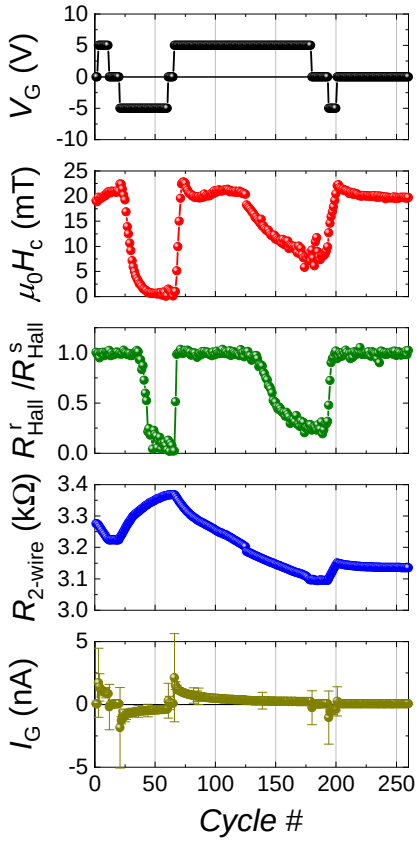

Figure 4.10: Gate voltage V_G, coercivity $\mu_0 H_c$, squareness ratio R^r_{Hall}/R^s_{Hall}, 2-wire resistance R_{2wire}, and gate leak current I_G as a function of the cycle number of each Hall loop measurement for the sample with 60°C-HfO_2 [171].

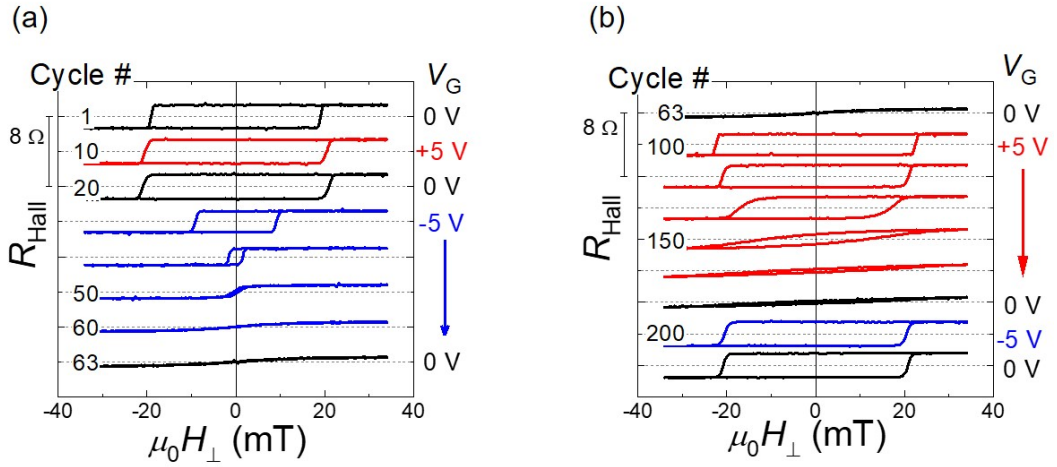

Figure 4.11: (a) First half and (b) Second half of the Hall loops at each cycle for the sample with 60°C-HfO_2 [171].

Magnetization measurement

We take a look at the results of the EF effect on the magnetic moment. For the enhancement of the signal for SQUID measurement, we prepared the capacitor structure which has larger area than that for the transport measurement (shown in Fig. 4.12(a)). Similar results were obtained in the magnetization curves measured using MPMS shown in Figs. 4.12(b) and (c). Each magnetization loop was measured at V_G = 0 V after gating with the values indicated in the graphs. The spin reorientation was shown in the process of the long-time positive V_G application, and the sample showed paramagnetic-like behavior after the application of negative V_G for along time. Importantly, the saturation $m_\perp/S$ always increased (decreased) after the positive (negative) V_G application, which implied that the reduction (oxidation) of the Co layer induced by applying the positive (negative) V_G caused the increase (decrease) in the effective ferromagnetic thickness t_{Co}^{eff}. Thus, the change in t_{Co}^{eff} may also play an important role in the modulation of the PMA of the system.

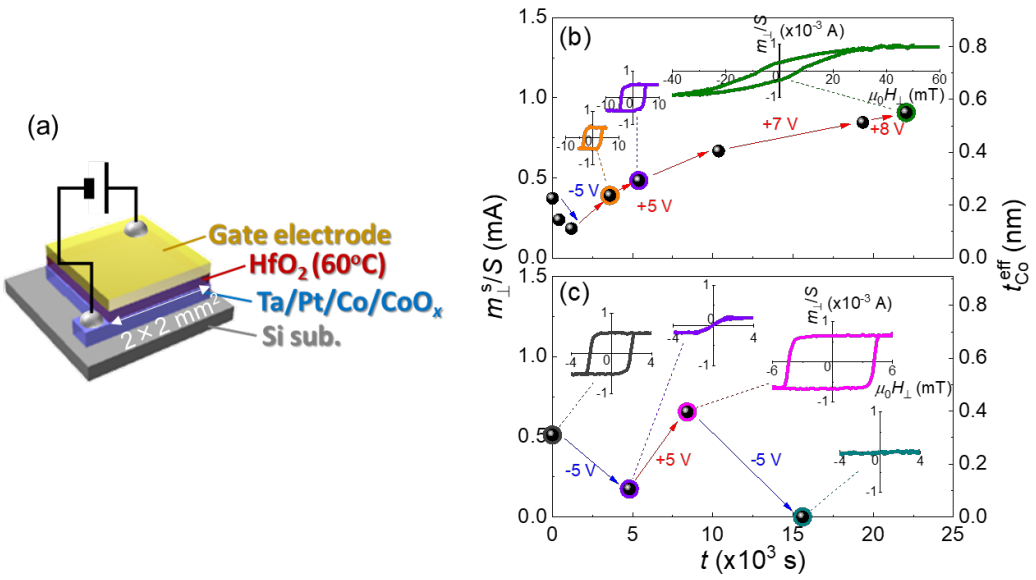

Figure 4.12: (a) Schematics of the device structure for the magnetization measurement. The area for this device was 4 mm^2. (b) and (c) The time charts of the change in the saturation magnetic moment by the V_G application for the samples with the different Co deposition thickness. t_{Co} = 0.85 nm and t_{Co} = 0.92 nm for (b) and (c), respectively. The typical magnetic hysteresis curves at each point were shown in the insets [171].

In order to check the actual metallic Co thickness in the paramagnetic-like phase ($t_{\mathrm{Co}}^{\mathrm{eff}}$ = 0 nm) shown in Fig. 4.12(c), we investigated temperature T dependence of the spontaneous magnetic moment. Black data in Figs. 4.13(a) and (b) show out-of-plane anomalous Hall curve at 300 K and T dependence of the areal magnetic moment under out-of-plane magnetic field $\mu_0 H_\perp$ = 0.2 mT for non-gated Pt/Co film with 60°C-HfO$_2$, respectively, where $t_{\mathrm{Co}}^{\mathrm{eff}}$ was estimated to be 0.49 nm (Pristine state). T_{C} in Pristine state was over 350 K. By applying −15 V for about 100 s, the paramagnetic-like R_{Hall} was accomplished (−15 V state: blue data in Fig. 4.13(a)). In Fig. 4.13(b), the spontaneous areal magnetic moment and $t_{\mathrm{Co}}^{\mathrm{eff}}$ at 300 K were decreased to zero, as obtained in Fig. 4.12(c). However, the magnetic moment in −15 V state revived below ~270 K, which implied that, in −15 V state, the metallic Co existed and the present paramagnetic-like R_{Hall} was not caused by the oxidation of whole Co layer but by the decrease in T_{C} below 300 K. From the value of the areal magnetic moment at 230 K, $t_{\mathrm{Co}}^{\mathrm{eff}}$ in −15 V state was calculated to be 0.25 nm. Moreover, as observed in non-oxidized Pt/Co samples [24], the spontaneous magnetic moment rapidly decreased below T_{C} due to the transformation from a single domain to a multi-domain state as observed in non-oxidized Pt/Co samples, suggesting that the voltage-induced chemical reaction in Co occurred uniformly in the film plane.

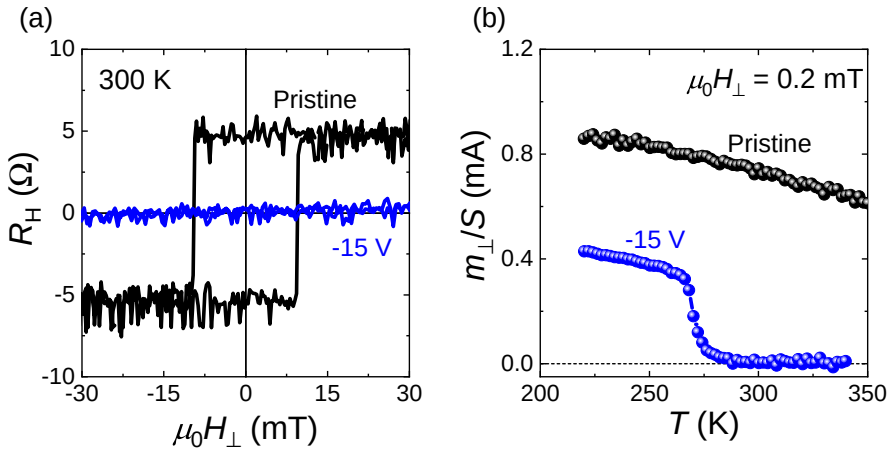

Figure 4.13: (a) R_{Hall} curves and (b) T dependence of the areal magnetic moment under $\mu_0 H_\perp$ = 0.2 mT of the Pt/Co film for Pristine and −15 V states.

4.6 Capacitive properties

In order to realize the difference in the capacitive characteristics of two samples, we investigated the frequency dependence of the capacitive properties using LCR meter (Keysight E4980A). Fig. 4.14(a) and Fig. 4.14(b) show the the ac frequency f dependence of the capacitance C and the phase angle θ for two samples. In the sample with 150°C-HfO_2, the characteristic of $C-f$ and $\theta-f$ shows almost flat for a wide range of the frequency. Especially, the value of θ shows almost $-90°$, which indicates that a conventional solid-state capacitor was formed and the electron charging/discharging effect was dominant mechanism of the present EF effect on magnetism in this sample. We note that the deviation of θ from $-90°$ was attributed to the existence of the background series resistance, such as the channel resistance of the Hall bar without the coverage of the gate electrode. On the other hand, the capacitive characteristics in the sample with 60°C-HfO_2, is completely different from those of the sample with 150°C-HfO_2. These characteristics strongly imply the existence of some mobile charged-ion in the HfO_2 fabricated at 60°C. In the low f region (<10^2-10^3 Hz), the value of C was much higher than that of the sample with 150°C-HfO_2 and θ largely deviated from $-90°$ and got closer to 0°, which is suggested to be induced by chemical reaction at the interface. In the middle f band (10^2<10^4 Hz), the peak of $\theta-f$ graph was seen. The decrease in C was also observed in this region, which is supposed to the current resulting from ion migration by the ac EF application. Because the drift of the ions is generally not very fast, ions cannot follow the ac EF above 10^4 Hz, resulting that θ approached $-90°$, which corresponds to the charging effect between the Co surface and the top gate electrode. The reason why C was slightly lower than that for the sample with 150°C-HfO_2 in this high f region was probably attributed to the difference in the thickness or the dielectric permittivity related with the different quality of the HfO_2. We note that this peculiar characteristic of the capacitive properties was similarly observed in the system using liquid gating such as electric double layer capacitance [181].

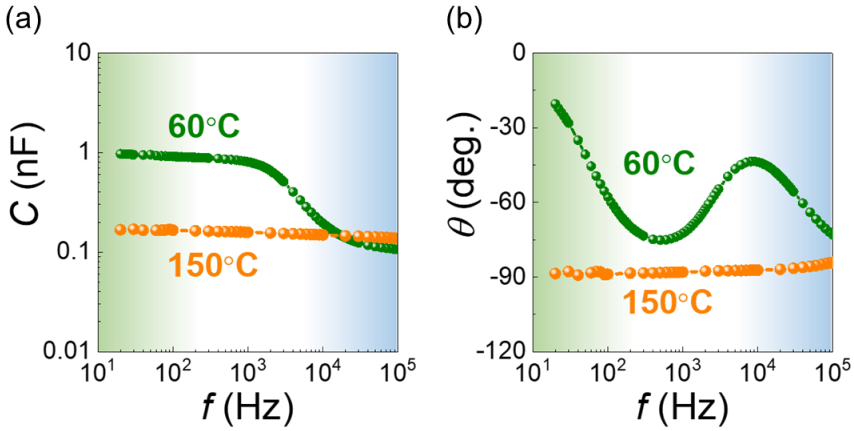

Figure 4.14: (a) C-f and (b) θ-f plots for the sample with 150°C-HfO_2 and 60°C-HfO_2 [171].

4.7 XPS measurement

Finally, we examined the difference in the chemical state of two HfO_2 layers by means of the XPS measurement. Figs. 4.15(a) and (b) show the Hf-4f spectra measured by the angle-resolved XPS for 150°C-HfO_2 and 60°C-HfO_2, respectively. Here, the black broken lines represent each chemical state of Hf estimated by the spectral Gaussian fitting analysis. We found that the composition ratio of the 150°C-HfO_2 layer (Hf : O) is completely 1 : 2. On the other hand, the HfO_2 layer fabricated at 60°C was consist of two chemical compositions. One component is made of HfO_2' which has larger oxygen concentration compared to a pure HfO_2. Previous studies have reported that the unusual peroxide hafnium oxide, e.g. HfO^{3+} and HfO_2^{2+} can exist in the thin films produced by the ion-beam sputtering or gas-phase oxidation [182, 183]. In contrast, the chemical formula of the other component was not well understood so far. However, we deduced that this component corresponded to a hafnium oxide having oxygen defects because the peak intensities of this un-known component appeared within the lower energy region. Therefore, the oxygen distribution in the 60°C-HfO_2 layer is expected to be inhomogeneous. It was difficult to determine the accurate distribution of oxygen ions, but in terms of the ionization tendency, the interfacial Hf ions were likely to be over-oxidized because the ionization tendency of Hf ions is larger that of Co ions.

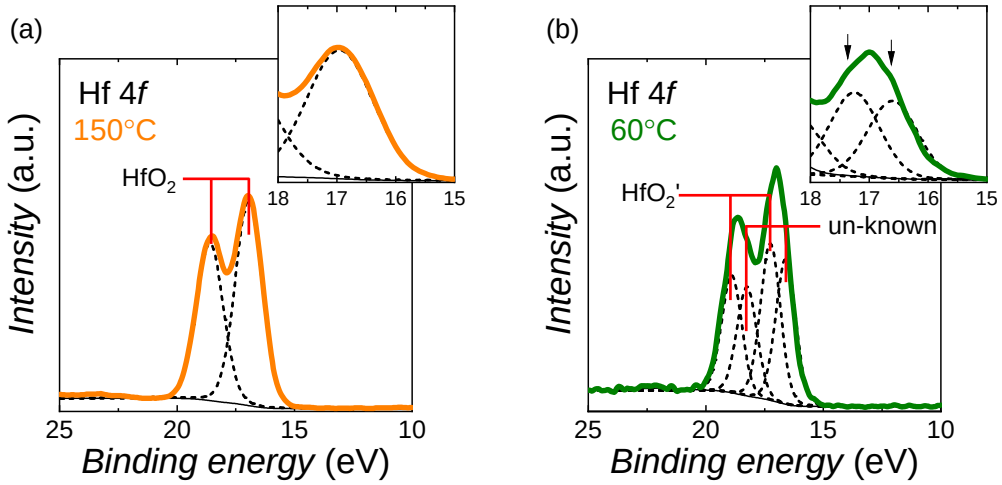

Figure 4.15: Hf-4f angle-resolved XPS spectra for (a) 150°C-HfO_2 and (b) 60°C-HfO_2.

4.8 Summary of this chapter

In this chapter, we have examined EF effect on magnetism in surface-oxidized Co with two types of the ALD-HfO_2 gate dielectric layer. The repetitive anomalous Hall measurements at different V_G and the impedance measurements have shown the mechanism of the EF modulation of magnetism dramatically depends on the quality of the dielectric oxide. A purely electronic EF effect on magnetism is obtained by using HfO_2 fabricated in the optimal ALD-fabrication condition. In addition, we find that an oxidation treatment to Co surface greatly affects PMA of the Pt/Co film and its EF effect. In contrast, mobile ions are substantial inside a low temperature fabricated HfO_2, resulting a redox-induced change in the effective ferromagnetic thickness. The results obtained here establish the basic fabrication method for not only making choice the performance of the field-effect devices but also introducing the further interface design in other spintronics phenomena.

Chapter 5

Electric-field control of exchange bias in Co/HfO_2 system

We investigated the electric-field (EF) effect on the exchange bias (EB) effect in the naturally surface-oxidized Co electrode. The oxidation treatment was same as in Chap. 4. We deduced the antiferromagnetism in the oxidized Co (CoO_x) and the perpendicular EB at low temperature by measuring anomalous Hall effect. We also confirmed that the EB field, as well as the coercivity, was modulated by the gate EF application at the Co/CoO_x interface below the blocking temperature (T_B). The EF modulation ratio of the EB field presented a strong temperature dependence, and it increased as the temperature approaches to T_B, while the EF change in the sheet resistance R_{sheet} did not show any temperature dependence. These results were most likely caused by the modification of an electronic state at Co/CoO_x interface by EF effect, which was fundamentally different from the case in systems using magnetoelectric (ME) or mutiferroic materials.

5.1 Introduction

5.1.1 Exchange bias effect

In a bilayer consisting of a ferromagnetic (FM) layer and an antiferromagnetic (AFM) layer (Fig. 5.1(a)), an EB effect can be emerged through field cooling (FC) process [184]. After FC of the FM/AFM layered system below the Néel temperature (T_N), the magnetic hysteresis loop is shifted along the applied magnetic field direction (Fig. 5.1(b)). The EB effect which originates from the exchange interaction between interfacial FM and AFM atoms adds a unidirectional (not a uniaxial) magnetic anisotropy (MA) in the FM layer [185–187]. EB is often utilized to form the magnetization pinned layers in GMR or TMR devices [188–190] (Fig. 5.1(c)). Moreover, it is known that the EB assists the magnetization switching. Fig. 5.1(d) shows the applied current dependence of the anomalous Hall resistance measured at zero magnetic field in Pt/PtMn/$[Co/Ni]_2$ structure. In this system, the combination of the spin-orbit-torque generated by the current-flowing in PtMn and the unidirectional effective in-plane field caused by EB at the interface of PtMn and Co/Ni multilayer assisted an external field free magnetization switching of the perpendicularly magnetized Co/Ni multilayer [191].

We have presented the Meiklejohn-Bean (MB) model, which is generally used to explain the origin of the EB effect. According to this model, the magnetic energy per unit area E for the exchange-biased system is described as

$$E = -Ht_{FM}M_s \cos(\theta - \beta) + t_{FM}K_F \sin^2\beta + t_{AFM}K_A \sin^2\alpha - K_J \cos(\beta - \alpha). \quad (5.1)$$

Here H is the applied magnetic field, M_s is the saturation magnetization, t_{FM} (t_{AFM}) is the thickness of FM (AFM) layer, K_F (K_A) is the anisotropy of FM (AFM) layer, and $K_J = Js_{FM}s_{AFM}$ is the interfacial exchange energy, where J is the exchange constant between FM and AFM spins s_{FM} (s_{AFM}) is the spin vector of FM (AFM). β, α and θ are the angles between the magnetization and the K_F vector, the magnetization of AFM sublattice and the K_A vector , and the applied field and K_F vector, respectively. Note that the it is assumed that the K_F and K_A vector are always along to the same direction. On the simplest assumption that the contribution of FM anisotropy is negligible ($t_{FM}K_F \ll t_{AFM}K_A$) [185, 187, 192], Eq.

5.1 becomes

$$E = -Ht_{\mathrm{FM}}M_{\mathrm{s}}\cos(\theta-\beta) + t_{\mathrm{AFM}}K_{\mathrm{A}}\sin^2\alpha - K_J\cos(\beta-\alpha). \tag{5.2}$$

By minimizing E with respect to α and β, we obtain following two equations:

$$\frac{K_J}{t_{\mathrm{AFM}}K_{\mathrm{A}}}\sin(\beta-\alpha) = \sin 2\alpha, \tag{5.3}$$

$$\frac{Ht_{\mathrm{FM}}M_{\mathrm{s}}}{K_J}\sin(\theta-\beta) = \sin(\beta-\alpha). \tag{5.4}$$

When the magnetic field is applied parallel to the AFM orders, the shifted field of the hysteresis loop H_{EB} is estimated as

$$H_{\mathrm{EB}} = -\frac{K_J}{t_{\mathrm{FM}}M_{\mathrm{s}}}, \tag{5.5}$$

which is called as the exchange bias field. In addition, we obtain that

$$K_J < t_{\mathrm{AFM}}K_{\mathrm{A}} \tag{5.6}$$

is required for the emergence of EB from a rule of thumb. Under the condition of $K_J < t_{\mathrm{AFM}}K_{\mathrm{A}}$, the system is minimized by keeping α small, which is independent with β. However, if $K_J \gg t_{\mathrm{AFM}}K_{\mathrm{A}}$ is qualified, the system is minimized by keeping $\beta-\alpha$ small, resulting that FM and AFM spins rotate together, which indicates no existence of the unidirectional anisotropy.

Furthermore, according to the theoretical study for the generalization of MB model [193, 194], the interfacial exchange energy K_J is described as

$$K_J = \frac{A_{\mathrm{A-F}}}{\zeta}\ (\lambda < 1), \tag{5.7}$$

$$K_J = 2\sqrt{K_{\mathrm{A}}A_{\mathrm{A}}}\ (\lambda > 1), \tag{5.8}$$

where A_{A}, $A_{\mathrm{A-F}}$, ζ are the exchange stiffness of AFM layer and AFM/FM interface, and the distance between interfacial AFM and FM atoms, respectively. λ is defined as $A_{\mathrm{A-F}}/2\zeta\sqrt{K_{\mathrm{A}}A_{\mathrm{A}}}$.

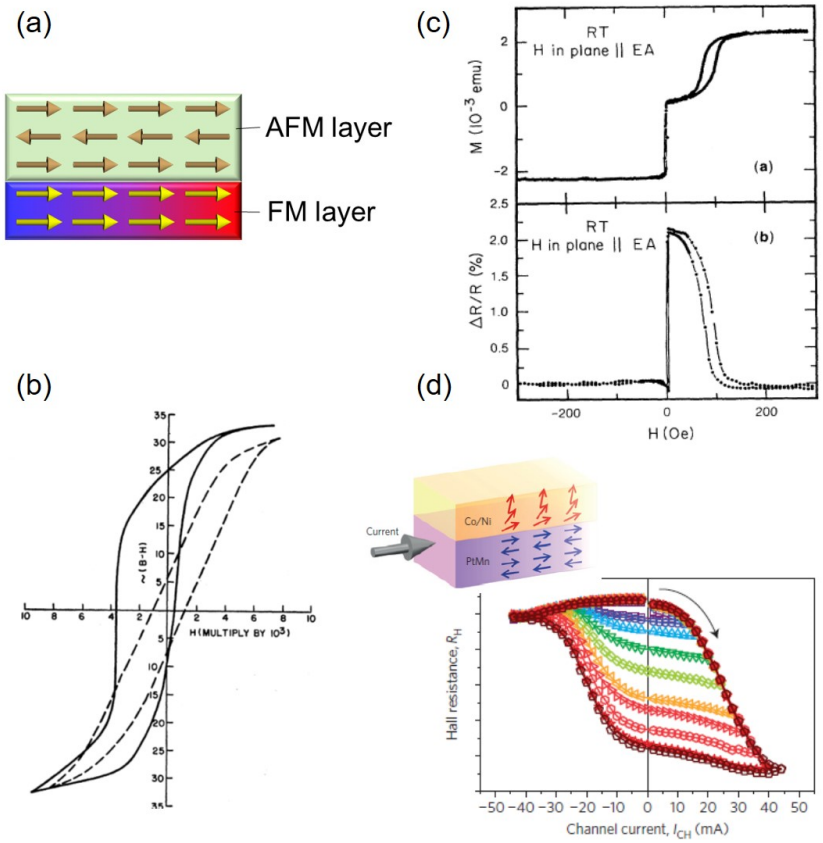

Figure 5.1: (a) Schematics of the FM/AFM bilayer system. (b) Hysteresis loops of the oxide-coated of Co at 77 K. The solid line show the hysteresis loop under the correct FC process. The dashed line shows the hysteresis loop when the sample was cooled in the zero magnetic field [184]. (c) Magnetization curve (upper) and the curve of magnetoresitance ratio for the GMR devices consisting NiFe/Cu/NiFe/FeMn [188]. (d) The current dependence of the anomalous Hall resistance measured at zero magnetic field. Schematics of PtMn/Co/Ni multilayer system [191].

5.1.2 Electrical control of exchange bias

It is known that EB in magnetoelectric-multiferroic AFM/FM heterostructures can be manipulated by an EF application [195–200]. Magnetoelectric-multiferroic materials simultaneously possess ferroelectric (FE) and FM properties in the same phase and exhibit an internal coupling between FE order (electrical polarization: P) and FM order (magnetization: M), called magnetoelectric (ME) coupling. The presence of P-M coupling enables us to control M (P) by applying an electric field (magnetic field), which is called the ME effect (Fig. 5.2(a)). Therefore in multiferroic AFM/FM systems, the applied EF causes a change in the

AFM order, resulting in a change in the EB field. Moreover, magnetoelectric random access memory (MERAM), where the ME magnetization reversal of one FM layer in MTJ structure stacked on an ME-AFM layer was offered by ME switching of AFM domain, was proposed for a next-generation non-volatile memory as well as MRAM (Fig. 5.2(b)).

As shown in Fig. 5.2(c), in 2005-2006, the ME manipulation of EB have been experimentally reported with an ME-AFM Cr_2O_3 [195] and a multiferroic-AFM $YMnO_3$ [196], but its demonstration was only limited at low temperature. Recently, room-temperature (RT) ME switching of EB was reported by using multiferroic-AFM $BiFeO_3$ [197]. One of the serious issues is how to realize a design of multiferroic materials with such a strong ME effect at RT [201]. Another possible way to manipulate the EB effect is utilizing a voltage-driven magneto-ionic effect. The mechanism of the magneto-ionic modulation of EB is a change in the thickness of FM and AFM layers. Thus, this modulation was demonstrated using non-ME multiferroic NiO and NiCoO [202, 203]. On the other hand, in this study, we examine the purely EF effect on EB in a Co thin film with a CoO_x layer.

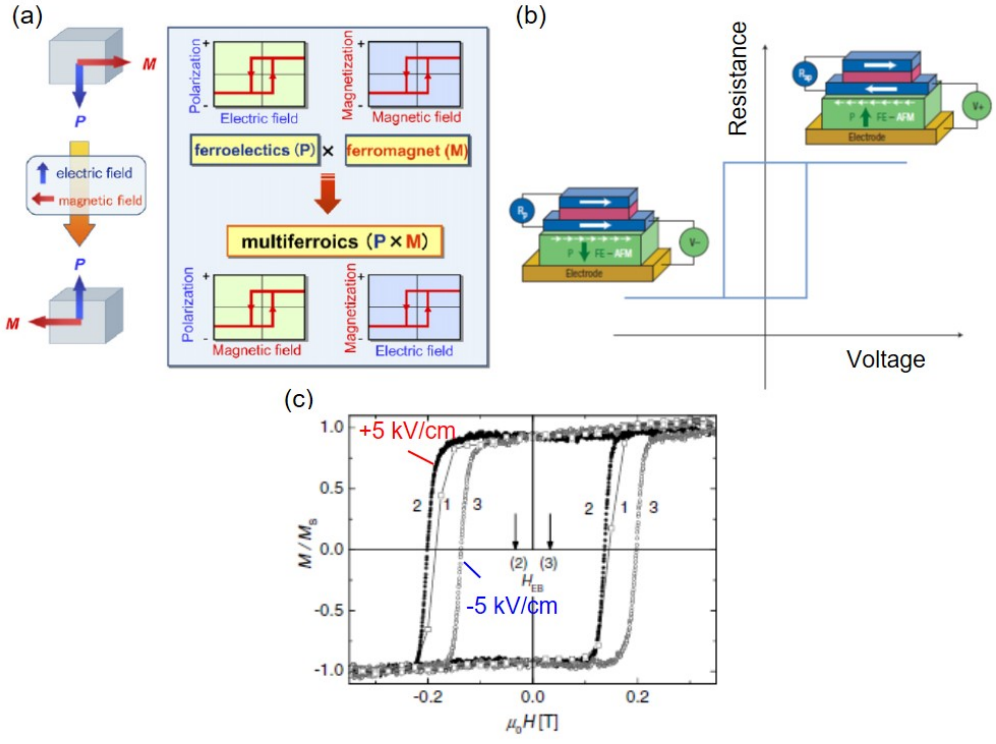

Figure 5.2: (a) A conceptual illustration of multiferroics and ME effect [201]. (b) The first demonstration of the ME modulation of EB in $[Pt/Co]_3/Pt/Cr_2O_3$ system. This figure is reproduced from [195]. (c) The schematic of MERAM [204].

5.2 Sample fabrication

The layered structure, consisting of Ta(3.3 nm)/Pt(3.0)/Co+CoO_x(1.0)/HfO_2/Cr(2)+Au(10), used in this Chapter is shown in Fig. 5.3(a). Note that numbers in the parentheses show nominal thickness in nanometer orders. The bottom electrode stack was deposited on a thermally oxidized Si substrate using rf sputtering. The sample was pattered into 30-μm-width Hall bar (Fig. 5.3(b)). The procedure of the oxidation treatment and the device fabrication is same as that in Chap. 4. We note that the ALD deposition temperature of HfO_2 dielectric layer is 150°C.

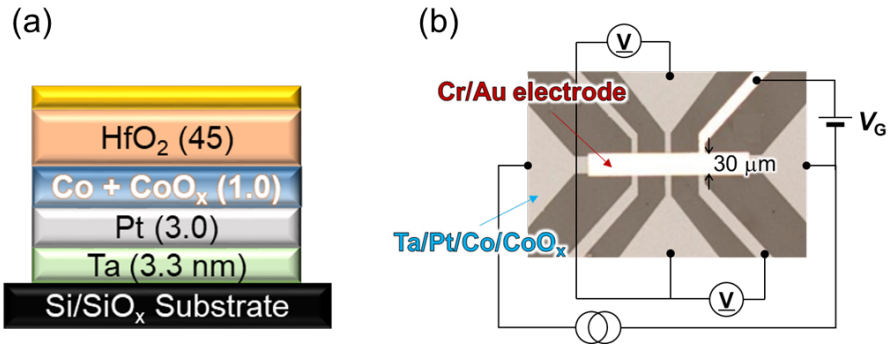

Figure 5.3: (a) The layered structure. (b) Measurement setup and optical image of the fabricated microwire.

Fig. 5.4 shows the temperature dependence of the perpendicular component of the areal saturation magnetic moment tM_s, which is quantified using SQUID magnetometer. The square hysteresis curve of the normalized perpendicular magnetic moment at 300 K is also shown in the inset of Fig. 5.4. The saturation magnetic moment is 0.39 mA at 300 K, resulting the thickness of the metallic Co and CoO_x layer is 0.24 nm and 0.76 nm, respectively. The Curie temperature T_C for the sample after oxidation process is ~370 K.

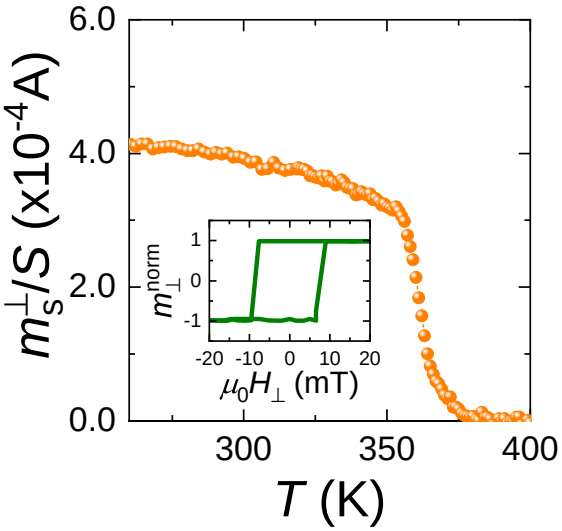

Figure 5.4: $m-T$ curve for the surface-oxidized Co sample. Inset shows the hysteresis curve of the normalized perpendicular magnetic moment at 300 K.

5.3 Temperature dependence of exchange bias

In this study, EB was introduced by the FC process from 300 K, which is higher than T_N of bulk CoO (~290 K) [205, 206]. An external magnetic field ($H_{\perp}^{FC}$) of ±3 T was applied to the parallel direction to the magnetic easy axis (out-of-plane direction) during FC. Fig. 5.5(a) shows R_{Hall} loops for V_G = 0 V at 40 K. The anomalous Hall measurement was conducted by sweeping the perpendicular magnetic field $\mu_0 H_{\perp}$ and a dc current of 100 μA was applied between drain-source channel. The clear shift of hysteresis curve toward the negative (positive) $\mu_0 H_{\perp}$ direction for the case of positive (negative) $H_{\perp}^{FC}$ was observed, suggesting that the perpendicular EB at Co/CoO$_x$ interface certainly existed. Here, we define the coercivity H_c and the exchange bias field H_{EB} as $(H_1-H_2)/2$ and $(H_1+H_2)/2$, respectively, where H_1 (H_2) is the value of the magnetic field at which the up-(down-)swept R_{Hall} curve crosses the horizontal axis. The hysteresis loops were repeatedly measured 15 times to quantify the accurate values of H_c and H_{EB} (Fig. 5.5 (b) and (c)). The decrease in H_c and H_{EB} was obtained, which is often called a training effect [193, 207–211]. The reorientation of partial AFM domains in the reversal of the FM magnetization caused the reduction of the

EB effect. This training effect was often observed in polycrystalline AFM materials and very small or almost non-existence in single crystals [209,212]. The origin of the training effect is considered to relate to a metastable spin configuration or a thermal fluctuation [187,193,208]. Temperature dependence of H_c and H_{EB} for V_G = 0 V was displayed in Fig. 5.5 (d) and (e). $|H_{EB}|$ as well as H_c increased with the decrease in the temperature. $|H_{EB}|$ became almost zero when $T >\sim$ 200 K. It has been known the EB vanishes above a temperature denoted as the blocking temperature T_B. In the present sample, T_B was estimated to be around 200 K, which was lower than T_N pf bulk CoO. One possibility of the oring of this phenomena is finite size effects [213]. The T_N is substantially decreased when the thickness of AFM is thinner than a critical dimension of the AFM layer [214].

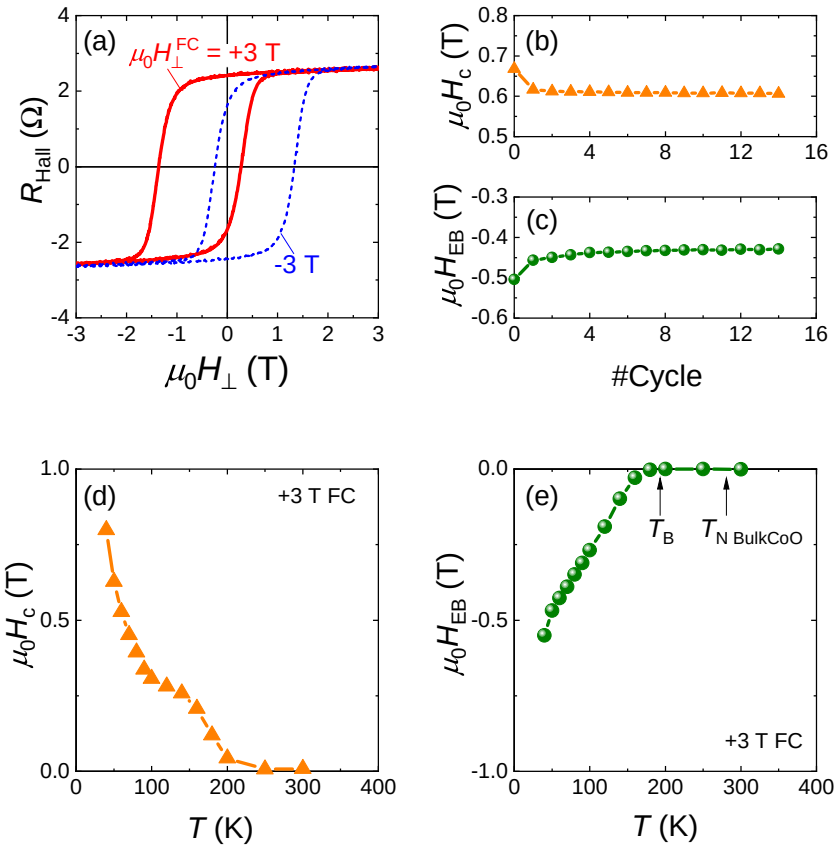

Figure 5.5: (a) R_{Hall} curve at 40 K for $\mu_0 H_\perp^{FC}$ = ±3 T. (b) H_c and (c) H_{EB} at plotted as a function of the number of Hall loop measurements. Temperature dependence of (d) H_c and (e) H_{EB} for V_G = 0 V, respectively.

5.4 Electric-field control of exchange bias field

Next, we examine the EF effect on H_c and H_{EB} in this exchange-biased system. Fig. 5.6(a) shows the hysteresis curves at 50 K under the applicaion of $V_G = \pm 10$ V obtained after $\mu_0 H_\perp^{FC} = \pm 3$ T FC process. First of all, H_c was modulated by the gating process. The value of H_c monotonically increased (decreased) at $V_G = +10$ V ($V_G = -10$ V) (Fig. 5.6(b)). The sign of the EF change in H_c is same as that in Chap. 4 at 300 K [171]. Here, nonlinear V_G dependence of H_c may be relevant to the shape of d band structure [128, 132, 215, 216]. If the derivative of d band, which determines the magnitude of the EF modulation of magnetic properties, is not constant in the vicinity of Fermi level, V_G induced change is predicted to be nonlinearly. More importantly, H_{EB}s for $V_G = +10$ V and -10 V, which are indicated by the dashed vertical lines in $V_G = +10$ V in Fig. 5.6(a), are different, suggesting that the gate EF application also modulated H_{EB}. Fig. 5.6(d) shows ΔH_{EB} ($= H_{EB}(+10\text{ V}) - H_{EB}(-10\text{ V})$) as a function of T. In the employed T range, the positive (negative) V_G always results in the increase in H_{EB}, *i.e.*, the sign of the H_{EB} modulation is independent of the measurement temperature. The magnitude of ΔH_{EB} was almost independent of T below 150 K while it decreased abruptly to zero as T approaches T_B. In contrast, H_{EB} itself shows strong temperature dependence (shown in Fig. 5.5(e)). As a result, the modulation ratio of H_{EB} ($= \Delta H_{EB}/H_{EB}(0\text{ V})$) increase with T (Fig. 5.6 (e)).

In order to check the volatility of the present EF effect, we carried out the repetitive Hall loop measurement changing the V_G value at 40 K. Fig. 5.7 shows V_G, the difference in H_c $\mu_0 \delta H_c$ ($= \mu_0 H_c(N) - \mu_0 H_c(N = 14)$) and H_{EB} $\mu_0 \delta H_{EB}$ ($= \mu_0 H_{EB}(N) - \mu_0 H_{EB}(N = 14)$), and R_{sheet} as a function of the cycle number N for each Hall measurement. H_c, H_{EB}, and R_{sheet} changed rapidly following to V_G change and no hysteresis was observed, confirming that the present EF effect was reversible and volatile.

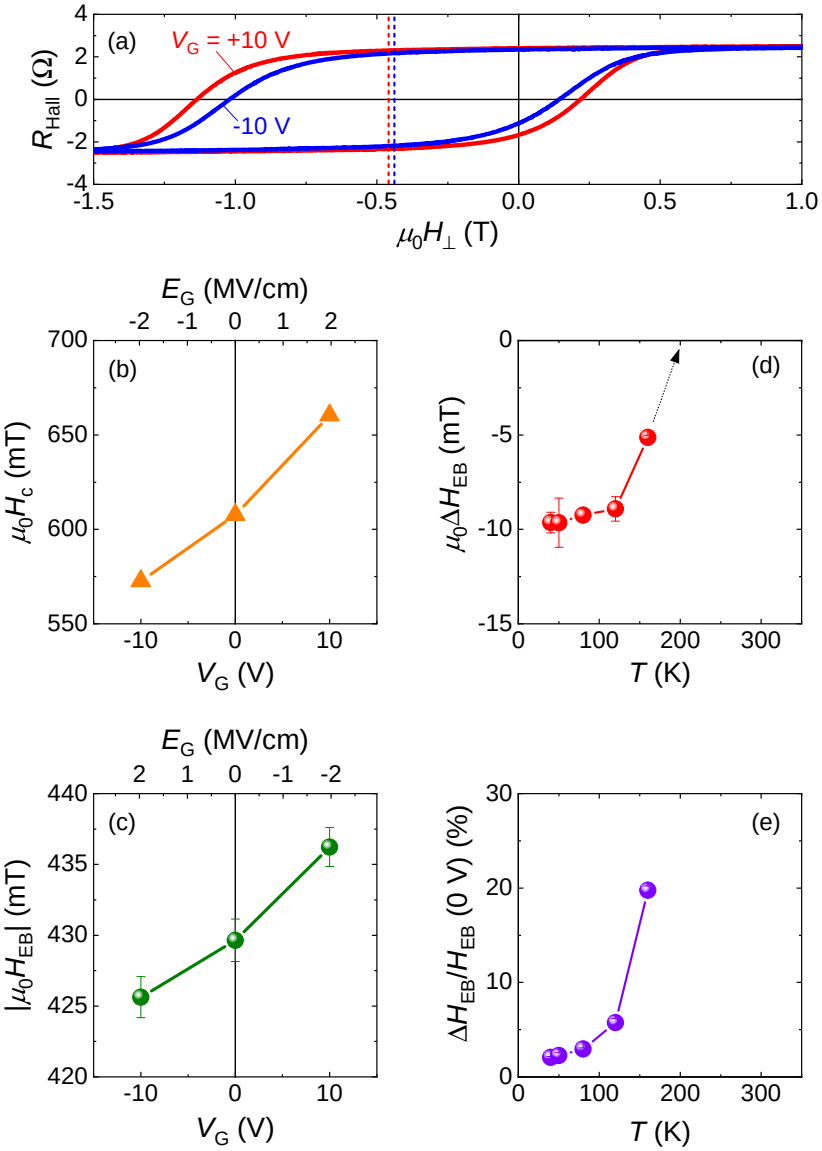

Figure 5.6: (a) R_{Hall} curves at 50 K for $\mu_0 H_\perp^{\mathrm{FC}} = \pm 3$ T under the application of $V_{\mathrm{G}} = +10$ V and -10 V. (b)H_{c} and H_{EB} as a function of V_{G} and the gate EF $E_{\mathrm{G}}(= V_{\mathrm{G}}/(t_{\mathrm{HfO_2}} + t_{\mathrm{CoO}}))$, where $t_{\mathrm{HfO_2}}$ and t_{CoO} represent the thickness of each insulating layer. (d)(e) Temperature dependence of the change in H_{EB} (ΔH_{EB}) and the modulation ratio of H_{EB} [$= \Delta H_{\mathrm{EB}}/H_{\mathrm{EB}}(0\,\mathrm{V})$], respectively.

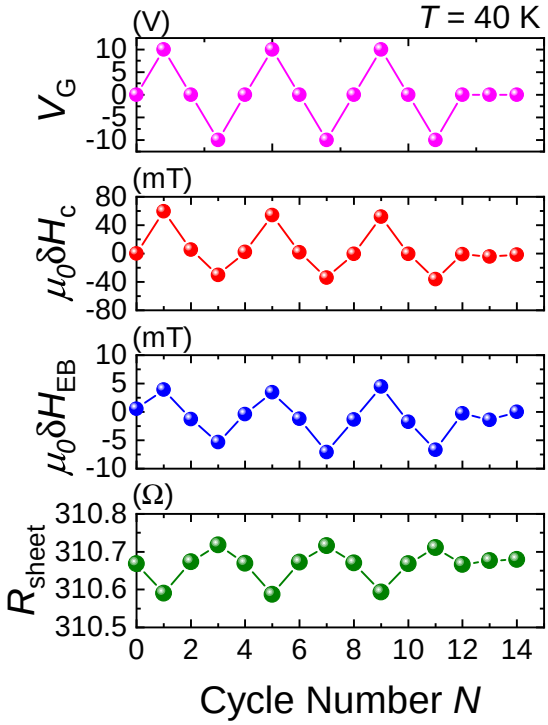

Figure 5.7: V_G, $\mu_0\delta H_c$, $\mu_0\delta H_{EB}$, and R_{sheet} as a function of the cycle number N for each Hall measurement.

Next, we discuss the origin of the EF-induced H_{EB} change observed here. The most important point is that the thermally activated effect such as the voltage-induced redox have no influence in the present EF effect. First, this EF effect showed volatile response although the chemical effect causes the nonvolatile change in magnetic properties. Second, the modulation of H_{EB} was confirmed even at low temperature. If the modulation is induced by a thermally activated phenomena, the modulation is expected to exponentially increased with T. However, ΔH_{EB} was almost constant at low T (Fig. 5.6(d)) and decreased with the increase in T. In addition, the V_G modulation of the R_{sheet} by $V_G = \pm 10$ V for the present sample is at most ~0.04% and it had no exponential relationship with T in the range from 40 to 300 K (Fig. 5.8). As shown in Chap. 4, the R_{sheet} modulation induced by the voltage-induced chemical reaction was on the order of 10% at 300 K, which was larger than th present case by two orders of magnitude. These results discussed above strongly suggested that thermally activated phenomena are not in the case with the present result. The change induced by the ME effect in the AFM layer [195–200] can be also ruled out because CoO does not show ME

effect [197]. Therefore, the modulation of the electronic state at Co/CoO_x interface, including the charge accumulation, becomes the most reasonable explanation for the EF-induced H_{EB} change observed here.

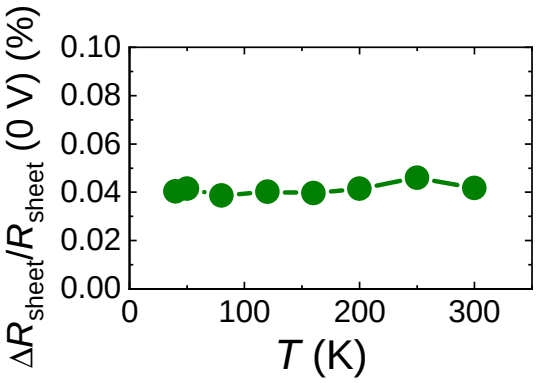

Figure 5.8: Temperature dependence of R_{sheet} modulation $\Delta R_{sheet}/R_{sheet}(0\ V)$, where ΔR_{sheet} is the difference in R_{sheet} between $V_G = +10$ V and -10 V.

Within MB model (Eq. 5.5), the change in K_J, t, and/or M_s results in the H_{EB} modulation, so we investigated the EF effect on the areal magnetic moment tM_s. Fig. 5.9 shows the V_G dependence of tM_s at 250 K measured by SQUID magnetometer. The modulation ratio of tM_s was ~0.8% per 10 V, the value and the sign of which were consistent with the previous report using non-oxidized Co electrode [36]. In addition, the change in tM_s was suggested to be almost independent with T by checking the temperature dependence of the voltage-induced change in R^s_{Hall}/R^2_{sheet}, where R_{Hall} was a saturation Hall resistance. tM_s increased (decreased) with the application of positive (negative) V_G. Thus, the sign of the H_{EB} change could not be explained from the EF-induced change in tM_s, indicating that not the modulation of tM_s but that of K_J played a crucial role in the present EF effect on H_{EB}. Furthermore, we calculated the change in t caused by the EF-induced atomic displacement at the interface on the assumption that the R_{sheet} change by the EF application (Fig. 5.7) was fully caused by the change in t, shown in Fig. 5.10. However, t change was estimated to be 1.5 pm at most. It was confirmed that such a small t change does not likely explain the present results. Note that K_J modulation was expected to result in change in T_N and T_B [217], which may be relevant to the rapid increase in the modulation ratio of H_{EB} toward T_B shown in Fig. 5.6(e), as the case of the change in MA and the remanent magnetic moment near T_C by the application of EF.

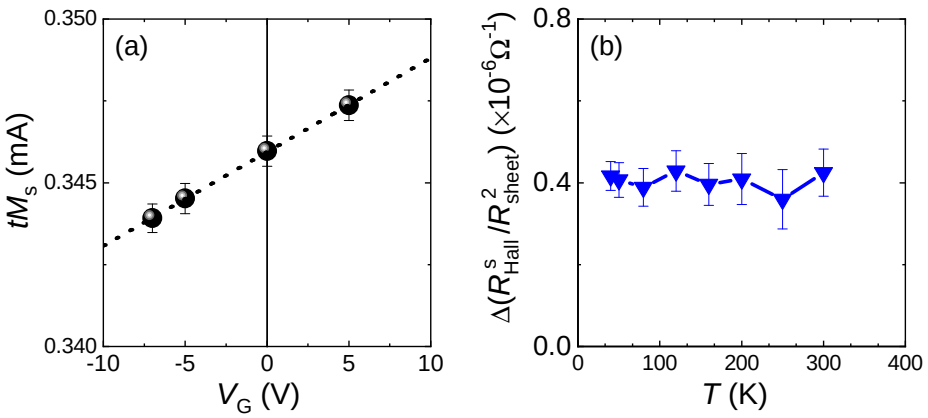

Figure 5.9: (a) V_G dependence of tM_s at 250 K. (b) Temperature dependence of the difference in R^s_{Hall}/R^2_{sheet} between $V_G = +10$ V and -10 V $\Delta R^s_{Hall}/R^2_{sheet}$.

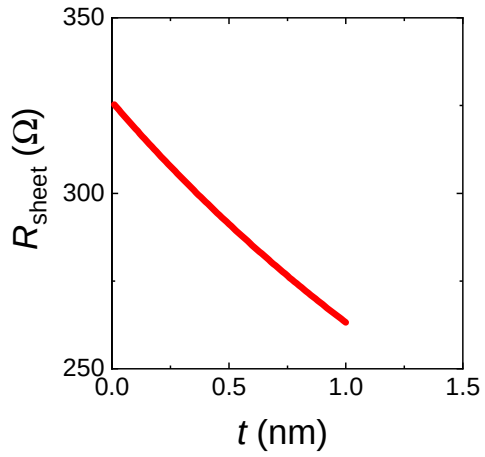

Figure 5.10: R_{sheet} calculated by assuming that the change in the R_{sheet} was fully caused by the change in t.

5.5 Plausible microscopic origins

Finally, we discussed the EF control of K_J. It has been pointed out K_J originates from the exchange interaction between the FM spins and AFM spins at the interface [184]. Based on Eqs. 5.7 and 5.8, we obtain $\lambda \sim 0.2$ by using $K_A = 2.92 \times 10^7$ J/m^3 of bulk CoO [218], the strength of the exchange interaction of CoO-CoO (−2 meV) and CoO-Co (−2 meV) [219], and the lattice constant of CoO = 0.4267 nm $\sim \zeta$. Therefore, it is found that Eq. 5.7 is the appropriate expression in our system. However, we note that the properties of CoO_x layer in our sample which is ultrathin and likely non-stoichiometric system may be different from those of bulk CoO. On the assumption that above quantitative argument is correct, the EF modification of the AFM-FM exchange stiffness A_{A-F} is suggested to be the most possible reason for the EF change in K_J. Although the EF effect on A_{A-F} has not been reported, it is possible that the EF modulation of the orbital hybridization [57], which may include the orbital occupancy [54–56], at the Co/CoO_x interface is its microscopic mechanism; this is, analogous to the case of EF effect on the exchange stiffness and the exchange interaction between FM spins [33, 36–39]. Another possibility is the EF modification of the interfacial Dzyaloshinskii-Moriya interaction (iDMI) [40–44]. Theoretical study has suggested that the iDMI between FM and AFM spins acts on the FM atom as an effective magnetic field, then contribute to the EB [220, 221]. In general, the iDMI between a ferromagnet and an oxide layers is considered to have much smaller contribution than that between a ferromagnet and a heavy metal with large spin-orbit interaction [222, 223]. However, recently, it has been demonstrated that the interface between Co and oxide layer also effectively characterizes iDMI [224, 225]. According to this scenario, in our case, the iDMI at the Co/CoO_x interface might be modulated by the EF, resulting in the EB modulation.

5.6 Summary of this chapter

In this Chapter, we have examined the EF control of EB in the $Co/CoO_x/HfO_2$ structure where the antiferromagentic CoO_x layer was formed by natural oxidation. The modulation of the EB field was clearly observed by applying gate EF below T_B. The efficiency of the EF-induced change in EB increased near T_B. The most reasonable mechanism of the observed EB change is the modulation of the interfacial electronic structure at Co/CoO_x, in contrast to thermally-activated chemical effect in FM or AFM layer. In addition, this mechanism is fundamentally different from the conventionally-studied ME and multiferroic AFM case, indicating that this result is the first observation of the manipulation of EB by EF effect. For further understanding the microscopic origin of this effect, the investigation of the FM and AFM thickness dependences on H_{EB} and its EF effect are expected to be helpful. Although further expansion of the window of the EF-induced change in EB is required, this method might be open a new route to develop high-speed and efficient magnetization switching.

Chapter 6

Electric-field control of spin orbit torque in Co/Pd/HfO_2 system

As introduced in Chap. 4, the electric-field (EF) is a attractive tool for engineering the interfacial electronic and the chemical state as well as realizing the ultralow-power magnetization manipulation. The modification of the interfacial states may be also applicable to control other spintronic phenomena. Here, we investigated the EF control of spin-orbit torque (SOT) in the Pd/Co/Pd structure using the ALD-HfO_2 dielectric layer fabricated at 60°C. The applied EF induced an oxygen migration at the Pd/HfO_2 interface, resulting in the non-volatile change in SOT arising from both bulk spin Hall effect and interfacial effect. In particular, the contribution of the EF-induced change in interfacial SOT was suggested to be dominant in the sample with the ultrathin Pd electrode. These results indicated that controlling oxygen concentration at the Co/Pd interface was crucial for the efficient modification of SOT.

6.1 Introduction

6.1.1 Spin orbit torque

As outlined previously, the electrical control of the magnetization direction is a crucial for encoding data in spintronic memory devices. In the present spintronics industry, it is usually accomplished through the spin transfer torque (STT) effect. However, STT still needs a large current passing through the tunnel barrier, which causes some damages into memory devices. Recently, a new type of a spin torque driven by the in-plane electrical current injection via the spin-orbit interaction (SOI) has attracted attention as a more efficient current-induced magnetization manipulation method, called spin-orbit torque (SOT) (Fig. 6.1(a)). SOT magnetization switching allows us to separate the read and write paths and thus enable to avoid damages to the tunnel barrier. In recent, magnetization switching by using the combination of SOT and the EF effect on MA has been demonstrated. In a simple bilayer structure consisting of one thin ferromagnetic (FM) layer (e.g. CoFeB and Co) and one non-magnetic (NM) heavy metal layer (e.g. Pt, Ta, and W), SOTs have two components with different symmetries: damping-like (DL) SOT $\boldsymbol{\tau}_{\mathrm{DL}}$ and field-like (FL) SOT $\boldsymbol{\tau}_{\mathrm{FL}}$. The relation between two SOTs and the magnetization vector is depicted in Fig 6.1(b) and described as

$$\boldsymbol{\tau}_{\mathrm{DL}} = \gamma \boldsymbol{M} \times \boldsymbol{H}_{\mathrm{DL}} \propto \boldsymbol{M} \times \{\boldsymbol{m} \times (\hat{\boldsymbol{z}} \times \boldsymbol{j})\}, \tag{6.1}$$

$$\boldsymbol{\tau}_{\mathrm{FL}} = \gamma \boldsymbol{M} \times \boldsymbol{H}_{\mathrm{FL}} \propto \boldsymbol{M} \times (\hat{\boldsymbol{z}} \times \boldsymbol{j}), \tag{6.2}$$

where $\boldsymbol{M}$, $\boldsymbol{m}$, $\hat{\boldsymbol{z}}$, $\boldsymbol{j}$, γ and $\boldsymbol{H}_{\mathrm{DL(FL)}}$ are the magnetization vector, the magnetization unit vector ($\boldsymbol{m} = \boldsymbol{M}/|\boldsymbol{M}|$), the position unit vector along out-of-plane direction, the current unit vector ($\boldsymbol{j} = \boldsymbol{I}/|\boldsymbol{I}|$), gyromagnetic ratio, and the DL (FL) SOT effective field, respectively. $\hat{\boldsymbol{z}} \times \boldsymbol{j}$ represents the spin angular momentum unit vector which is parallel to the $\boldsymbol{\tau}_{\mathrm{DL}}$ direction in Fig. 6.1(b).

It has been generally considered that two phenomena are responsible for generating such SOT effective field: the spin Hall effect (SHE) [107] and the interfacial Rashba effect [106, 159]. The SHE is one of the spin-orbit coupling phenomena within the bulk of a heavy metal layer, where electrical currents generate transverse pure spin currents vice versa.

This effect originates from the intrinsic mechanism arising from a momentum-space Berry curvature [226] and/or two extrinsic mechanisms: the skew-scattering [227] and the side-jump mechanisms [228]. The illustration of SHE-SOT is shown in Fig. 6.1(c). Under the in-plane electrical bias, electrons with different spins separate in the NM heavy metal layer. The separated spin is injected into neighboring FM layer, and then provide a torque for the magnetic moment through the transfer of the spin angular momentum. Thus, it is suggested that the DL torque dominantly arises from the SOT generated by the SHE.

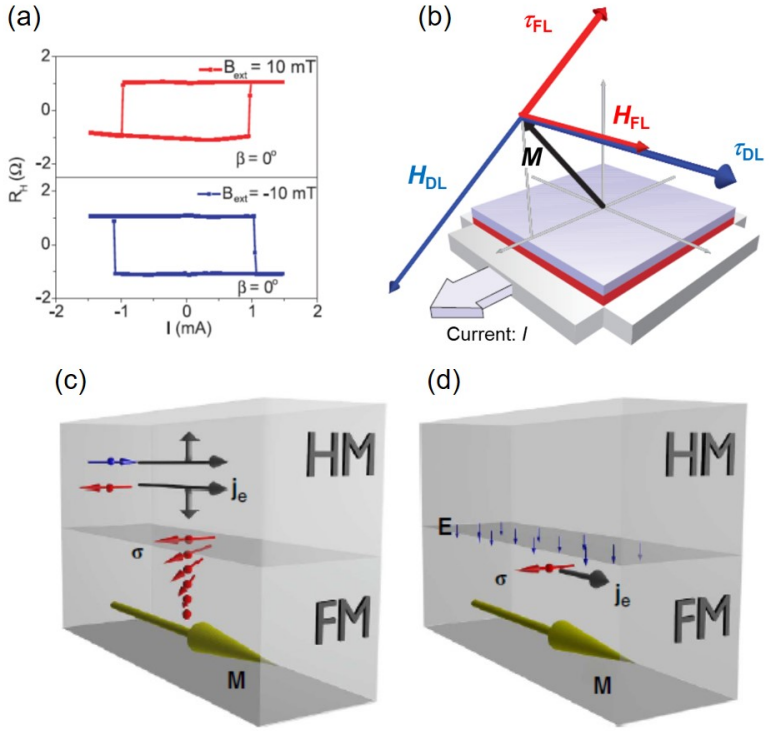

Figure 6.1: (a) The demonstration of current-induced SOT switching in a perpendicularly magnetized Ta(4)/CoFeB(1)/MgO(1.6)/Ta(1) structure at room temperature [107]. (b) Schematics of DL (FL) SOTs τ_{DL} (τ_{DL}) and SOT effective fields H_{DL} (H_{FL}) [229]. (c),(d) Schematics of two mechanism for SOT and SOT effective field: (c) Spin Hall effect and (d) Rashba effect [230].

The latter origin, the Rashba effect [156], emerges at the interface of different materials due to the large spin-orbit coupling and the structural inversion asymmetry, then resulting in the spin accumulation at the FM/NM interface. The accumulated spins can diffuse into the adjacent FM layer to exert a torque and an effective field on the magnetization through *s-d* exchange coupling (Fig. 6.1(d)). In general, the generation of FL torque is conclusively

derived from the interfacial Rashba effect [231, 232].

6.1.2 Modification of spin orbit torque by oxygen incorporation

For the application of SOT-driven devices, the improvement of the SOT efficiency is strongly required because the enhancement of SOT directly leads to the reduction of the switching current density. Therefore, various studies on the SOT phenomena have been examined to clarify the underlying origins (the SHE or the Rashba effect) and increase the efficiency. One way to enhance the SOT efficiency is the oxidation of the FM or NM layer [106, 138, 172, 233, 234]. The importance of the oxidation at the FM surface has been pointed out since the beginning of SOT research [106]. As shown in Fig. 6.2(a), our group has confirmed that both the DL and FL torques in surface-oxidized Pt/Co systems (Sample O) were enhanced compared to those of non-oxidized systems (Sample UO) [172]. Further, inserting the oxide layer at the Co/Pt interface increases the efficiency of SOT more (Fig. 6.2(b)) [138]. The enhancement ratio of the FL torque is much larger than that of the DL torque in Co/CoO_x/Pt system (IO sample). These research claimed that the FM/NM interface is considered to be mainly responsible for the modulation of the interfacial Rashba effect by the oxide insertion. In recent, voltage-controlled SOT via magneto-ionic control of oxygen migration was demonstrated [235–237].

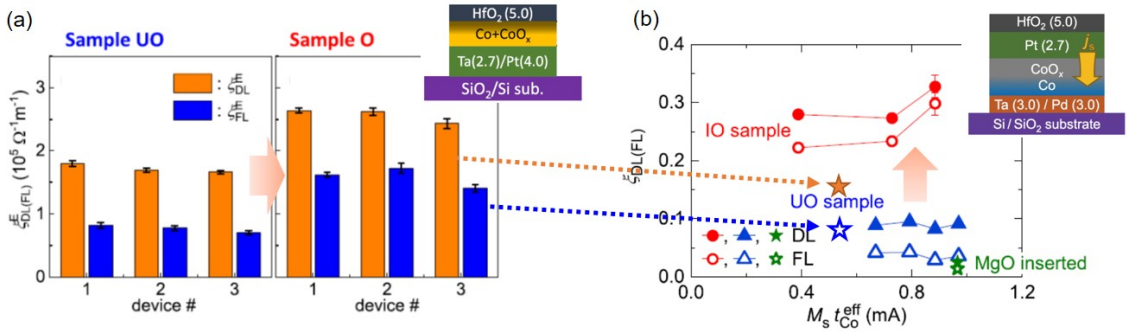

Figure 6.2: (a) The SOT efficiencies per unit electric field for three similar devices made from the sample UO and O. The layer structure of the sample O is also shown in the figure [172]. (b) The SOT efficiencies for the IO and UO samples as a function of the areal magnetic moment. The results for the Co/MgO(0.8)/Pt sample (green star symbol), Pt/Co/MgO (blue star symbol: sample UO in Fig. 6.2(a)) sample, and Pt/Co+CoO_x (orange star symbol: sample O in Fig. 6.2(a)) reproduced from ref. [172] are also shown [138].

In these studies, a large spin-orbit coupling NM layer, such as Pt was used. Thus, the spin current generated by the bulk SHE mainly affect the SOT effect. In this study, to suppress the SHE contribution, we examined the SOT effect in Pd/Co/Pd structure. Note that it has been considered that the contribution of a spin current from Pd layer is much smaller, compared to Pt layer [238]. We also investigated the role of oxygen ion on SHE-induced and Rashba-induced SOT by EF-induced redox effect using 60°C-ALD-fabricated HfO_2 dielectric.

6.2 Sample fabrication

The illustration of the sample structure is shown in Fig. 6.3. From the substrate side, Ta(2.0)/Pd(3.1)/Co(2.2)/Pd(t_{Pd}) was deposited on semi-insulating GaAs(001) substrate using rf magnetron sputtering at room temperature under Xe gas with a pressure of 0.2 Pa. The samples were patterned into a Hall bar structure by photolithography and Ar ion milling. The etching time was 130 s. Then, electrodes and contact pads made of Cr(2)/Cu(50)/Au(10) were formed at the end of the Hall cross by photolithography and lift-off. Both the width of the channel and the Hall probe of the Hall devices were 10-μm. After photoresist was only covered on contact pads by photolithography, 50-nm-thick HfO_2 insulating layer was deposited in ALD chamber at 60°C under ~0.3 Torr N_2 condition. Finally, Cr(2)/Cu(40)/Au(10) gate electrode was formed by resistance heating evaporation and lift-off.

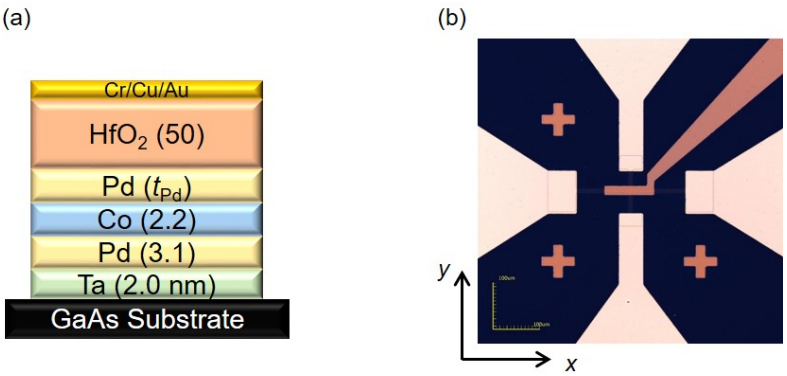

Figure 6.3: (a) The schematics of Pd/Co/Pd/HfO_2 capacitor structure studied in this chapter. (b) The optical image of the Hall device. The experimental set-up for the harmonic Hall measurement is depicted in the image.

6.3 Electric-field induced magneto-ionic effect on SOT effective field

6.3.1 Ac Hall measurement

For the quantitative SOT determination, we performed the harmonic Hall voltage measurement by injecting an in-plane ac current [239, 240]. The ac electric current I was applied to the source-drain path at the frequency f of 13.14 Hz using an ac current source meter (Keithley 6221). Positive current is defined as current flowing along $+x$ direction in Fig. 6.3(b). Then, the in-phase first and out-of-phase second harmonic Hall voltages, $V^{\omega}_{\mathrm{Hall}}$ and $V^{2\omega}_{\mathrm{Hall}}$ respectively, were measured using a lock-in amplifier (Stanford Research Systems, Model SR830) while the external magnetic field H was rotated in the xy plane from $\varphi = 0°$ to 360°. The magnetization is assumed to be uniform during the harmonic Hall measurement. All transport measurements were performed at room temperature.

The first and second harmonic Hall resistances ($R^{\omega}_{\mathrm{Hall}} \equiv V^{\omega}_{\mathrm{Hall}}/I$, $R^{2\omega}_{\mathrm{Hall}} \equiv V^{2\omega}_{\mathrm{Hall}}/I$) are described as

$$R^{\omega}_{\mathrm{Hall}} = R_{\mathrm{AHE}} \cos\theta + R_{\mathrm{PHE}} \sin 2\varphi, \tag{6.3}$$

$$R^{2\omega}_{\mathrm{Hall}} = -(R_{\mathrm{DL}} + R_{\mathrm{ANE}}) \cos\varphi - R_{\mathrm{FL}}(\cos 3\varphi + \cos\varphi), \tag{6.4}$$

where R_{AHE}, R_{PHE}, R_{DL}, R_{FL}, and R_{ANE} are the anomalous Hall resistance, the planer Hall resistance, DL, FL and the anomalous Nernst thermal contributions to the second harmonic transverse resistances, respectively. Further, R_{DL}, R_{FL}, and R_{ANE} follow the relation;

$$R_{\mathrm{DL}} = \frac{1}{2}\frac{R_{\mathrm{AHE}} H_{\mathrm{DL}}}{H + H_{\mathrm{k}}}, \tag{6.5}$$

$$R_{\mathrm{FL}} = \frac{1}{2}\frac{R_{\mathrm{PHE}}(H_{\mathrm{FL}} + H_{\mathrm{Oe}})}{H}, \tag{6.6}$$

$$R_{\mathrm{ANE}} = -\alpha w M_{\mathrm{s}} \frac{\nabla T_z}{I}, \tag{6.7}$$

where H_{Oe}, H_{k}, α, w, and ∇T_z are the Oersted field, the anisotropy field, the anomalous Nernst coefficient, the channel width, and the out-of-plane temperature gradient. The typical

φ dependence of $R^{\omega}_{\mathrm{Hall}}$ and $R^{2\omega}_{\mathrm{Hall}}$ are shown in Fig. 6.4(a) and (b). R_{PHE} is estimated by the fitting to $R^{\omega}_{\mathrm{Hall}}$ which shows no H dependence (eq. 6.3) and the result of the fitting to $R^{2\omega}_{\mathrm{Hall}}$ using eq. 6.4 provides us to the value of $R_{\mathrm{DL}} + R_{\mathrm{ANE}}$ and R_{FL} (Fig. 6.4(c) and (d)). As shown in eqs. 6.5 and 6.6, the resistance derived from the SOT effect depends on the magnitude of H. Thus, we can evaluate H_{DL} and $H_{\mathrm{FL}} + H_{\mathrm{Oe}}$ from the slope of the linear fitting to $(R_{\mathrm{DL}} + R_{\mathrm{ANE}})$-$[\mu_0(H + H_{\mathrm{k}})^{-1}]$ plot and R_{FL}-$(\mu_0 H)^{-1}$ plot. H_{Oe} is calculated as $\mu_0 H_{\mathrm{Oe}} = \mu_0 j_{\mathrm{NM}} t_{\mathrm{NM}}/2$, where j_{NM} and t_{NM} are the current density in the NM layer and the NM layer thickness, respectively.

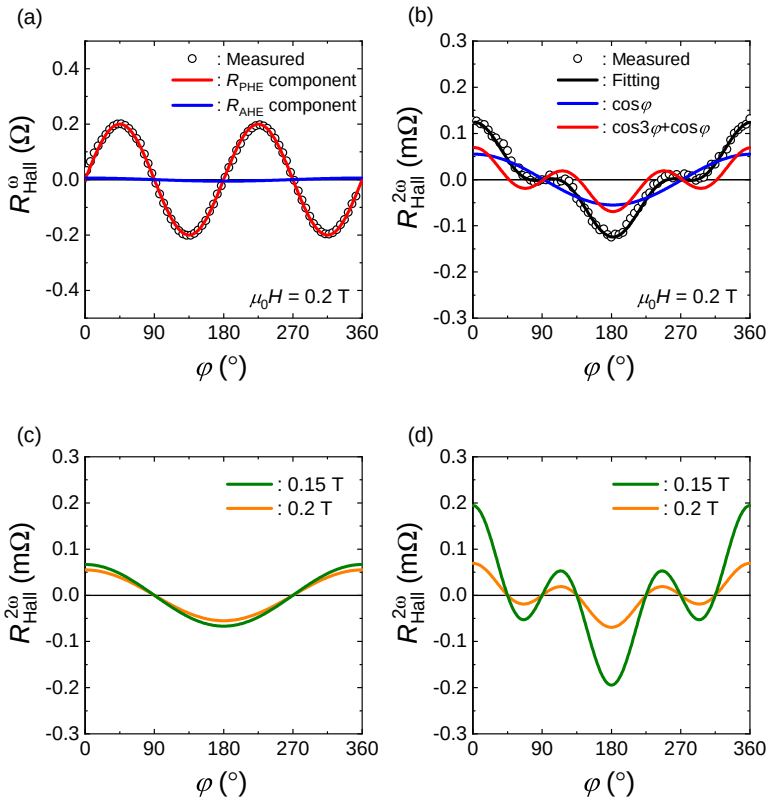

Figure 6.4: (a) φ dependence of $R^{\omega}_{\mathrm{Hall}}$. (b) φ dependence of $R^{2\omega}_{\mathrm{Hall}}$ for the in-plane magnetic field of 0.15 T and 0.2 T. (c) The cos φ component of $R^{2\omega}_{\mathrm{Hall}}$. (d) The cos $3\varphi + \cos\varphi$ component of $R^{2\omega}_{\mathrm{Hall}}$.

We take a look at the result of the EF modulation of the SOT effective fields for our Pd(3.1)/Co(2.2)/Pd(t_{Pd})/HfO_2 samples. V_{G}s were applied to two similar devices in the following order:

- Sample 1: 0 V→ +10 V for 600 s → 0 V,
- Sample 2: 0 V→ −10 V for 600 s → 0 V.

We should note that there is no difference in any magnetic properties, including SOT effective fields, between two samples. Each transport measurement was carried out at $V_G = 0$ V before and after applying V_G. Fig. 6.5(a) shows $R_{Hall}^{2\omega}$ of the Pd(3.1)/Co(2.2)/Pd(0.52) sample measured under the in-plane magnetic field of 0.2 T before (0 V) and after gating treatments (+10 V and −10 V). $V_G = \pm 10$ V corresponds $E_G = \pm 2$ MV/cm. The distinct change in $R_{Hall}^{2\omega}$ was obtained by V_G applications. $\cos\varphi$ component decreased (increased) by the positive (negative) V_G application (Fig. 6.5(b)), while the component of $\cos 3\varphi + \cos\varphi$ increased (decreased) (Fig. 6.5(c)). Figs. 6.6(a) and (b) shows $(H + H_k)^{-1}$ dependence of $R_{DL} + R_{ANE}$ and H^{-1} dependence of R_{FL}, respectively. $\mu_0 H_k$ was measured by dc Hall measurement under the perpendicular magnetic field $\mu_0 H_\perp$ and a dc current of 50 μA was applied along sample channel. The reduction (enhancement) of PMA was obtained after applying the positive (negative) V_G (see in Figs. 6.7(a) and (b)). All data can be definitely fitted to the linear function. The deviation from the origin of coordinates in R_{FL} graph may be due to a finite misalignment of the sample position. We calculated the SOT effecitive field by applying eqs. 6.5 and 6.6 with the values of R_{PHE} and R_{AHE} (Fig. 6.7(c)).

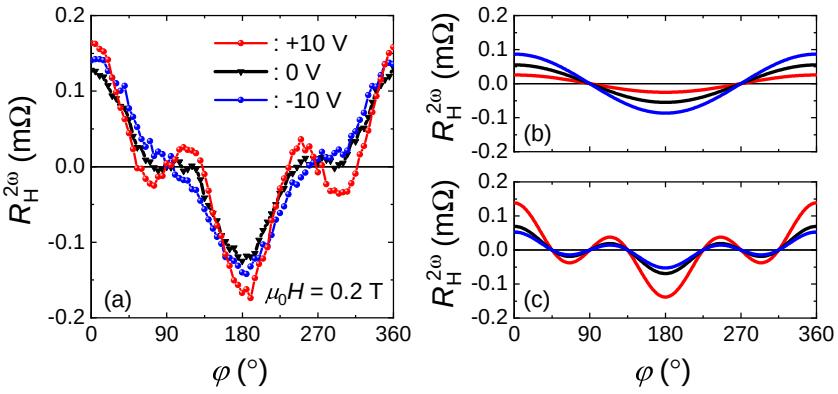

Figure 6.5: (a) $R_{Hall}^{2\omega}$ of Pd(3.1)/Co(2.2)/Pd(0.52) sample measured under the in-plane magnetic field of 0.2 T before gating (0 V) and after gating (+10 V and −10 V) (b) $\cos\varphi$ component. (c) $\cos 3\varphi + \cos\varphi$ component.

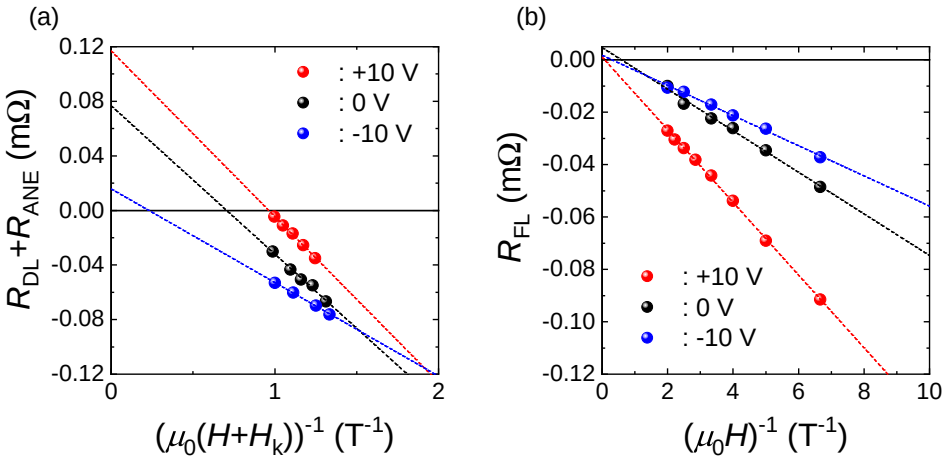

Figure 6.6: The external magnetic field dependence of (a) R_{DL} + R_{ANE} and (b) R_{FL}.

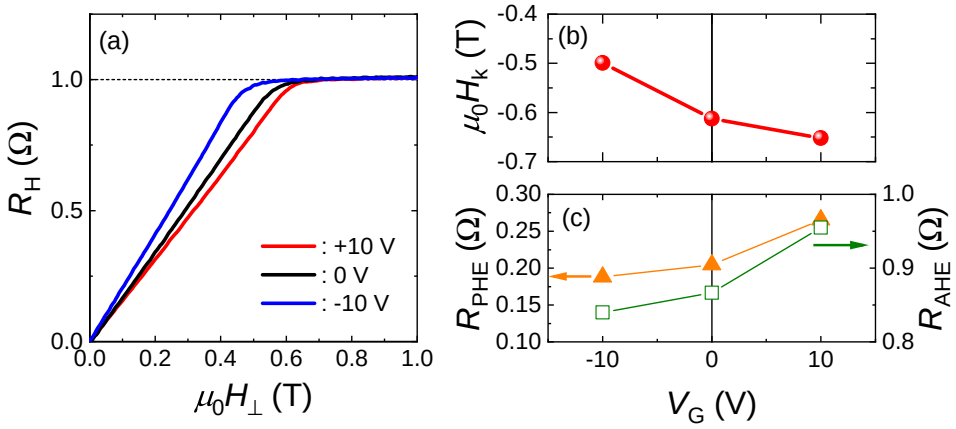

Figure 6.7: (a) Normalized R_{Hall} curves for each gate voltage application measured by sweeping out-of-plane magnetic field. (b) V_G dependence of $\mu_0 H_k$. (c) V_G dependence of R_{PHE} and R_{AHE}. R_{AHE} values were quantified by each R_{Hall} curve.

Figs. 6.8(a) and (b) present V_G dependence of $\mu_0 H_{DL}$ and $\mu_0(H_{FL} + H_{Oe})$ for the Pd(3.1)/Co(2.2)/Pd(0.52) sample, respectively. A large change in $\mu_0 H_{DL}$ was observed by applying $V_G = -10$ V, whereas the value of $\mu_0 H_{DL}$ at $V_G = +10$ V was almost the same value as $V_G = 0$ V. In contrast, $\mu_0(H_{FL} + H_{Oe})$ monotonically decreased (increased) at the positive (negative) V_G. We conducted the same SOT measurement for the Pd(3.1)/Co(2.2)/Pd(1.03) sample, which has thicker Pd electrode. Figs. 6.9(a) and (b) show V_G dependence of $\mu_0 H_{DL}$

and $\mu_0(H_{FL}+H_{Oe})$ for the Pd(3.1)/Co(2.2)/Pd(1.03) sample. Both $\mu_0 H_{DL}$ and $\mu_0(H_{FL}+H_{Oe})$ values monotonically increased (decreased) by the application of the positive (negative) V_G. We found that the sign of the EF modulation of the SOT effective field was different between the thin Pd sample and the thick Pd sample.

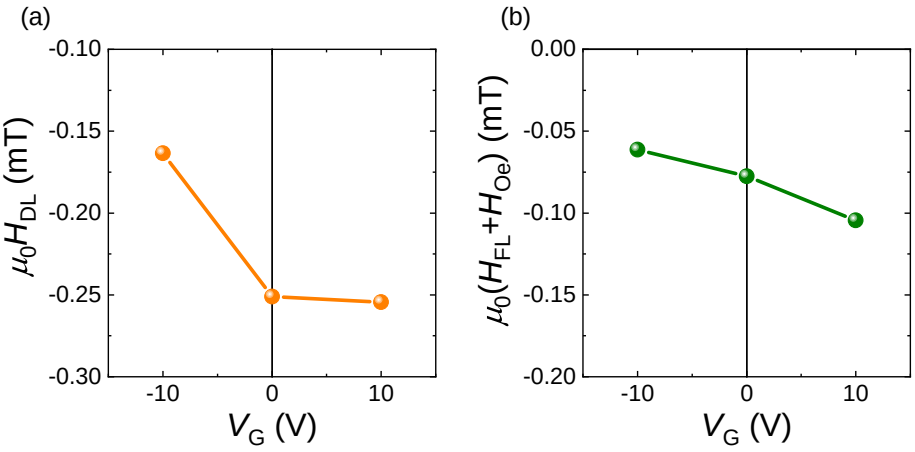

Figure 6.8: V_G dependence of (a) $\mu_0 H_{DL}$ and (b) $\mu_0(H_{FL}+H_{Oe})$ for the Pd(3.1)/Co(2.2)/Pd(0.52) sample.

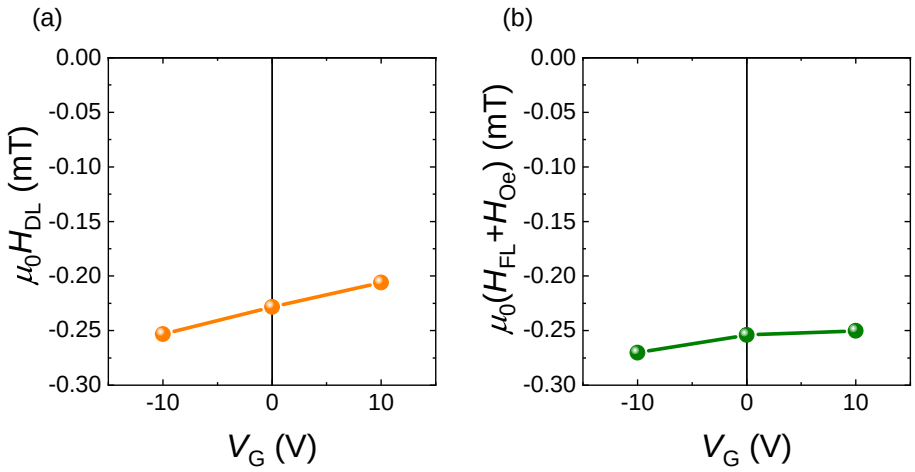

Figure 6.9: V_G dependence of (a) $\mu_0 H_{DL}$ and (b) $\mu_0(H_{FL}+H_{Oe})$ for the Pd(3.1)/Co(2.2)/Pd(1.03) sample.

6.3.2 Discussion

To estimate the contribution of the SHE, we evaluated the resistivity of each layer by measuring the longitudinal resistance of various samples: the Ta(2)/MgO(2), Ta(2)/Co(2.2)/MgO(2), and Ta(2)/Pd(t_{Pd})/MgO(2) samples. All stacks were deposited on a semi-insulating GaAs substrate. After the deposition and the device fabrication, samples were baked at 60°C for 90 min in the ALD chamber. To measure 4-wire resistance, a dc current of 50 μA was applied to the sample channel whose width and length are 30 μm and 50 μm, respectively. Table 6.1 shows the resistivity ρ and the sheet resistance R_{sheet} of Ta(2 nm), Co(2.2 nm), Pd(3.1 nm), Pd(1.03 nm), and Pd(0.52 nm). In addition, we estimated the thickness of the naturally-oxidized Pd layer and the voltage-induced change in t_{Pd}. Fig. 6.10(a) presents the t_{Pd} dependence of the Pd R_{sheet} ($R^{\mathrm{Pd}}_{\mathrm{sheet}}$) for non-oxidized Ta(2)/Pd(t_{Pd})/MgO(2) samples. We assume that the Pd resistivity is constant in this t_{Pd} range. Fig. 6.10(b) shows the value of $R^{\mathrm{Pd}}_{\mathrm{sheet}}$ at each V_{G} treatment for the sample made of Ta(2)/Pd(1.03)/HfO_2(50)/Ta/Pt. The $R^{\mathrm{Pd}}_{\mathrm{sheet}}$ decreased (increased) as the positive (negative) V_{G} was applied, indicating that the Pd layer was reduced (oxidized) by the positive (negative) V_{G} application. The reduction of the metallic Pd thickness caused by the natural oxidation was estimated to be 0.05 nm. Furthermore, the voltage-induced change in t_{Pd} was about ±0.1 nm by the application of ±10 V for 600 s.

Considering the shunting, the +10 V (−10 V) application would reduce (enhance) the contribution of the SHE from the bottom Pd layer. Therefore, if there was only the contribution of the SHE in the Pd/Co/Pd/HfO_2 system, the amount of H_{DL} will decrease (increase). This tendency was consistent with the Pd(1.03) sample, but opposite to the case of the Pd(0.52) sample. One possible explanation of this difference is EF modification of the interfacial SOT contribution, such as the Rashba-driven SOT. Injected oxygen ions by the natural oxidation is suggested to be located near the Co/Pd(0.52) interface, compared to the Co/Pd(1.03) sample. The negative V_{G} pushed up the oxygen ions closer to the Co/Pd interface, resulting that the change in interfacial SOT exceeded that in SHE-driven SOT. The difference on the sign of the EF-induced change in the H_{FL} + H_{Oe} component may be attributable to the same mechanism because the change in H_{Oe} is consider to be little.

Material	ρ [$\mu\Omega \cdot$ m]	R_{sheet} [Ω]
Ta(2 nm)	4.37	2519
Co(2.2 nm)	0.811	369
Pd(3.1/1.03/0.52 nm)	0.63	245/1541/1794

Table 6.1: The resistivity ρ and the sheet resistance R_{sheet} of each material.

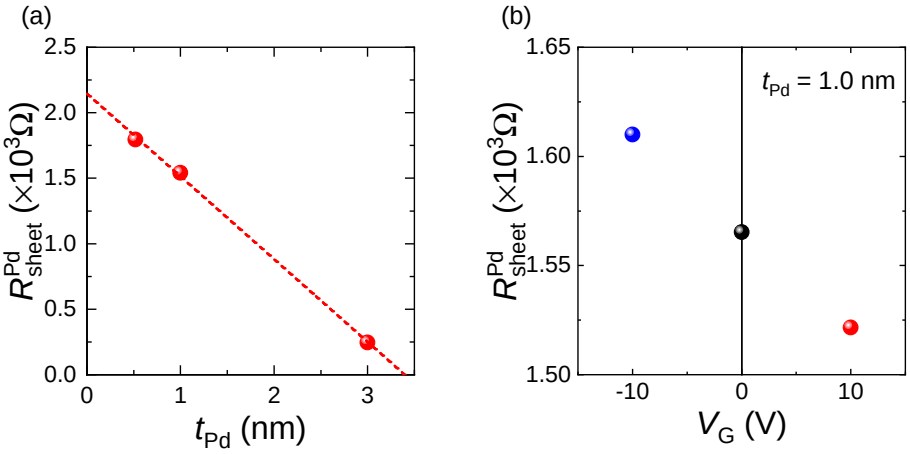

Figure 6.10: (a) t_{Pd} dependence of $R^{\mathrm{Pd}}_{\mathrm{sheet}}$. (b) V_{G} dependence of $R^{\mathrm{Pd}}_{\mathrm{sheet}}$.

6.4 Summary of this chapter

We have demonstrated the large and non-volatile modification of SOTs by using voltage-driven oxygen incorporation at the Pd/HfO_2 interface using a glow temperature ALD-fabricated HfO_2 insulator. The EF change in the SOT magnitude was estimated by harmonic Hall voltage measurements with ac electrical in-plane current injection. In the sample with the thick Pd electrode, the sign of the EF modulation of the DL SOT effective field can be explained by the change in the injected spin current from top and bottom Pd layers caused by the voltage-induced change in the Pd thickness. On the other hand, in the sample with the approximately 2 ML Pd electrode, the peculiar EF-change in the DL SOT effective field was obtained. These results imply that the EF modification of the interfacial spin-orbit phenomena dominantly contributes SOT. For further investigation of the interfacial SOT, the systematic top Pd thickness dependence should be needed. The oxidation of Pd and its non-volatile EF control is a significant step toward not only understanding the SOT description but also improving the SOT-based spintronic devices.

Chapter 7

Summary

7.1 Conclusion

In this thesis, we have examined the controls of magnetism by applying a gate electric-field (EF) and engineering an interfacial state in ultrathin transition metal/oxide stacked structures. By focusing on not only $3d$-ferromagnet/MgO system but also the interface comprised of $4d$ and $5d$ transition metal electrodes and several oxide dielectrics, we have demonstrated unprecedented EF control of magnetism. The following achievements would accelerate the research on the EF control of spintronic phenomena.

Electric-field control of magnetic anisotropy in Pt/Oxide system

In Chap. 3, we have investigated the EF control of the magnetic anisotropy (MA) in the $5d$-Pt/oxide structures. The efficiency of the EF-induced change in the perpendicular MA (PMA) energy β_S depends on the temperature and the Pt thickness, which is significantly different from the case of the conventional $3d$-transition metal/MgO systems. We have found the proximity-induced orbital magnetic moment in Pt atoms shows the similar relation with the temperature to β_S by means of the x-ray absorption spectroscopy and the x-ray circular dichroism (XMCD) measurement. In addition, we have found that the PMA energy and its EF effect strongly depend on the adjacent oxide materials rather than the capacitance value. The magnetic moments in Pt atoms, quantified by the XMCD spectroscopy, have confirmed that the oxide materials have a great impact on the electronic state at the Pt surface. Furthermore,

we have revealed that the effective PMA mediated by the Rashba spin-orbit coupling exists at the Pt/oxide interface and it would be modulated by changing the interfacial oxide.

Electric-field control of magnetic anisotropy and phase transition in Co/HfO_2 system

In Chap. 4, we have investigated the control of the MA and the magnetic phase transition in the naturally-oxidized Co electrode by applying the gate EF through the ALD-fabricated HfO_2 dielectric layer. Comparing the results for two samples with HfO_2 formed under different temperature: 150°C (optimal) and 60°C (low temperature) using the anomalous Hall effect, the SQUID magnetization measurement, and the capacitance measurement, we have found that changing the ALD fabrication condition dramatically causes the quality of HfO_2, resulting in the determination of the mechanism of the EF effect on magnetism. In addition, we have realized the enhancement of β_S, which is originated from a purely electronic mechanism, only by treating a surface oxidation of Co layer.

Electric-field control of exchange bias in Co/HfO_2 system

In Chap. 5, we have investigated the EF control of the exchange bias (EB) effect in the naturally-oxidized Co/HfO_2 system. After the field cooling was performed, the hysteresis loop shift that had not been observed at 300 K can be clearly obtained by the anomalous Hall measurement, indicating that the EB effect is induced by the interfacial exchange coupling between spins in the ferromagnetic Co layer and naturally-oxidized antiferromagnetic CoO_x layer. Both the coercivity and the EB field are monotonically and reversibly change by applying the gate EF. We have confirmed that there is no magneto-electric effect in CoO_x and no voltage-driven redox reaction, thus concluded that the observed EB change is attributable to the EF modification of the interfacial electronic state at the Co/CoO_x interface.

Electric-field control of spin orbit torque in $Co/Pd/HfO_2$ system

In Chap. 6, we have investigated the EF control of spin-orbit torque (SOT) in the Pd/Co/Pd system using the magneto-ionic solid-state dielectric HfO_2 at room temperature. The clear

changes in the SOT effective fields have been observed by the EF-induced incorporation of oxygen ions into the Pd electrode. In addition, we have found that the interfacial SOT contribution may be dominantly modulated by promoting the oxygen migration near the Co/Pd interface by measuring SOT for the two samples with the different Pd thickness.

7.2 Future prospect

We have demonstrated the dramatic enhancement of the EF-induced modulation of the PMA energy in the Pt/oxide system and the EF-induced EB change in Co/CoO_x system only at low temperature. For the realization of the efficient EF effect on magnetism near room temperature, utilizing the lattice strain is supposed to be effective. One of the promising way to introduce an intentional internal strain into the microfabricated magnetic capacitor is to utilize a flexible substrate, such as a polyethylene terephthalate (PET) substrate. The thickness of a flexible substrate is below 50 μm, enabling us to apply one order of magnitude of larger tensile stress to thin films compared to a conventional piezo transducer. Actually, we have demonstrated the fabrication of a field-effect capacitor with an ALD-grown HfO_2 dielectric and an MgO-based magnetic tunnel junction device on an organic flexible substrate [95, 132]. Thus, by tuning the amount of strain in the capacitor structures, we enable the systematic studies on the strain dependence of the EF effect on magnetism and the enhancement of the EF effect might be possible. In addition, we need to work on the experimental and theoretical studies on the pure EF modification of the Rashba-driven MA and iDMI as a new pathway to improve the EF effect on magnetism.

Moreover, our findings would realize the EF control of other spintronic phenomena (e.g. spin-orbit transport or spin caloritronics phenomena). In fact, the reversible EF switching of the anomalous Ettingshausen effect, the interconversion between the electrical charge current and the heat current in ferromagnets, for the ultrathin Co film using the low temperature ALD-fabricated HfO_2 has reported [173]. Such advances would open a new window of the field-effect spintronics devices.

Bibliography

[1] M. N. Baibich, J. M. Broto, A. Fert, F. N. Van Dau, F. Petroff, P. Eitenne, G. Creuzet, A. Friederich, and J. Chazelas, Phys. Rev. Lett. **61**, 2472 (1988).

[2] G. Binasch, P. Grunberg, F. Saurenbach, and W. Zinn, Phys. Rev. B **39**, 4828 (1989).

[3] H. Ohno, D. Chiba, F. Matsukura, T. Omiya, E. Abe, T. Dietl, Y. Ohno, and K. Ohtani, Nature **408**, 944 (2000).

[4] F. Matsukura, Y. Tokura, and H. Ohno, Nat. Nanotechnol. **10**, 209 (2015).

[5] S. Miwa, M. Suzuki, M. Tsujikawa, T. Nozaki, T. Nakamura, M. Shirai, S. Yuasa, and Y. Suzuki, J. Phys. D. Appl. Phys. **164**, 162 (2018).

[6] T. Nozaki, T. Yamamoto, S. Miwa, M. Tsujikawa, M. Shirai, S. Yuasa, and Y. Suzuki, Micromachines **10**, 327 (2019).

[7] J. E. Lilienfeld, U. S. Patent No. 1745175 (1925).

[8] D. Kahng, U. S. Patent No. 3102230 (1963).

[9] M. Nakano, K. Shibuya, D. Okuyama, T. Hatano, S. Ono, M. Kawasaki, Y. Iwasa, and Y. Tokura, Nature **487**, 459 (2012).

[10] K. Ueno, S. Nakamura, H. Shimotani, A. Ohtomo, N. Kimura, T. Nojima, H. Aoki, Y. Iwasa, and M. Kawasaki, Nat. Mater. **7**, 855 (2008).

[11] K. Ueno, S. Nakamura, H. Shimotani, H. T. Yuan, N. Kimura, T. Nojima, H. Aoki, Y. Iwasa, and M. Kawasaki, Nat. Nanotechnol. **6**, 408 (2011).

[12] H. Ohno, J. Magn. Magn. Mater. **200**, 110 (1999).

[13] T. Dietl, H. Ohno, F. Matsukura, J. Cibert, and D. Ferrand, Science **287**, 1019 (2000).

[14] S. Souma, L. Chen, R. Oszwałdowski, T. Sato, F. Matsukura, T. Dietl, H. Ohno, and T. Takahashi, Sci. Rep. **6**, 27266 (2016).

[15] D. Chiba, M. Yamanouchi, F. Matsukura, and H. Ohno, Science **301**, 943 (2003).

[16] H. Ohno, A. Shen, F. Matsukura, A. Oiwa, A. Endo, S. Katsumoto, and Y. Iye, Appl. Phys. Lett. **69**, 363 (1996).

[17] D. Chiba, F. Matsukura, and H. Ohno, Appl. Phys. Lett. **89**, 162505 (2006).

[18] M. Sawicki, D. Chiba, A. Korbecka, Y. Nishitani, J. A. Majewski, F. Matsukura, T. Dietl, and H. Ohno, Nat. Phys. **6**, 22 (2009).

[19] D. Chiba, M. Sawicki, Y. Nishitani, Y. Nakatani, F. Matsukura, and H. Ohno, Nature **455**, 515 (2008).

[20] L. Chen, S. Yan, P. F. Xu, J. Lu, W. Z. Wang, J. J. Deng, X. Qian, Y. Ji, and J. H. Zhao, Appl. Phys. Lett. **95**, 182505 (2009).

[21] Y. Yamada, K. Ueno, T. Fukumura, H. T. Yuan, H. Shimotani, Y. Iwasa, L. Gu, S. Tsukimoto, Y. Ikuhara, and M. Kawasaki, Science **332**, 1065 (2011).

[22] M. Weisheit, S. Fähler, A. Marty, Y. Souche, C. Poinsignon, and D. Givord, Science **315**, 349 (2007).

[23] T. Maruyama, Y. Shiota, T. Nozaki, K. Ohta, N. Toda, M. Mizuguchi, A. A. Tulapurkar, T. Shinjo, M. Shiraishi, S. Mizukami, Y. Ando, and Y. Suzuki, Nat. Nanotechnol. **4**, 158 (2009).

[24] D. Chiba, S. Fukami, K. Shimamura, N. Ishiwata, K. Kobayashi, and T. Ono, Nat. Mater. **10**, 853 (2011).

[25] P. F. Carcia, J. Appl. Phys. **63**, 5066 (1988).

[26] T. Koyama, A. Obinata, Y. Hibino, A. Hirohata, B. Kuerbanjiang, V. K. Lazarov, and D. Chiba, Appl. Phys. Lett. **106**, 132409 (2015).

[27] T. Hirai, T. Koyama, A. Obinata, Y. Hibino, K. Miwa, S. Ono, M. Kohda, and D. Chiba, Appl. Phys. Express **9**, 063007 (2016).

[28] K. Shimamura, D. Chiba, S. Ono, S. Fukami, N. Ishiwata, M. Kawaguchi, K. Kobayashi, and T. Ono, Appl. Phys. Lett. **100**, 122402 (2012).

[29] C. Takahashi, M. Ogura, and H. Akai, J. Phys. Condens. Matter **19**, 365233 (2007).

[30] M. Kawaguchi, K. Shimamura, S. Ono, S. Fukami, F. Matsukura, H. Ohno, D. Chiba, and T. Ono, Appl. Phys. Express **5**, 063007 (2012).

[31] A. Obinata, Y. Hibino, D. Hayakawa, T. Koyama, K. Miwa, S. Ono, and D. Chiba, Sci. Rep. **5**, 14303 (2015).

[32] A. Obinata, T. Hirai, Y. Kotani, K. Toyoki, T. Nakamura, T. Koyama, A. Obinata, T. Hirai, Y. Kotani, and K. Toyoki, AIP Adv. **8**, 115122 (2018).

[33] F. Ando, H. Kakizakai, T. Koyama, K. Yamada, M. Kawaguchi, S. Kim, K.-J. Kim, T. Moriyama, D. Chiba, and T. Ono, Appl. Phys. Lett. **109**, 022401 (2016).

[34] A. L. Sukstanskii and K. I. Primak, Phys. Solid State **45**, 109 (2003).

[35] J. Dyson, Phys. Rev. **102**, 1230 (1956).

[36] F. Ando, K. T. Yamada, T. Koyama, M. Ishibashi, Y. Shiota, T. Moriyama, D. Chiba, and T. Ono, Appl. Phys. Express **11**, 073002 (2018).

[37] T. Dohi, S. Kanai, A. Okada, F. Matsukura, and H. Ohno, AIP Adv. **6**, 075017 (2016).

[38] T. Dohi, S. Kanai, F. Matsukura, and H. Ohno, Appl. Phys. Lett. **111**, 072403 (2017).

[39] J. Cho, S. Miwa, K. Yakushiji, H. Kubota, A. Fukushima, C. Y. You, S. Yuasa, and Y. Suzuki, Phys. Rev. Appl. **10**, 014033 (2018).

[40] K. Nawaoka, S. Miwa, Y. Shiota, N. Mizuochi, and Y. Suzuki, Appl. Phys. Express **8**, 063004 (2015).

[41] T. Koyama, Y. Nakatani, J. Ieda, and D. Chiba, Sci. Adv. **4**, eaav0265 (2018).

[42] S. Kasukawa, Y. Shiota, T. Moriyama, and T. Ono, Jpn. J. Appl. Phys. **57**, 080309 (2018).

[43] J. Suwardy, K. Nawaoka, J. Cho, M. Goto, Y. Suzuki, and S. Miwa, Phys. Rev. B **98**, 144432 (2018).

[44] J. Suwardy, M. Goto, Y. Suzuki, and S. Miwa, Jpn. J. Appl. Phys. **58**, 060917 (2019).

[45] I. Dzyaloshinsky, J. Phys. Chem. Solids **4**, 241 (1958).

[46] T. Moriya, Phys. Rev. Lett. **4**, 228 (1960).

[47] T. Moriya, Phys. Rev. **120**, 91 (1960).

[48] A. Fert and P. M. Levy, Phys. Rev. Lett. **44**, 1538 (1980).

[49] A. Thiaville, S. Rohart, É. Jué, V. Cros, and A. Fert, Eur. Lett. **100**, 57002 (2012).

[50] A. Fert, V. Cros, and J. Sampaio, Nat. Nanotechnol. **8**, 152 (2013).

[51] J.-H. Moon, S.-M. Seo, K.-J. Lee, K.-W. Kim, J. Ryu, H.-W. Lee, R. D. Mcmichael, and M. D. Stiles, Phys. Rev. B **88**, 184404 (2013).

[52] C. Bi, Y. Liu, T. Newhouse-Illige, M. Xu, M. Rosales, J. W. Freeland, O. Mryasov, S. Zhang, S. G. E. Te Velthuis, and W. G. Wang, Phys. Rev. Lett. **113**, 267202 (2014).

[53] U. Bauer, L. Yao, A. J. Tan, P. Agrawal, S. Emori, H. L. Tuller, S. V. Dijken, and G. S. D. Beach, Nat. Mater. **14**, 174 (2015).

[54] C. G. Duan, J. P. Velev, R. F. Sabirianov, Z. Zhu, J. Chu, S. S. Jaswal, and E. Y. Tsymbal, Phys. Rev. Lett. **101**, 137201 (2008).

[55] K. Nakamura, R. Shimabukuro, Y. Fujiwara, T. Akiyama, T. Ito, and A. J. Freeman, Phys. Rev. Lett. **102**, 187201 (2009).

[56] M. Tsujikawa and T. Oda, Phys. Rev. Lett. **102**, 247203 (2009).

[57] M. Oba, K. Nakamura, T. Akiyama, T. Ito, M. Weinert, and a. J. Freeman, Phys. Rev. Lett. **114**, 107202 (2015).

[58] K. T. Yamada, M. Suzuki, A.-M. Pradipto, T. Koyama, S. Kim, K.-J. Kim, S. Ono, T. Taniguchi, H. Mizuno, F. Ando, K. Oda, H. Kakizakai, T. Moriyama, K. Nakamura, D. Chiba, and T. Ono, Phys. Rev. Lett. **120**, 157203 (2018).

[59] K. Nakamura, T. Akiyama, T. Ito, M. Weinert, and A. J. Freeman, Phys. Rev. B **81**, 220409 (2010).

[60] F. Ibrahim, H. X. Yang, A. Hallal, B. Dieny, and M. Chshiev, Phys. Rev. B **93**, 014429 (2016).

[61] C. Liu, E. R. Moog, and S. D. Bader, Phys. Rev. Lett. **60**, 2422 (1988).

[62] H. X. Yang, M. Chshiev, B. Dieny, J. H. Lee, A. Manchon, and K. H. Shin, Phys. Rev. B **84**, 054401 (2011).

[63] G. H. O. Daalderop, P. J. Kelly, and F. J. a. Den Broeder, Phys. Rev. Lett. **68**, 682 (1992).

[64] D.-S. Wang, R. Wu, and A. J. Freeman, Phys. Rev. B **48**, 15886 (1993).

[65] N. Nakajima, T. Koide, T. Shidara, H. Miyauchi, H. Fukutani, A. Fujimori, K. Iio, T. Katayama, M. Nývlt, and Y. Suzuki, Phys. Rev. Lett. **81**, 5229 (1998).

[66] C. Chappert and P. Bruno, J. Appl. Phys. **64**, 5736 (1988).

[67] P. Bruno, J. Appl. Phys. **64**, 3153 (1988).

[68] B. T. Thole, P. Carra, F. Sette, and G. Van Der Laan, Phys. Rev. Lett. **68**, 1943 (1992).

[69] P. Carra, B. T. Thole, M. Altarelli, and X. Wang, Phys. Rev. Lett. **70**, 694 (1993).

[70] J. Stöhr and H. König, Phys. Rev. Lett. **75**, 3748 (1995).

[71] A. J. Silenko, J. Phys. B At. Mol. Opt. Phys. **25**, 1661 (1992).

[72] J. Stöhr, J. Magn. Magn. Mater. **200**, 470 (1999).

[73] Y. Suzuki and S. Miwa, Phys. Lett. A **383**, 1203 (2019).

[74] T. Oguchi and T. Shishidou, Phys. Rev. B **70**, 024412 (2004).

[75] G. V. D. Laan, J. Phys. Condens. Matter **10**, 3239 (1998).

[76] P. Bruno and J. Renard, Appl. Phys. A **506**, 499 (1989).

[77] P. Bruno, Phys. Rev. B **39**, 865 (1989).

[78] S. Miwa, M. Suzuki, M. Tsujikawa, K. Matsuda, T. Nozaki, K. Tanaka, T. Tsukahara, K. Nawaoka, M. Goto, Y. Kotani, T. Ohkubo, F. Bonell, E. Tamura, K. Hono, T. Nakamura, M. Shirai, S. Yuasa, and Y. Suzuki, Nat. Commun. **8**, 15848 (2017).

[79] T. Seki, J. Shimada, S. Iihama, and M. Tsujikawa, J. Phys. Soc. Jpn. **86**, 074710 (2017).

[80] T. Kawabe, K. Yoshikawa, M. Tsujikawa, T. Tsukahara, K. Nawaoka, Y. Kotani, K. Toyoki, M. Goto, M. Suzuki, T. Nakamura, M. Shirai, Y. Suzuki, and S. Miwa, Phys. Rev. B **96**, 220412(R) (2017).

[81] M. H. Kryder and C. S. Kim, IEEE Trans. Magn. **45**, 3406 (2009).

[82] S. S. P. Parkin, M. Hayashi, and L. Thomas, Science (80-.). **320**, 190 (2008).

[83] S. Parkin and S.-H. Yang, Nat. Nanotechnol. **10**, 195 (2015).

[84] M. Julliere, Phys. Lett. A **54**, 225 (1975).

[85] J. S. Moodera, L. R. Kinder, T. M. Wong, and R. Meservey, Phys. Rev. Lett. **74**, 3273 (1995).

[86] T. Miyazaki and N. Tezuka, J. Magn. Magn. Mater. **139**, 94 (1995).

[87] S. Yuasa and D. D. Djayaprawira, J. Phys. D. Appl. Phys. **40**, R337 (2007).

[88] S. S. Parkin, C. Kaiser, A. Panchula, P. M. Rice, B. Hughes, M. Samant, and S. H. Yang, Nat. Mater. **3**, 862 (2004).

[89] S. Yuasa, T. Nagahama, A. Fukushima, Y. Suzuki, and K. Ando, Nat. Mater. **3**, 868 (2004).

[90] W. H. Butler, X.-G. Zhang, T. C. Schulthess, and J. M. MacLaren, Phys. Rev. B **63**, 054416 (2001).

[91] D. D. Djayaprawira, K. Tsunekawa, M. Nagai, H. Maehara, S. Yamagata, N. Watanabe, S. Yuasa, Y. Suzuki, and K. Ando, Appl. Phys. Lett. **86**, 092502 (2005).

[92] S. Ikeda, J. Hayakawa, Y. Ashizawa, Y. M. Lee, K. Miura, H. Hasegawa, M. Tsunoda, F. Matsukura, and H. Ohno, Appl. Phys. Lett. **93**, 082508 (2008).

[93] S. Ikeda, K. Miura, H. Yamamoto, K. Mizunuma, H. D. Gan, M. Endo, S. Kanai, J. Hayakawa, F. Matsukura, and H. Ohno, Nat. Mater. **9**, 721 (2010).

[94] K. Watanabe, B. Jinnai, S. Fukami, H. Sato, and H. Ohno, Nat. Commun. **9**, 663 (2017).

[95] S. Ota, M. Ono, H. Matsumoto, A. Ando, T. Sekitani, R. Kohno, S. Iguchi, T. Koyama, and D. Chiba, Appl. Phys. Express **12**, 053001 (2019).

[96] S. Ota, A. Ando, T. Sekitani, T. Koyama, and D. Chiba, Appl. Phys. Lett. **115**, 202401 (2019).

[97] S. Yuasa, Y. Suzuki, T. Katayama, and K. Ando, Appl. Phys. Lett. **87**, 242503 (2005).

[98] A. Yamaguchi, T. Ono, and S. Nasu, Phys. Rev. Lett. **92**, 077205 (2004).

[99] M. Hayashi, L. Thomas, R. Moriya, C. Rettner, and S. S. P. Parkin, Science **320**, 209 (2008).

[100] S. Bhatti, R. Sbiaa, A. Hirohata, H. Ohno, S. Fukami, and S. N. Piramanayagam, Mater. Today **20**, 530 (2017).

[101] S. Mühlbauer, B. Binz, F. Jonietz, C. Pfleiderer, A. Rosch, A. Neubauer, R. Georgii, and P. Böni, Science **323**, 915 (2009).

[102] X. Z. Yu, Y. Onose, N. Kanazawa, J. H. Park, J. H. Han, Y. Matsui, N. Nagaosa, and Y. Tokura, Nature **465**, 901 (2010).

[103] J. Slonczewski, J. Magn. Magn. Mater. **159**, L1 (1996).

[104] L. Berger, Phys. Rev. B **54**, 9353 (1996).

[105] K. Ando, S. Fujita, J. Ito, S. Yuasa, Y. Suzuki, Y. Nakatani, T. Miyazaki, and H. Yoda, J. Appl. Phys. **115**, 172607 (2014).

[106] I. M. Miron, K. Garello, G. Gaudin, P.-J. Zermatten, M. V. Costache, S. Auffret, S. Bandiera, B. Rodmacq, A. Schuhl, and P. Gambardella, Nature **476**, 189 (2011).

[107] L. Liu, C.-F. Pai, Y. Li, H. W. Tseng, D. C. Ralph, and R. A. Buhrman, Science **336**, 555 (2012).

[108] R. Landauer, IBM J. Res. Dev. **5**, 183 (1961).

[109] W.-G. Wang, M. Li, S. Hageman, and C. L. Chien, Nat. Mater. **11**, 64 (2012).

[110] S. Kanai, Y. Nakatani, M. Yamanouchi, S. Ikeda, H. Sato, F. Matsukura, and H. Ohno, Appl. Phys. Lett. **104**, 212406 (2014).

[111] Y. Shiota, T. Nozaki, F. Bonell, S. Murakami, T. Shinjo, and Y. Suzuki, Nat. Mater. **11**, 39 (2012).

[112] S. Kanai, M. Yamanouchi, S. Ikeda, Y. Nakatani, F. Matsukura, and H. Ohno, Appl. Phys. Lett. **101**, 122403 (2012).

[113] T. Nozaki, Y. Shiota, S. Miwa, S. Murakami, F. Bonell, S. Ishibashi, H. Kubota, K. Yakushiji, T. Saruya, A. Fukushima, S. Yuasa, T. Shinjo, and Y. Suzuki, Nat. Phys. **8**, 491 (2012).

[114] Y. Shiota, T. Nozaki, S. Tamaru, K. Yakushiji, H. Kubota, A. Fukushima, S. Yuasa, and Y. Suzuki, Appl. Phys. Lett. **111**, 022408 (2017).

[115] T. Yamamoto, T. Nozaki, and H. Imamura, J. Phys. D Appl. Phys. **52**, 164001 (2019).

[116] T. Yamamoto, T. Nozaki, H. Imamura, Y. Shiota, T. Ikeura, S. Tamaru, K. Yakushiji, H. Kubota, A. Fukushima, Y. Suzuki, and S. Yuasa, Phys. Rev. Appl. **10**, 014013 (2019).

[117] M. Endo, S. Kanai, S. Ikeda, F. Matsukura, and H. Ohno, Appl. Phys. Lett. **96**, 212503 (2010).

[118] T. Nozaki, Y. Shiota, M. Shiraishi, T. Shinjo, and Y. Suzuki, Appl. Phys. Lett. **96**, 022506 (2010).

[119] F. Bonell, S. Murakami, Y. Shiota, T. Nozaki, T. Shinjo, and Y. Suzuki, Appl. Phys. Lett. **98**, 232510 (2011).

[120] Y. Shiota, F. Bonell, S. Miwa, N. Mizuochi, T. Shinjo, and Y. Suzuki, Appl. Phys. Lett. **103**, 082410 (2013).

[121] K. Yamada, H. Kakizakai, K. Shimamura, M. Kawaguchi, S. Fukami, N. Ishiwata, D. Chiba, and T. Ono, Appl. Phys. Express **6**, 073004 (2013).

[122] T. Nozaki, K. Yakushiji, S. Tamaru, M. Sekine, R. Matsumoto, M. Konoto, H. Kubota, A. Fukushima, and S. Yuasa, Appl. Phys. Express **6**, 073005 (2013).

[123] Y. Hibino, T. Koyama, A. Obinata, K. Miwa, S. Ono, and D. Chiba, Appl. Phys. Express **8**, 113002 (2015).

[124] W. Skowroński, T. Nozaki, Y. Shiota, S. Tamaru, K. Yakushiji, H. Kubota, A. Fukushima, S. Yuasa, and Y. Suzuki, Appl. Phys. Express **8**, 053003 (2015).

[125] Y. Hibino, T. Koyama, A. Obinata, T. Hirai, S. Ota, K. Miwa, S. Ono, F. Matsukura, H. Ohno, and D. Chiba, Appl. Phys. Lett. **109**, 082403 (2016).

[126] T. Nozaki, A. Kozioł-Rachwał, W. Skowroński, V. Zayets, Y. Shiota, S. Tamaru, H. Kubota, A. Fukushima, S. Yuasa, and Y. Suzuki, Phys. Rev. Appl. **5**, 044006 (2016).

[127] S. Kikushima, T. Seki, K. Uchida, E. Saitoh, and K. Takanashi, AIP Adv. **7**, 085210 (2017).

[128] T. Nozaki, A. Kozio, M. Tsujikawa, Y. Shiota, X. Xu, T. Ohkubo, T. Tsukahara, S. Miwa, M. Suzuki, S. Tamaru, H. Kubota, A. Fukushima, K. Hono, M. Shirai, Y. Suzuki, and S. Yuasa, NPG Asia Mater. **9**, e451 (2017).

[129] Y. Hayashi, Y. Hibino, F. Matsukura, K. Miwa, S. Ono, T. Hirai, T. Koyama, H. Ohno, and D. Chiba, Appl. Phys. Express **11**, 013003 (2018).

[130] T. Nozaki, T. Yamamoto, S. Tamaru, H. Kubota, A. Fukushima, Y. Suzuki, and S. Yuasa, APL Mater. **6**, 026101 (2018).

[131] Y. Kato, H. Yoda, Y. Saito, S. Oikawa, K. Fujii, M. Yoshiki, K. Koi, H. Sugiyama, M. Ishikawa, T. Inokuchi, N. Shimomura, M. Shimizu, S. Shirotori, B. Altansargai, Y. Ohsawa, K. Ikegami, A. Tiwari, and A. Kurobe, Appl. Phys. Express **11**, 053007 (2018).

[132] K. Ochi, T. Hirai, S. Ota, T. Koyama, T. Sekitani, and D. Chiba, Jpn. J. Appl. Phys. **58**, 118003 (2019).

[133] Y. Iida, Q. Xiang, J. Okabayashi, and T. Scheike, J. Phys. D Appl. Phys. **53**, 124001 (2020).

[134] K. L. Wang, J. G. Alzate, and P. Khalili Amiri, J. Phys. D Appl. Phys. **46**, 074003 (2013).

[135] T. Suntola, Appl. Surf. Sci. **100/101**, 391 (1996).

[136] C. S. Fadley, Prog. Surf. Sci. **16**, 275 (1985).

[137] E. H. Hall, Proc. Phys. Soc. London **4**, 325 (1881).

[138] K. Hasegawa, Y. Hibino, M. Suzuki, T. Koyama, and D. Chiba, Phys. Rev. B **98**, 020405(R) (2018).

[139] W. Grange, M. Maret, J. P. Kappler, J. Vogel, and A. Fontaine, Phys. Rev. B **58**, 6298 (1998).

[140] M. Suzuki, H. Muraoka, Y. Inaba, H. Miyagawa, N. Kawamura, T. Shimatsu, H. Maruyama, N. Ishimatsu, Y. Isohama, and Y. Sonobe, Phys. Rev. B **72**, 054430 (2005).

[141] R. Megy, D. Weller, J. Stohr, R. Nakajima, A. Carl, M. G. Samant, C. Chappert, P. Beauvillain, P. Veillet, and G. A. Held, Phys. Rev. Lett. **75**, 3752 (1995).

[142] L. F. Mattheiss and R. E. Dietz, Phys. Rev. B **22**, 1663 (1980).

[143] A. H. MacDonald, J. M. Daams, S. H. Vosko, and D. D. Koelling, Phys. Rev. B **23**, 6377 (1981).

[144] F. J. A. den Broeder, H. C. Donkersloot, H. J. G. Draaisma, and W. J. M. de Jonge, J. Appl. Phys. **61**, 4317 (1987).

[145] R. Wu, C. Li, and a.J. Freeman, J. Magn. Magn. Mater. **99**, 71 (1991).

[146] L. Cheng, Z. Altounian, D. H. Ryan, J. O. Ström-Olsen, M. Sutton, and Z. Tun, Phys. Rev. B **69**, 144403 (2004).

[147] S. Shimizu, K. S. Takahashi, T. Hatano, M. Kawasaki, Y. Tokura, and Y. Iwasa, Phys. Rev. Lett. **111**, 216803 (2013).

[148] K. Nakamura, T. Nomura, A. Pradipto, K. Nawa, T. Akiyama, and T. Ito, J. Magn. Magn. Mater. **429**, 214 (2017).

[149] D. Hayakawa, A. Obinata, K. Miwa, S. Ono, T. Hirai, T. Koyama, and D. Chiba, AIP Adv. **6**, 115305 (2016).

[150] J. G. Alzate, P. Khalili Amiri, G. Yu, P. Upadhyaya, J. A. Katine, J. Langer, B. Ocker, I. N. Krivorotov, and K. L. Wang, Appl. Phys. Lett. **104**, 112410 (2014).

[151] P. V. Ong, N. Kioussis, D. Odkhuu, P. Khalili Amiri, K. L. Wang, and G. P. Carman, Phys. Rev. B **92**, 020407 (2015).

[152] P. V. Ong, N. Kioussis, P. K. Amiri, and K. L. Wang, Sci. Rep. **6**, 29815 (2016).

[153] K. Kita, D. W. Abraham, M. J. Gajek, and D. C. Worledge, J. Appl. Phys. **112**, 033919 (2012).

[154] Y. Yang, J. Yuan, L. Qi, Y. Wang, Y. Xu, X. Wang, Y. Feng, B. Xu, L. Shen, and Y. Wu, Phys. Rev. B **95**, 094417 (2017).

[155] S. E. Barnes, J. Ieda, and S. Maekawa, Sci. Rep. **4**, 4105 (2014).

[156] Y. A. Bychkov and E. I. Rashba, JETP Lett. **39**, 78 (1984).

[157] H. B. Michaelson, J. Appl. Phys. **48**, 4729 (1977).

[158] M. T. Greiner, L. Chai, M. G. Helander, W.-M. Tang, and Z.-H. Lu, Adv. Funct. Mater. **22**, 4557 (2012).

[159] I. M. Miron, G. Gaudin, S. Auffret, B. Rodmacq, A. Schuhl, S. Pizzini, J. Vogel, and P. Gambardella, Nat. Mater. **9**, 230 (2010).

[160] U. Bauer, M. Przybylski, J. Kirschner, and G. S. D. Beach, Nano Lett. **12**, 1437 (2012).

[161] K. Leistner, N. Lange, J. Hänisch, S. Oswald, F. Scheiba, S. Fähler, H. Schlörb, and L. Schultz, Electrochim. Acta **81**, 330 (2012).

[162] K. Leistner, J. Wunderwald, N. Lange, S. Oswald, M. Richter, H. Zhang, L. Schultz, and S. Fähler, Phys. Rev. B **87**, 224411 (2013).

[163] L. Reichel, S. Oswald, S. Fahler, L. Schultz, and K. Leistner, J. Appl. Phys. **113**, 143904 (2013).

[164] F. Bonell, Y. T. Takahashi, D. D. Lam, S. Yoshida, Y. Shiota, S. Miwa, T. Nakamura, and Y. Suzuki, Appl. Phys. Lett. **102**, 152401 (2013).

[165] D. A. Gilbert, A. J. Grutter, E. Arenholz, K. Liu, B. J. Kirby, J. A. Borchers, and B. B. Maranville, Nat. Commun. **7**, 12264 (2016).

[166] U. Bauer, S. Emori, and G. S. D. Beach, Nat. Nanotechnol. **8**, 411 (2013).

[167] A. Rajanikanth, T. Hauet, F. Montaigne, S. Mangin, and S. Andrieu, Appl. Phys. Lett. **103**, 062402 (2013).

[168] C. Bi, C. Sun, M. Xu, T. Newhouse-Illige, P. M. Voyles, and W. Wang, Phys. Rev. Appl. **8**, 034003 (2017).

[169] A. J. Tan, M. Huang, C. O. Avci, F. Büttner, M. Mann, W. Hu, C. Mazzoli, S. Wilkins, H. L. Tuller, and G. S. D. Beach, Nat. Mater. **18**, 35 (2019).

[170] S. Gierałtowska, D. Sztenkiel, E. Guziewicz, M. Godlewski, and G. Łuka, Acta. Phys. Pol. A **119**, 692 (2011).

[171] T. Hirai, T. Koyama, and D. Chiba, Appl. Phys. Lett. **112**, 122408 (2018).

[172] Y. Hibino, T. Hirai, K. Hasegawa, T. Koyama, and D. Chiba, Appl. Phys. Lett. **111**, 132404 (2017).

[173] H. Nakayama, T. Hirai, J. Uzuhashi, R. Iguchi, T. Ohkubo, T. Koyama, D. Chiba, and K. Uchida, Appl. Phys. Express **12**, 123003 (2019).

[174] A. Manchon, C. Ducruet, L. Lombard, S. Auffret, B. Rodmacq, B. Dieny, S. Pizzini, J. Vogel, V. Uhlir, M. Hochstrasser, and G. Panaccione, J. Appl. Phys. **104**, 043914 (2008).

[175] A. Manchon, S. Pizzini, J. Vogel, V. Uhlir, L. Lombard, C. Ducruet, S. Auffret, B. Rodmacq, B. Dieny, M. Hochstrasser, and G. Panaccione, J. Appl. Phys. **103**, 07A912 (2008).

[176] B. Rodmacq, A. Manchon, C. Ducruet, S. Auffret, and B. Dieny, Phys. Rev. B **79**, 024423 (2009).

[177] J. Shiogai, T. Ohashi, T. Yang, M. Kohda, T. Seki, K. Takanashi, and J. Nitta, J. Phys. D. Appl. Phys. **49**, 03LT01 (2016).

[178] T. Koyama and D. Chiba, Phys. Rev. B **96**, 224409 (2017).

[179] D. Chiba, M. Kawaguchi, S. Fukami, N. Ishiwata, K. Shimamura, K. Kobayashi, and T. Ono, Nat. Commun. **3**, 888 (2012).

[180] C. Bi, M. Xu, H. Almasi, M. Rosales, and W. Wang, Adv. Funct. Mater. **26**, 3490 (2016).

[181] H. Yuan, H. Shimotani, J. Ye, S. Yoon, H. Aliah, A. Tsukazaki, M. Kawasaki, and Y. Iwasa, J. Am. Chem. Soc. **132**, 18402 (2010).

[182] V. Brites, K. Franzreb, J. N. Harvey, S. G. Sayres, M. W. Ross, D. E. Blumling, A. W. Castleman, and M. Hochlaf, Phys. Chem. Chem. Phys. **13**, 15233 (2011).

[183] C. Lourenço, M. D. C. Michelini, J. Marçalo, J. K. Gibson, and M. C. Oliveira, J. Phys. Chem. A **116**, 12399 (2012).

[184] W. H. Meiklejohn and C. Bean, Phys. Rev. **102**, 1413 (1956).

[185] W. H. Meiklejohn, J. Appl. Phys. **33**, 1328 (1962).

[186] A. E. Berkowitz and K. Takano, J. Magn. Magn. Mater. **200**, 552 (1999).

[187] J. Nogués and I. K. Schuller, J. Magn. Magn. Mater. **192**, 203 (1999).

[188] B. Dieny, V. S. Speriosu, S. S. Parkin, B. A. Gurney, D. R. Wilhoit, and D. Mauri, Phys. Rev. B **43**, 1297 (1991).

[189] M. Sato and K. Kobayashi, Jpn. J. Appl. Phys. **36**, L200 (1997).

[190] Y. Lu, R. A. Altman, A. Marley, S. A. Rishton, P. L. Trouilloud, G. Xiao, W. J. Gallagher, and S. S. Parkin, Appl. Phys. Lett. **70**, 2610 (1997).

[191] S. Fukami, C. Zhang, S. DuttaGupta, and H. Ohno, Nat. Mater. **15**, 535 (2015).

[192] S. Rezende and R. White, Phys. Rev. B **60**, 14837 (1999).

[193] A. P. Malozemoff, Phys. Rev. B **35**, 3679 (1987).

[194] D. Mauri, H. C. Siegmann, P. S. Bagus, and E. Kay, J. Appl. Phys. **62**, 3047 (1987).

[195] P. Borisov, A. Hochstrat, X. Chen, W. Kleemann, and C. Binek, Phys. Rev. Lett. **94**, 117203 (2005).

[196] V. Laukhin, V. Skumryev, X. Martí, D. Hrabovsky, F. Sánchez, M. V. García-Cuenca, C. Ferrater, M. Varela, U. Lüders, J. F. Bobo, and J. Fontcuberta, Phys. Rev. Lett. **97**, 227201 (2006).

[197] Y. H. Chu, L. W. Martin, M. B. Holcomb, M. Gajek, S. J. Han, Q. He, N. Balke, C. H. Yang, D. Lee, W. Hu, Q. Zhan, P. L. Yang, A. Fraile-Rodríguez, A. Scholl, S. X. Wang, and R. Ramesh, Nat. Mater. **7**, 478 (2008).

[198] X. He, Y. Wang, N. Wu, A. N. Caruso, E. Vescovo, K. D. Belashchenko, P. A. Dowben, and C. Binek, Nat. Mater. **9**, 579 (2010).

[199] V. Skumryev, V. Laukhin, I. Fina, X. Martí, F. Sánchez, M. Gospodinov, and J. Fontcuberta, Phys. Rev. Lett. **106**, 057206 (2011).

[200] K. Toyoki, Y. Shiratsuchi, A. Kobane, C. Mitsumata, Y. Kotani, N. Tetsuya, and R. Nakatani, Appl. Phys. Lett. **106**, 162404 (2015).

[201] Y. Tokura, J. Magn. Magn. Mater. **310**, 1145 (2007).

[202] D. A. Gilbert, J. Olamit, R. K. Dumas, B. J. Kirby, A. J. Grutter, B. B. Maranville, E. Arenholz, J. A. Borchers, and K. Liu, Nat. Commun. **7**, 11050 (2016).

[203] L. Wei, Z. Hu, G. Du, Y. Yuan, J. Wang, H. Tu, B. You, S. Zhou, J. Qu, H. Liu, R. Zheng, Y. Hu, and J. Du, Adv. Mater. **30**, 1801885 (2018).

[204] M. Bibes and A. Barthélémy, Nat. Mater. **7**, 425 (2008).

[205] P. J. van der Zaag, R. M. Wolf, A. R. Ball, C. Bordel, L. F. Feiner, and R. Jungblut, J. Magn. Magn. Mater. **148**, 346 (1995).

[206] S. Maat, K. Takano, S. S. P. Parkin, and E. Fullerton, Phys. Rev. Lett. **87**, 087202 (2001).

[207] C. Tsang and K. Lee, J. Appl. Phys. **53**, 2605 (1982).

[208] A. P. Malozemoff, Phys. Rev. B **37**, 7673 (1988).

[209] T. J. Moran, J. M. Gallego, and I. K. Schuller, J. Appl. Phys. **78**, 1887 (1995).

[210] K. Zhang, T. Zhao, and H. Fujiwara, J. Appl. Phys. **89**, 6910 (2001).

[211] S. Brems, D. Buntinx, K. Temst, C. Van Haesendonck, F. Radu, and H. Zabel, Phys. Rev. Lett. **95**, 157202 (2005).

[212] N. J. Gökemeijer, T. Ambrose, C. L. Chien, N. Wang, and K. K. Fung, J. Appl. Phys. **81**, 4999 (1997).

[213] T. Ambrose and C. L. Chien, J. Appl. Phys. **79**, 5920 (1996).

[214] M. Ali, C. H. Marrows, M. Al-Jawad, B. J. Hickey, A. Misra, U. Nowak, and K. D. Usadel, Phys. Rev. B **68**, 214420 (2003).

[215] R. Shimabukuro, K. Nakamura, T. Akiyama, and T. Ito, Physica E **42**, 1014 (2010).

[216] Q. Xiang, Z. Wen, H. Sukegawa, S. Kasai, T. Seki, T. Kubota, K. Takanashi, and S. Mitani, J. Phys. D Appl. Phys. **50**, 40LT04 (2017).

[217] M. D. Stiles and R. D. McMichael, Phys. Rev. B **60**, 12950 (1999).

[218] J. Kanamori, Prog. Theor. Phys. **17**, 177 (1957).

[219] T. C. Schulthess and W. H. Butler, Phys. Rev. Lett. **81**, 4516 (1998).

[220] Y. Ijiri, T. C. Schulthess, J. A. Borchers, P. J. Van Der Zaag, and R. W. Erwin, Phys. Rev. Lett. **99**, 147201 (2007).

[221] R. Yanes, J. Jackson, L. Udvardi, L. Szunyogh, and U. Nowak, Phys. Rev. Lett. **111**, 217202 (2013).

[222] M. Bode, M. Heide, K. Von Bergmann, P. Ferriani, S. Heinze, G. Bihlmayer, A. Kubetzka, O. Pietzsch, S. Blügel, and R. Wiesendanger, Nature **447**, 190 (2007).

[223] H. Yang, A. Thiaville, S. Rohart, A. Fert, and M. Chshiev, Phys. Rev. Lett. **115**, 267210 (2015).

[224] O. Boulle, J. Vogel, H. Yang, S. Pizzini, D. D. S. Chaves, A. Locatelli, A. Sala, L. D. Buda-prejbeanu, O. Klein, M. Belmeguenai, Y. Roussigné, A. Stashkevich, S. M.

Chérif, L. Aballe, M. Foerster, M. Chshiev, S. Auffret, I. M. Miron, and G. Gaudin, Nat. Nanotechnol. **11**, 449 (2016).

[225] H. Yang, O. Boulle, V. Cros, A. Fert, and M. Chshiev, Sci. Rep. **8**, 12356 (2018).

[226] S. Murakami, N. Nagaosa, and S.-C. Zhang, Science **301**, 1348 (2003).

[227] J. Smit, Physica XXIV **24**, 39 (1958).

[228] L. Berger, Phys. Rev. B **2**, 4559 (1970).

[229] K. Garello, I. M. Miron, C. O. Avci, F. Freimuth, Y. Mokrousov, S. Blügel, A. Stéphane, O. Boulle, G. Gaudin, and P. Gambardella, Nat. Nanotechnol. **8**, 587 (2013).

[230] X. Fan, J. Wu, Y. Chen, M. J. Jerry, H. Zhang, and J. Q. Xiao, Nat. Commun. **4**, 1799 (2013).

[231] P. M. Haney, H.-W. Lee, K.-J. Lee, and M. D. Stiles, Phys. Rev. B **87**, 174411 (2013).

[232] S. Emori, T. Nan, A. M. Belkessam, X. Wang, A. D. Matyushov, C. J. Babroski, Y. Gao, H. Lin, and N. X. Sun, Phys. Rev. B **93**, 180402 (2016).

[233] H. An, Y. Kageyama, Y. Kanno, N. Enishi, and K. Ando, Nat. Commun. **7**, 13069 (2016).

[234] K.-U. Demasius, T. Phung, W. Zhang, B. P. Hughes, S.-H. Yang, A. Kellock, W. Han, A. Pushp, and S. S. P. Parkin, Nat. Commun. **7**, 10644 (2016).

[235] S. Emori, U. Bauer, S. Woo, and G. S. D. Beach, Appl. Phys. Lett. **105**, 222401 (2014).

[236] H. An, T. Ohno, Y. Kanno, Y. Kageyama, Y. Monnai, H. Maki, J. Shi, and K. Ando, Sci. Adv. **4**, eaar2250 (2018).

[237] R. Mishra, F. Mahfouzi, D. Kumar, K. Cai, N. Kioussis, H. Yang, M. Chen, and X. Qiu, Nat. Commun. **10**, 248 (2019).

[238] A. Ghosh, K. Garello, C. O. Avci, M. Gabureac, and P. Gambardella, Phys. Rev. Appl. **7**, 014004 (2017).

[239] M. Hayashi, J. Kim, M. Yamanouchi, and H. Ohno, Phys. Rev. B **89**, 144425 (2014).

[240] C. O. Avci, K. Garello, M. Gabureac, A. Ghosh, A. Fuhrer, S. F. Alvarado, and P. Gambardella, Phys. Rev. B **90**, 224427 (2014).

Publication list

1. **T. Hirai**, T. Koyama, A. Obinata, Y. Hibino, K. Miwa, S. Ono, M. Kohda, and D. Chiba,
   "Control of magnetic anisotropy in Pt/Co system using ionic liquid gating"
   Applied Physics Express **9**, 063007 (2016).

2. T. Tamegai, **T. Hirai**, Y. Sun, and S. Pyon,
   "Trapping a Magnetic Field of 7.9 T using Bulk Magnet Fabricated from Stack of Coated Conductors",
   Physica C: Superconductivity and its Application **530**, 20 (2016).

3. Y. Hibino, T. Koyama, A. Obinata, **T. Hirai**, S. Ota, K. Miwa, S. Ono, F. Matsukura, H. Ohno, and D. Chiba,
   "Peculiar temperature dependence of electric-field effect on magnetic anisotropy in Co/Pd/MgO system",
   Applied Physics Letters **109**, 082403 (2016).

4. D. Hayakawa, A. Obinata, K. Miwa, S. Ono, **T. Hirai**, T. Koyama, and D. Chiba,
   "Dielectric and magnetic characterizations of capacitor structures with an ionic liquid/MgO barrier and a ferromagnetic Pt electrode",
   AIP Advances **6**, 115305 (2016).

5. Y. Hibino, **T. Hirai**, K. Hasegawa, T. Koyama, and D Chiba,
   "Enhancement of the spin-orbit torque in a Pt/Co system with a naturally oxidized Co layer",
   Applied Physics Letters **111**, 132404 (2017).

6. Y. Hayashi, Y. Hibino, F. Matsukura, K. Miwa, S. Ono, **T. Hirai**, T. Koyama, H. Ohno, and D. Chiba,
   "Electric-field effect on magnetic anisotropy in Pt/Co/Pd/MgO structures deposited on GaAs and Si substrate",
   Applied Physics Express **11**, 013003 (2017).

7. **T. Hirai**, T. Koyama, and D. Chiba,
   "Control of magnetism by electrical charge doping or redox reactions in a surface-oxidized Co thin film with a solid-state capacitor structure", Applied Physics Letters **112**, 122408 (2018).

8. Y. Tanaka, **T. Hirai**, T. Koyama, and D. Chiba,
   "Electric-field-induced magnetic domain writing in a Co wire",
   Applied Physics Express **11**, 053005 (2018). (Spotlight in 2018)

9. A. Obinata, **T. Hirai**, Y. Kotani, K. Toyoki, T. Nakamura, T. Koyama, and D. Chiba,
   "Electric field effect on magnetism in a MgO/Pd/Co system with a solid-state capacitor structure",
   AIP Advances **8**, 115122 (2018).

10. K. Ochi, **T. Hirai**, S. Ota, T. Koyama, T. Sekitani, and D. Chiba,
    "Solid-state capacitor for voltage control of magnetism formed on a flexible substrate",
    Japanese Journal of Applied Physics **58**, 118003 (2019).

11. H. Nakayama*, **T. Hirai***, J. Uzuhashi, R. Iguchi, T. Ohkubo, T. Koyama, D. Chiba, and K. Uchida,
    "Electric-field-induced on-off switching of anomalous Ettingshausen effect in ultrathin Co films",
    Applied Physics Express **12**, 123003 (2019). (* : Equal contribution)

12. **T. Hirai**, T. Koyama, and D. Chiba,
    "Electric field modulation of exchange bias at the Co/CoO_x interface",
    Physical Review B **101**, 014447 (2020).

Acknowledgements

First and foremost, I would like to express my deepest gratitude to my supervisor, Prof. Daichi Chiba for continuous encouragement and offering specific ideas on my five-year research in the university of Tokyo.

I would like to offer my special thanks to Dr. Tomohiro Koyama for many experimental supports and insightful comments which strongly helped me to improve this thesis.

I would like to appreciate Prof. Makoto Kohda, Dr. Motohiro Suzuki, Dr. Ken-ichi Uchida, Dr. Ryo Iguchi, Dr. Hiroyasu Nakayama, Dr. Tadakatsu Ohkubo, and Dr. Jun Uzuhashi for collaborative work. I am deeply grateful to Prof. Yoshihiro Iwasa, Prof. Katsuyuki Fukutani, Prof. Shinichiro Seki, and Prof. Shinji Miwa for many constructive comments and recommendations on this thesis. My work greatly benefited from Prof. Masashi Kawasaki, Dr. Yusuke Kozuka, Dr. Takahiro Fujita, Dr. Yuki Ohuchi, Prof. Atsushi Tsukazaki, Prof. Masaki Nakano, Prof. Masafumi Shirai, Dr. Masahito Tsujikawa, Dr. Shimpei Ono, Dr. Kazumoto Miwa, Prof. Kazuhiko Matsumoto, Prof. Koichi Inoue, Dr. Yasushi Kanai, and Dr. Takao Ono for variable comments, technical supports, and sharing apparatus.

I would thank the present and past members of Chiba laboratory: Dr. Aya Obinata, Dr. Yuki Hibino, Mr. Shinya Ota, Mr. Daichi Hayakawa, Mr. Ryo Asai, Mr. Shogo Iguchi, Mr. Yichen Guan, Mr. Yohei Hayashi, Mr. Ryuhei Kohno, Mr. Yuya Sasakawa, Mr. Koki Ochi, Mr. Kento Hasegawa, Mr. Yuki Tanaka, Mr. Hiroki Matsumoto, Mr. Masaki Ono, Mr. Toho Nagaoka, Mr. Taiga Torii, Mr. Ryota Nagira, Dr. Masaru Yamashita, and Ms. Akiko Imai. Let me also thank the members of Iwasa laboratory. In particular, I want to reappreciate Dr. Yuki Hibino, Mr. Shinya Ota, and Mr. Kento Hasegawa and thank Mr. Masaru Onga, Mr. Yuji Nakagawa, and Mr. Hideki Matsuoka for enriching my research life

through scientific discussions and daily communications. I really appreciate Ms. Marina Mori, Ms. Yoshie Tsukasaki, Ms. Naoko Bungo, Ms. Tomomi Kaneko, and Ms. Keiko Yashima, the sophisticated secretaries of Chiba and Iwasa laboratory for supporting a lot of official and financial works.

I am financially supported by Japan Society for the Promotion of Science Research Fellowship for Young Scientists (Grant No. JP18J10734).

Finally, I would like to thank my parents and grandparents for their understanding and support of my college life.